

©Copyright by Rohit Pande 2012

All rights reserved

**RADIO-FREQUENCY ELECTROMAGNETIC
CHARACTERIZATION OF BIOMATTER AND NANOPARTICLES
FOR BIOMEDICAL APPLICATIONS**

A Dissertation
Presented to
the Faculty of the Department of Electrical and Computer Engineering
University of Houston

In Partial Fulfillment
of the Requirements for the Degree
Doctor of Philosophy
in Electrical Engineering

by
Rohit Pande
August 2012

RADIO-FREQUENCY ELECTROMAGNETIC CHARACTERIZATION OF BIOMATTER AND NANOPARTICLES FOR BIOMEDICAL APPLICATIONS

Rohit Pande

Approved:

Co-Chair of the Committee
Jarek Wosik, Research Professor,
Electrical and Computer Engineering

Co-Chair of the Committee
Wanda Wosik, Associate Professor,
Electrical and Computer Engineering

Committee Members:

Paul Ruchhoeft, Associate Professor,
Electrical and Computer Engineering

Akhil Bidani, Professor,
Biomedical Engineering

John H. Miller, Jr., Professor,
Physics

Biana Godin, Assistant Member,
Department of Nanomedicine,
The Methodist Hospital Research Institute

Suresh K. Khator, Associate Dean,
Cullen College of Engineering

Badrinath Roysam, Professor and Chair,
Electrical and Computer Engineering

Acknowledgements

This dissertation work would not have been possible without the guidance and the help of many individuals who have directly or indirectly contributed and extended their valuable assistance. First and foremost, I extend my heartfelt gratitude to my advisors, Dr. Jarek Wosik and Dr. Wanda Wosik, for their supervision, encouragement and generous and dependable support during the progression of my research work. Dr. Jarek Wosik, not only shared his valuable perceptions in relevance to the studies, but also trained me in excellent experimental etiquettes, problem analysis and system design techniques. I am highly obliged to Dr. Biana Godin for her direction, guidance and for the significant use of her facilities at The Methodist Hospital Research Institute throughout my work and also for serving on my committee. I am grateful to Dr. Leiming Xie for his remarkable insights into biophysics and bioelectromagnetics without which arriving into firm conclusions would have been very difficult. He proved to be a reckoner in solving my theoretical and scientific problems during the research. I express my sincere appreciations to Dr. Paul Ruchhoeft, Dr. Akhil Bidani and Dr. John Miller for serving on my committee.

I am highly grateful to Mr. Christian Kuether and Mr. Krzysztof Nesteruk who aided me in mechanical and electronic realization of this work. Mr. Kuether's skills at machine shop and Mr. Nesteruk's help with electronics and design were really noteworthy. I also appreciate Dr. Paolo Decuzzi's efforts to involve me and let me participate in CPRIT (Cancer Prevention & Research Institute of Texas) meetings, which allowed me to perform perceptive investigations for rf induced cancer therapy. I genuinely appreciate Srimeenakshi Srinivasan's help with material characterization and sample preparation. I am also grateful to all my colleagues for their perceptive

discussions and opinions and for being enormously supportive through out my graduate program at University of Houston. I am also thankful to my friend Dr. Heidi Vitrac who proofread my dissertation and provided me with her insightful consultations through out my research work.

Last but not least, I would like to express my utmost indebtedness to my parents and my first teachers Surendra and Deepa, my sister Arti and my uncle Guman who have always been financially and morally supportive and without whom, I would not be where I am today.

**RADIO-FREQUENCY ELECTROMAGNETIC
CHARACTERIZATION OF BIOMATTER AND NANOPARTICLES
FOR BIOMEDICAL APPLICATIONS**

An Abstract
of a
Dissertation
Presented to
the Faculty of the Department of Electrical and Computer Engineering
University of Houston

In Partial Fulfillment
of the Requirements for the Degree
Doctor of Philosophy
in Electrical Engineering

by
Rohit Pande
August 2012

Abstract

The influence of radio-frequency (*rf*) electromagnetic fields on biological tissues plays a critical role in their diagnostic and therapeutic applications. These include hyperthermia and *rf* ablation modalities for cancer, in which cell temperatures are increased to 41-46°C and above 56°C respectively. However, optimizing tumor's obliteration efficiency and selectivity is a challenge and is accomplished by functionalized magnetic/nonmagnetic nanoparticles as *rf* absorption enhancers. Since there is no explicit elucidation of the nanoparticles' heating mechanism, this dissertation focuses on the characterization of their heating efficiency.

Rf losses due to the interaction of nanoparticles in aqueous media with both electric (E_{rf}) and magnetic (H_{rf}) fields were investigated using a low input power hyperthermia-setup designed with a high quality factor LCR resonator to generate E_{rf} and H_{rf} fields up to 100 kV/m and 50 kA/m, in 12-50 MHz frequency range. To find the specific absorption rates (SAR), measurements of temperature change versus time were done on the metallic, dielectric and superparamagnetic nanoparticles, as they constitute the multifunctional nanoconstructs. Magnetic SAR for SPIO was calculated as 4 kW/kg and electric SARs for gold, silica and SPIO were calculated as $\sim 10^3$, 2 and 27 kW/kg respectively. This demonstrates that at MHz frequencies SARs for nanoparticles were overestimated by previous studies, which ignored ohmic heating of the conductive dispersion medium. From the analysis of non-magnetic nanoparticles, the enhanced dipole fields on gold were found three times higher than silica. The *rf* loss was strongly ascribed to the interaction of dipole fields with the electrical double layer (EDL) at the particle-electrolyte interface, which was confirmed by synergistic heat enhancement through EDL modification using physiologically relevant proteins.

In order to understand the nature of EDL at a charged surface, investigations of nonlinear rf responses of bio-electrolytes placed within gold electrodes of a capacitor as a part of frequency-adjustable LCR parallel-resonant circuit were reported. Measurements were done using the intermodulation distortion technique. It was confirmed that the measured intrinsic nonlinear effect originates from the electrode-electrolyte interface and is ion-concentration dependent. The third-order coefficient of the power series of the nonlinear transfer-function was related to capacitive and conductive components of the EDL's impedance.

Table of contents

ACKNOWLEDGEMENTS	v
ABSTRACT	viii
TABLE OF CONTENTS	x
LIST OF FIGURES	xiv
LIST OF TABLES	xx
CHAPTER 1 INTRODUCTION	1
1.1 THESIS ORGANIZATION	5
CHAPTER 2 ELECTROMAGNETIC FIELDS' INTERACTION WITH BIO-MATTER	7
2.1 FUNDAMENTALS OF BIOELECTROMAGNETICS	7
2.2 ELECTROMAGNETIC FIELD INTERACTIONS WITH BIOLOGICAL SYSTEMS.....	12
2.2.1 Electric field induced effects	13
2.2.2 Magnetic field induced effects	15
2.3 THERMAL EFFECTS	16
2.4 DIELECTRIC SPECTROSCOPY: FREQUENCY DEPENDENCE OF PERMITTIVITY AND CONDUCTIVITY.....	21
2.5 RF ELECTROMAGNETIC FIELDS INDUCED NONLINEAR EFFECTS	24
CHAPTER 3 RF ENERGY BASED THERMAL THERAPEUTICS AND NANOMEDICINE	29
3.1 THERMAL THERAPY (HYPERTHERMIA AND ABLATION)	29
3.1.1 Mechanism of thermal injury	30
3.1.2 Role of unique physiology of the tumor in heat therapy	31
3.1.3 Need for a targeted thermal therapy	34
3.2 MAGNETIC RESONANCE IMAGING GUIDED HYPERTHERMIA	36
3.3 NANOMEDICINE.....	37

3.3.1 Targeting Cancer.....	38
3.4 NANOPARTICLE ENHANCED HYPERTHERMIA.....	39
3.4.1 Magnetic Nanoparticle Hyperthermia.....	40
3.4.2 Non-magnetic gold nanoparticle hyperthermia	44
3.4.3 Carbon Nanotube Hyperthermia	50
3.5 CONCEPT OF VOLUME FRACTION	51
3.6 SAR STUDIES ON NANOPARTICLES	51
3.7 CLINICAL TRIALS USING NANOPARTICLES	53
3.8 DESIGN OF MULTIFUNCTIONAL NANOBIOCONJUGATED VECTORS	54
3.8.1 Hyperthermia with other modalities	54
3.8.2 Design of nanostage vectors	55
CHAPTER 4 PROBLEM STATEMENT.....	58
CHAPTER 5 RF INTERMODULATION DISTORTION MEASUREMENT SETUP.....	60
5.1 INTRODUCTION.....	60
5.2 INTERMODULATION DISTORTION SETUP TO MEASURE BIOLOGICAL NONLINEARITY	66
5.3 MEASUREMENT PROCEDURE	69
CHAPTER 6 RESULTS ON BIO-ELECTROCHEMICAL NONLINEARITY	70
6.1 PRELIMINARY MEASUREMENTS WITH DI WATER	70
6.2 MEASUREMENTS WITH AQUEOUS SOLUTIONS OF NaCl	70
6.3 SUPPLEMENTAL MEASUREMENTS WITH VARYING VALENCY AND FREQUENCY	72
6.4 MEASUREMENT ON BUFFERS AND YEAST SAMPLES.....	74
6.5 EXPLANATION OF NON-LINEARITY DUE TO ELECTRODE-ELECTROLYTE INTERFACE	75
6.5.1 Double layer model for electrode-electrolyte interface.	75
6.5.2 Mathematical analysis of the electrode-electrolyte non-linearity	79
6.5.3 Electronic schematic capture analysis of the nonlinearity due to electrode - electrolyte interface.....	82

CHAPTER 7 RF ELECTROMAGNETIC FIELDS INDUCED HYPERTHERMIA SETUP	85
7.1 INTRODUCTION.....	85
7.2 BLOCK DIAGRAM OF HYPERTHERMIA SETUP	86
7.3 LCR RESONATOR.....	86
7.3.1 Design	88
7.3.2 Coupling and RF excitation	89
7.4 TEMPERATURE SENSING AND HEAT SINK	90
7.5 FIELDS IN THE RESONATOR AND POWER MEASUREMENTS	92
7.5.1 Theoretical electric and magnetic fields	92
7.5.2 Experimental techniques to measure fields.....	93
7.5.3 Experimental fields' dependence on measured input power	95
7.5.4 Heating of superparamagnetic iron oxide nanoparticles with varying input power placed in capacitor and solenoid	97
CHAPTER 8 RESULTS: HYPERTHERMIA.....	99
8.1 CAPACITIVELY-COUPLED FIELD HEATING	99
8.1.1 Electric field heating of gold nanoparticles with varying concentrations.....	99
8.1.2 Electric field heating of porous silicon shells loaded with gold nanoparticles.....	104
8.2 CAPACITIVELY AND INDUCTIVELY COUPLED FIELD HEATING	105
8.2.1 Magnetic field and electric field heating of deionized water.....	106
8.2.2 Effect of conductivity on magnetic field and electric field heating.....	106
8.3 PRESENCE OF CONSERVATIVE AND MAGNETICALLY INDUCED FIELDS IN THE SOLENOID OF THE RESONATOR	109
8.4 HEATING OF NANOPARTICLES PLACED IN CAPACITOR AND SOLENOID.....	112
8.4.1 Heating of gold nanoparticles and control solutions in fields coupled in the capacitor and solenoid.....	112

8.4.2 Heating of silica nanoparticles and control solutions in fields coupled in the capacitor and solenoid	120
8.4.3 Electric field heating of silica nanoparticles with different ambiances	124
8.4.4 Preliminary results of magnetic field and electric field heating of super paramagnetic iron oxide nanoparticles	129
8.5 RESULTS OF SHIELDING ON ENDOMAG IRON OXIDE PARTICLES	132
CHAPTER 9 CONCLUSIONS AND FUTURE WORK	137
REFERENCES	141

List of figures

Figure 2-1 The electromagnetic spectrum	8
Figure 2-2 Polarization on a cell placed between two parallel plates	13
Figure 2-3 (a) Random alignment of water molecules (b) Water molecules aligned to electric field.....	14
Figure 2-4 Capacitive and inductive applicators and thermographic views of agar phantom with metallic sphere in electric and magnetic field heating	18
Figure 2-5 Dispersion of bio-matter showing real and imaginary parts of complex permittivity as the function of frequency	22
Figure 2-6 Typical β dispersion of a biological cell	23
Figure 2-7 Permittivity and conductivity changes as a function of frequency based on the double shell model of a cell using Maxwell-Wagner's mixture equation.....	24
Figure 3-1 External <i>rf</i> hyperthermia using antenna array and wave-guide applicators	30
Figure 3-2 Types of cellular injuries at different regimes of temperature	31
Figure 3-3 Comparison of blood vasculature of a normal cell and a tumor cell.....	32
Figure 3-4 Survival rate curves for the Chinese hamster ovarian cells evaluating hyperthermia efficiency	33
Figure 3-5 Zones of hyperthermia induced cell death	34
Figure 3-6 Targeted ablation could not focus the micro-metastases outside the ablation zone	35
Figure 3-7 (a) MRI Image of a porcine meat with introduced resonant circuit implant (b) Frequency and field strength product and its limitations for such MRI assisted hyperthermia	37

Figure 3-8 Bioconjugated nanocapsules with anticancer drug molecules and iron oxide nanoparticles loaded inside and phosphonate coatings for cell targeting.....	39
Figure 3-9 Structure of organic materials functionalized magnetic iron oxide core nanoparticles	41
Figure 3-10 Capacitive <i>rf</i> field heating using the Kanzius machine at 13.56 MHz.....	45
Figure 3-11 Subdomain-Boundaries of the nanoparticle with direction of applied electric field shown	47
Figure 3-12 Electric field distribution around a nanoparticle and a slice plot in xy plane for (a) metallic gold nanoparticle (b) dielectric silica nanoparticle; Electric field magnitudes along x and y axis for (c) metallic and (d) dielectric particle.....	48
Figure 3-13 Electrical double layer around particle showing redistribution of the charges around nanoparticle due to the surface charge.....	49
Figure 3-14 Clinical magnetic field applicator for hyperthermia	53
Figure 3-15 (a) Preoperative MRI with tumor area identified (b) Iron oxide nanoparticles injected with isothermal lines showing the calculated intra-tumoral temperatures.	53
Figure 3-16 Fabrication of porous silica magnetic nanocapsules as a chemotherapeutic synergetic drug carrier	55
Figure 3-17 Cancer treatment philosophy using systemic injection of nanoconstructs loaded with MRI contrast agents and nanoparticles	57
Figure 3-18 Schematic representation of temperature-induced release from temperature sensitive liposome nanocapsules.....	57
Figure 5-1 (a) Total Harmonic Distortion (b) Non-ohmic resistor (c) Multisim simulation for a nonlinear circuit element	61

Figure 5-2 (a) Intermodulation Distortion (b) A complete intermodulation distortion spectrum (c) Multisim simulation for a nonlinear circuit element	63
Figure 5-3 Fundamental and IMD input power per tone	66
Figure 5-4 Two-tone intermodulation distortion measurement setup.....	66
Figure 5-5 LCR resonator showing adjustable ferrite core-based inductor	67
Figure 5-6 (a) Expanded view of the sample capacitor (b) Lateral and top view of the sample capacitor (c) Resonant frequency sweep <i>versus</i> distance between the ferrite cores for different sample capacitances	68
Figure 6-1 Output power for the fundamental and the third-order intermodulation product <i>versus</i> input power for DI Water	70
Figure 6-2 Output power for the fundamental and the third-order intermodulation product <i>versus</i> input power for 0.01 M NaCl, 0.1 M NaCl and 1M NaCl solutions	71
Figure 6-3 Output power for the fundamental and the third-order intermodulation product <i>versus</i> input power for aqueous solutions of 0.1 M NaCl, 0.1 M MgCl ₂ and 0.1M LaCl ₃	72
Figure 6-4 Output power for the fundamental and the third-order intermodulation product <i>versus</i> input power for aqueous solutions of 0.1 M NaCl at 35, 50 and 80 kHz	73
Figure 6-5 Output power for the fundamental and the third-order intermodulation product <i>versus</i> input power for 1 M NaCl, PBS and yeast cells suspended in PBS and DI Water	74
Figure 6-6 Schematic representation of the electrical double layer[106]	76
Figure 6-7 Output power for the fundamental and third order intermodulation product <i>versus</i> input power	80
Figure 6-8 Plot of Equation 6.16 (black curve) and experimental data (red dots).....	82

Figure 6-9 (a) Diode representation of non-linearity of the electrode-electrolyte interface (b) Intermodulation distortion peaks from the Multisim simulation of the diode circuit for 0.01M, 0.1 M and 1M NaCl solutions	83
Figure 6-10 Output power for the fundamental and the third-order intermodulation product <i>versus</i> input power for 0.01 M, 0.1M and 1M NaCl aqueous solutions simulated from circuit level analysis.....	84
Figure 7-1 Capacitive and Inductive Heating System	85
Figure 7-2 Schematic representation of hyperthermia setup	86
Figure 7-3 A series LCR resonator circuit.....	87
Figure 7-4 Response of a series LCR resonant circuit with its current response.....	87
Figure 7-5 LCR resonator made up of oxygen free copper metal to realize the capacitive plates and the inductive coils; the sample is placed in a quartz tube mounted in cavities drilled in sapphire	88
Figure 7-6 Coupling and Q and f_r measurements using a network analyzer and LabView Interface.....	90
Figure 7-7 Driving input power to the critically coupled resonator using frequency sweeper coupled with amplifier	90
Figure 7-8 Ga-As monocrystal based optical fiber temperature sensor.....	91
Figure 7-9 Simulated electric and magnetic fields <i>versus</i> input power	93
Figure 7-10 Circuit to measure electric field between the capacitor plates.....	93
Figure 7-11 Measurement of magnetic field using search coil.....	94
Figure 7-12 Input power fed to the resonator (output from amplifier) with respect to input power from the frequency synthesizer.....	95
Figure 7-13 Square root dependence of (a) electric field between the capacitor plates (b) magnetic field within the solenoid <i>versus</i> input power.....	97

Figure 8-1 (a) Temperature <i>versus</i> time curves for gold nanoparticle and the two and four fold dilutions (b) Normalized slopes <i>versus</i> dilution ratio	100
Figure 8-2 Calorimetric components of heat from nanoparticle suspension	101
Figure 8-3 Conceptual design of silicon gold nanoconstructs	104
Figure 8-4 Electric field heating of Au nanoparticles and Si hemispheres loaded with Au	105
Figure 8-5 Temperature <i>versus</i> time curves for DI water when placed in a solenoid and capacitor	106
Figure 8-6 Temperature <i>versus</i> time curves for 5nm gold particles and DI water as a control, when placed in the solenoid and the capacitor	107
Figure 8-7 (a) Effect of conductivity change on heating of DI Water by making 2.5mM NaCl solution (b) Heating slopes of NaCl in electric and magnetic fields <i>versus</i> the salt concentration	108
Figure 8-8 Slopes of $\Delta T/\Delta t$ from heating 1.25mM, 2.5mM and 5mM NaCl solutions in solenoid and capacitor	109
Figure 8-9 Electric fields in capacitor, solenoid and solenoid with shield	110
Figure 8-10 Fields E_z , E_ϕ , H_z for (a) empty quartz tube (b) quartz tube filled with physiological saline solution and (c) shielded solenoid with saline solution	111
Figure 8-11 (a) Gold nanoparticle stock solutions (b) Centrifugation and filtrate preparation	114
Figure 8-12 UV-Vis absorbance spectra for (a) 20 nm and (b) 100 nm gold nanoparticle's stock, supernatant and flow-through filtrate	114
Figure 8-13 SEM images of 20 nm and 100 nm gold nanoparticles' stock and filtrate	115

Figure 8-14 Slope of heating of stock and filtrate of gold nanoparticle suspensions <i>versus</i> particle size (a) when placed in the capacitor (b) when placed in the solenoid	117
Figure 8-15 (a) Process for obtaining filtrate as a control solution from the silica nanoparticle stock solution (b) UV- Vis on filtrate and silica stock solutions	121
Figure 8-16 SEM micrographs for stock and filtrate of 100 nm silica nanoparticles	121
Figure 8-17 Slopes of filtrate and stock solutions for 100 nm and 200 nm silica NPs	123
Figure 8-18 Composite silica particle used in the study entailing silica, silica-water charged interface, adsorbed albumin and water solution	125
Figure 8-19 Thermographic results of heating of 30 nm silica particles in 2% w/v BSA and in 10 % v/v FBS and their respective controls including DI Water	126
Figure 8-20 Slopes for temperature rises <i>versus</i> albumin concentrations for 30, 50 and 100 nm silica nanoparticles	128
Figure 8-21 Heating slopes of SPIO in electric and magnetic fields <i>versus</i> the concentration fraction.....	129
Figure 8-22 TEM Images of SPIO (a) 5nm Sigma (b) 5nm Endomag (c) Dextran matrix showing the SPIO nanoparticles embedded in it	131
Figure 8-23 Nanoparticle samples placed in solenoid, capacitor and solenoid with shield for (a) 5 nm Au nanoparticle as magnetic control (b) 10 nm Sigma SPIO nanoparticle (c) 30 nm Endomag SPIO.....	131
Figure 8-24 Temperature <i>versus</i> time plotted for SPIO (a) 28 mg/mL (b) 1 mg/mL SPIO measured in three <i>rf</i> fields configurations	133

List of tables

Table 2.1 Review of biological nonlinear dielectroscopy.....	28
Table 3.1 Thermal power dissipation values for gold nanoparticles reported by different groups.	44
Table 6.1 P_{3IMP} and a_3 for respective molar concentrations	79
Table 7.1 Calculation of electric field between the plates of the capacitor	96
Table 7.2 Calculation of magnetic field within the solenoid	96
Table 8.1 SAR and conductivity of DI water	103
Table 8.2 SAR and conductivity calculations of gold nanoparticle's stock suspension and relative dilutions	103
Table 8.3 Molar concentration of aqueous NaCl solutions and their dc conductivity	107
Table 8.4 Calibrated local electric field values in the particular configuration from the slopes of NaCl solution heating.....	118
Table 8.5 Slopes of filtrate and nanoparticle samples in the capacitor and solenoid	119
Table 8.6 Calculated effective conductivity and SAR calculation for Gold filtrate and nanoparticle suspensions	120
Table 8.7 Calculated effective conductivity and SAR calculation for silica filtrate and nanoparticle suspensions	124
Table 8.8 Hydrodynamic radius of bare and BSA adsorbed silica NPs	126
Table 8.9 Conductivities and SARs for dispersion mediums	127
Table 8.10 Conductivities and SARs for bare and modified silica nanoparticles.....	127
Table 8.11 Slope values of NaCl and calculated local fields values for the three configurations.....	134

Table 8.12 Slope values of SPIO for the three configurations	134
Table 8.13 Magnetic SAR of Endomag iron oxide nanoparticles	136

Chapter 1 Introduction

Rapid technological advances in radio-frequency (*rf*) technology and engineering techniques have facilitated the development of promising new therapeutic and diagnostic techniques. *Rf* electrical impedance spectroscopy of tissues, cells, and sub-cellular organelles has lead to the identification of many diseases, distinguishing healthy cells from malignant and diseased ones [1]. *Rf* electromagnetic waves interact with biological cells and tissues through a number of mechanisms. Biological materials are inherently inhomogeneous lossy dielectric materials. They have remarkable dielectric properties, but are also considered electrolytic conductors [2, 3]. This makes them very interesting for physicists and electrical engineers to study. The cell, which is the basic organizational unit of every living biological system, consists of a conductive cytoplasm encapsulated by an insulating membrane separating the conductive extracellular environment. At lower frequencies, cell membranes, being capacitive in nature, exhibit huge impedance and prevent the electromagnetic (EM) waves from entering into the cell through the membrane. However, at higher frequencies, the waves can penetrate the membrane, thereby probing information regarding the molecules and sub-cellular organelles in the cytoplasm [4].

Moving higher and lower in the frequency regime also results in interesting thermal and non-thermal effects, probing and stimulating different cellular mechanisms [5]. Studying the nonlinear harmonic signatures from the output response of the impedance spectroscopy on various cell suspensions has helped in the identification of their different biochemical states. The nature of these harmonics could be related to the cellular phenomenon of aerobic and anaerobic respiration, fermentation, growth phases,

and their respiring capacity [6-9]. Therefore, by using a sensitive spectroscopy technique, differentiation between cellular states and metabolic activities can be achieved thereby proving useful for diagnostics at a cellular level.

Besides non-thermal effects, very strong and significant thermal effects are also observed due to the absorption of *rf* energy due to the electrically conductive nature of the biological tissue. Over the past few decades, these *rf* induced thermal effects have been studied so that they can be used to therapeutically treat diseases like cancer and joint and muscle diseases [10]. Using heat for physiotherapy and for other medical purposes is a well-established therapeutic approach in health sciences. One of these thermo-therapies is hyperthermia, where malignant tumors are heated up to therapeutic temperatures (43-45°C), without harming the surrounding healthy tissue [11, 12]. Healthy cells continue to divide until they get the apoptosis signal that leads to their programmed cell death. However, in cancerous cells there is an uncontrolled cell division leading to a disorganized and condensed vascular structure, which leads to difficulty in heat dissipation [13-15]. Intense heating leads to denaturation and coagulation of cell proteins governed by the heat-shock response of T-cells. Thus, external heat triggers irreversible necrosis in such cells leading to their death [16, 17].

Depending upon the target (particular area of cells/tissues or the whole body), hyperthermia could be classified as local hyperthermia or whole body hyperthermia. There is another technique called *rf*-ablation in which a thin probe is directly inserted into the tumor to release a high frequency current that locally produces heat, elevating temperatures above 56°C resulting in ablation of cells [18, 19]. Conventional external hyperthermia is marked by high-energy waves aimed at the tumor site near the body

surface using an *rf* applicator outside the body [20]. However such hyperthermia techniques have some drawbacks like insufficient temperature rise in tumor site, poor temperature distribution and often over-heating of tissue leading to organ damage.

With the innovative developments in the field of nanomedicine, the idea of using nanoparticles for enhancing the *rf* absorption and achieving a very efficient distribution of heat using external *rf* field applicators have been proposed [21]. Such nanoparticles enhanced hyperthermia modality is selectively destructive and demonstrates considerable merits over the conventional hyperthermia technique while not affecting the healthy tissues and the immune system [22, 23]. Nanomedicine has outlined many promising benefits for cancer theranostics and detection at early stages by incorporating the ability to transport complex molecular cargoes to the malignant sites as well as targeting specific cell populations. With dimensions of sub-cellular range, nanoscale devices are able to interact with biomolecules in the cell-surface and sub-cellular environment. Nanoparticles, tubes, shells, etc. can be bio-functionalized by coating them with antibodies, binding them to proteins, etc., resulting in a surface modification to perform targeted drug delivery and medical imaging [24, 25]. Bio-functionalized nanostage vectors have been designed to encapsulate drugs and nanoparticles and programmed to deliver them at specific tissue sites. They also demonstrate the capability to be internalized by human cancer cells serving customizable, targeted drug-delivery vehicles capable of loading chemotherapeutic drugs or therapeutic entities, nanoparticles, etc. into cancer cells while sparing healthy cells [26, 27].

Achieving hyperthermia using magnetic nanoparticles using *rf* EM waves have been already studied extensively in the past decade [28-33]. Successful clinical hyperthermia trials using the magnetic iron oxide nanoparticles have also been achieved [28, 34]. In recent years, heating on non-magnetic nanoparticles like gold nanoparticles and carbon nanotubes have also been presented to enhance hyperthermia with capacitively coupled *rf* fields and huge numbers for power loss per unit volume of gold have been reported stating the mechanism behind heating of the nonmagnetic nanoparticles is Ohmic [35-37]. Owing to reasonably large skin depth at *rf* frequencies, the methodology behind using nanoparticles as *rf* energy absorption enhancers, is very promising for treating extensive range of tumors, including deep-seated ones. The philosophy behind using nanostage vectors is to combine cancer modalities by rendering nanoparticle assisted hyperthermia as well as adjuvant chemotherapy from the drugs specifically being delivered to the targeted lesions. Nonetheless these reports are impressive and indicative of emerging cancer therapeutics; the underlying physical mechanism behind the heating of nanoparticles is ambiguous as a very limited literature is available on the heating mechanism of these particles. Significant disparities on the heating of nanoparticles have been reported stating Joule heating via ionic conduction of the electrolyte solution containing nanoparticles is the dominant mechanism, generating such rises in temperatures [38, 39].

Therefore, the concept of hyperthermia using such nano heat-enhancers is still being explored and *in vitro* and *in vivo* trials are being evaluated and understood. Studying EM properties and thermodynamics of the colloidal suspensions of the nanoparticles including the surface effects and the characterization of the appropriate

amount of heat to be delivered to the specific organ sites under the application of *rf*-fields is crucial for clinical applications and forms the basis of this dissertation. Improvement of temperature distributions in critical regions is also significant and requires further research.

1.1 THESIS ORGANIZATION

This dissertation contours the analysis of nonlinear and thermal effects of *rf* electromagnetic fields on bio-matter viz. bio electrolytes, buffers, nanoparticles, etc., and is divided into 7 chapters; Chapter 1 provides a general introduction to the dissertation, followed by Chapter 2 that gives a brief theoretical review on the *rf* field interactions with bio-electrolytes and bio-matters. The fundamentals of electromagnetics are also reviewed, keeping biological effects in consideration. Electrical and magnetic field induced effects on biological enzymes, membranes and cells are mentioned. Nonlinear impedance spectroscopy on cells is studied and the existing literatures relating the non-linearity to cell bioenergetics and electrode-electrolyte polarization are contemplated. The phenomenon of *rf* absorption and thus, specific absorption rate (SAR) for dosimetric analysis is explained. Chapter 3 covers *rf* induced thermal effects for providing hyperthermia for oncological treatments. Physiology of cancer cells with regards to susceptibility to heat is reviewed and the need of targeted therapy is ascertained. Some engineering concepts of nanotechnology reported to design nano-bio-conjugated vectors proposed as heat enhancers as well as drug capsules for *rf* induced hyperthermia techniques are contemplated. An assessment on SAR studies on magnetic and non-magnetic nanoparticles is also made in Chapter 3. In Chapter 4, the problem statement emphasizing the basis of the dissertation is

outlined. The requirement for adequate sensitivity of the nonlinear impedance spectroscopy technique and the intrinsic electrode-electrolyte polarization at *rf* frequencies is addressed. The need of development of an *rf* heating applicator is identified for assessing the thermal effects and for *in vitro* characterization of nanoparticles for hyperthermia optimization. Furthermore, issues of overestimation of SAR are also highlighted. Chapters 5 and 7 cover the design and development of experimental setups. In Chapter 5, a nonlinear bio-impedance sensor based on an *rf*-intermodulation distortion phenomenon has been explained. Chapter 6 covers the results and analysis of the nonlinear intermodulation spectroscopy with bio-electrolytes and cells and its analysis. Chapter 7 delineates the design and development of an *rf* heating applicator system for heating colloidal, cellular and nanoparticle suspensions. Chapter 8 comprises the results of hyperthermia on dielectric, metallic and magnetic nanoparticles with their calorimetric analysis. Chapter 9 concludes the study reiterating the significant findings and discusses its future implications.

Chapter 2 Electromagnetic fields' interaction with bio-matter

2.1 FUNDAMENTALS OF BIOELECTROMAGNETICS

Electromagnetic (EM) radiation is the propagation of energy by time varying electric and magnetic fields. Radiation is transmitted through space or a material medium as a disturbance without the transfer of matter. Electromagnetic radiations exhibit the properties of waves as well as particles and thus are considered to behave like discrete packets of energy and are characterized by three quantities, wavelength, frequency and energy, which are related as

$$Q = h\nu = hc/\lambda, \quad (2.1)$$

where h is Planck's constant. Frequency ν and wavelength λ are the wave parameters of the EM spectrum while the photon energy Q describes the particle behavior. Frequency is used to refer to the radio and microwave frequency regime, wavelength is used to depict the infrared, visible and ultraviolet radiations and finally photon energy is used to represent the X-ray and gamma ray. Since EM wave traverses through the space or a material medium, the properties of different material media is of great interest and are characterized by permittivity ϵ and permeability μ which are the measures of EM interaction of media with the electric and magnetic fields respectively. These quantities are related to each other as,

$$c = 1/\sqrt{\mu_0\epsilon_0}, \quad (2.2)$$

where c is the speed of light, μ_0 and ϵ_0 are the respective values in vacuum and are equal to $4\pi \times 10^{-7}$ H/m and 8.8541×10^{-12} F/m respectively.

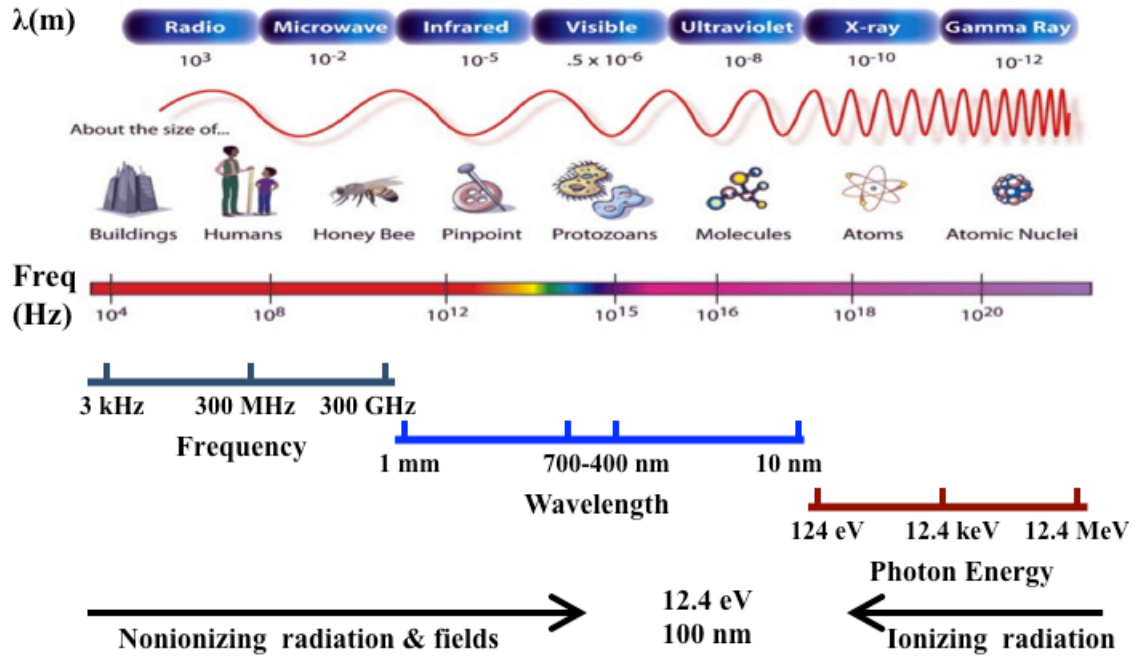


Figure 2-1 The electromagnetic spectrum

In the field of biomedicine, the EM spectrum is broadly divided into two regimes viz.: ionizing and non-ionizing radiation based on photon energy as shown in Figure 2-1 [40]. Photon energy of 12.4 eV is sufficient to ionize the hydrogen and oxygen atoms composing the water molecule. This energy resides roughly at about 100 nm wavelength in the ultra-violet regime and thus demarcates the boundary. The ionizing radiations are capable of disrupting molecular or atomic structures. Though ionizing radiation is used for imaging, its overuse is hazardous to health. The most significant issue is that at a higher frequency, penetration depth decreases which reduces the capability to probe the materials like human bodies, biological cells and tissues. Thus scientists prefer to use *rf* regimes to interrogate the biological samples.

This work focuses on *rf* regime of the EM spectrum, which covers a wide frequency range from 3 kHz to about 10 GHz. Hence, the terms *rf* and EM would be used to supplement each other throughout the dissertation. For EM waves, the electric field and the magnetic field are present simultaneously and are coupled together by Maxwell's equation. If there is a known electric field, then the corresponding magnetic field can be calculated. When a material is exposed to an applied electric field \mathbf{E} , it becomes polarized. The amount of polarization is termed as Polarization vector \mathbf{P} and defined as the electrical dipole moment per unit volume (C/m^2). The total electric field in a material is therefore the sum of the applied electric field and of an induced electric field due to the material polarization. Therefore another vector field \mathbf{D} (C/m^2) is used to define the sum as

$$\mathbf{D} = \epsilon_0 \mathbf{E} + \mathbf{P}. \quad (2.3)$$

When the material is isotropic, lossless and linear, equation (2.3) can be rewritten as

$$\mathbf{D} = \epsilon_0 \epsilon_r \mathbf{E} = \epsilon \mathbf{E}, \quad (2.4)$$

where ϵ (F/m) is the permittivity of the material and is the product of the vacuum permittivity, ϵ_0 (F/m) and the relative permittivity ϵ_r (dimensionless) of the material.

The electric susceptibility χ_e is related to relative permittivity as

$$\epsilon_r = 1 + \chi_e. \quad (2.5)$$

The relative permittivity is a complex quantity and can be written as

$$\epsilon_r = \epsilon'_r - j\epsilon''_r. \quad (2.6)$$

The real part ϵ'_r is called dielectric constant whereas the imaginary part ϵ''_r is a measure of the dielectric losses and their ratio is termed as the tangent of loss angle and is expressed as

$$\tan \delta_e = \frac{\epsilon''}{\epsilon'}. \quad (2.7)$$

Maxwell's equations suggest permittivity and conductivity to be related to one another.

The relationship between current density \mathbf{J} and the electric field \mathbf{E} can be written as

$$\mathbf{J} = (\sigma + j\omega\epsilon)\mathbf{E}, \quad (2.8)$$

or

$$\mathbf{J} = \sigma\mathbf{E} + j\omega(\epsilon' - j\epsilon'')\mathbf{E} = (\sigma + \omega\epsilon'')\mathbf{E} + j\omega\epsilon'\mathbf{E}. \quad (2.9)$$

From the above equation, the real part of the effective conductivity can be written as

$$\sigma'_{eff} = \sigma' + \omega\epsilon'', \quad (2.10)$$

while the imaginary part is

$$\sigma''_{eff} = \omega\epsilon'. \quad (2.11)$$

Equations 2.3-2.7 deal with polarization induced in a material media by its interaction with the electric field. Similarly, analogous equations exist for the magnetization induced in the material media due to its interaction with the magnetic field. Under an applied magnetic field \mathbf{H} , the material becomes magnetized. The amount of magnetization is termed as magnetization vector \mathbf{M} and defined as the magnetic dipole moment per unit volume (A/m^2). The total magnetic field in a material is the sum of the applied magnetic field and the induced magnetic field due to the intrinsic magnetization. Hence, vector field \mathbf{B} (Wb/m^2) referred to as magnetic flux density is used to define the sum as

$$\mathbf{B} = \mu_0(\mathbf{H} + \mathbf{M}). \quad (2.12)$$

When the material is isotropic, lossless and linear, then equation (2.12) can be rewritten as

$$B = \mu_0 \mu_r H = \mu H, \quad (2.13)$$

where μ (H/m) is the permeability of the material and is the product of the vacuum permeability μ_0 (H/m) and the relative permeability μ_r (dimensionless) of the material.

Again, the magnetic susceptibility χ_m is related to relative permeability as

$$\mu_r = 1 + \chi_m. \quad (2.14)$$

This relative permeability is a complex quantity and can also be written as

$$\mu_r = \mu'_r - j\mu''_r. \quad (2.15)$$

The imaginary part μ''_r is a measure of the magnetic losses and the ratio of the imaginary to the real part of complex permeability is termed as the tangent of loss angle and is expressed as

$$\tan \delta_m = \frac{\mu''_r}{\mu'_r}. \quad (2.16)$$

Bio-matter, including tissues and cells, can be studied in a dry form, but their electrical properties would be completely different from intact biological media. Under *in vivo* conditions, the electrolytic conductance of intra- and extracellular fluids, flushing through the biological material makes it challenging to analyze because of hydration and dominance of dipolar polarization from water like bio-electrolytes. Thus, bio-matter has to be considered as a conductor as well as a dielectric. The conductivity and permittivity are complex and can be addressed by the capacitive and conductive components, respectively. Effective conductivity is used to characterize a lossy conductor while the effective imaginary part of permittivity is used for describing a lossy dielectric. The permeability of biological materials is equal to that of free space. This means that biological tissue is non-magnetic. These effective conductivity,

permittivity and permeability, which are related by Maxwell's equations forms the basis of the interaction of *rf* fields with the biological materials and the various effects of such fields will be discussed in the following sections.

2.2 ELECTROMAGNETIC FIELD INTERACTIONS WITH BIOLOGICAL SYSTEMS

Electric (E) and magnetic (H) fields interact with any material in two ways. Primarily, the fields exert forces on charged particles in the material medium, thereby changing the charge distribution that originally existed. Secondly, the altered charge patterns in the materials produce additional E and H fields. Broadly, materials can be classified as magnetic or non-magnetic. In magnetic materials, magnetic dipoles are strongly affected by magnetic field. Biological systems are usually non-magnetic. In such non-magnetic materials, electric field interaction mechanism plays a significant role only. In dielectric type of non-magnetic materials, the electric field polarizes the bound charges or changes the orientation of permanent dipoles; however in conductors, electric field causes drift of electronic and ionic conduction charges. Biological systems are considered to be lossy dielectrics with ϵ'' as the measure of the loss. Therefore, any physiological effect in the biological system upon exposure to electromagnetic fields would be considered as a combined result of penetration and propagation of EM fields into the living system, the primary interaction of the fields with the bio-matter and then the possible secondary effects due to the primary interaction. Though the mechanisms of EM interactions are numerous, yet they can vaguely be classified as non-thermal effects and thermal effects.

Non-thermal effects include all the effects related to the cell and its membranes, tissues, changes in protein conformation, etc., where there are no evident changes in

temperature or the temperature change is low enough to stimulate thermoregulation. Thermal effects are mainly associated with thermal dissipation due to the absorption of electromagnetic fields due to the electrical conductivity from charged ions within the biological materials. Another important mechanism of heat dissipation is due to the hindered rotation of molecules. The thermal effects are dealt with in Section 2.6.

2.2.1 Electric field induced effects

Electric field interacts with the biological systems in various fashions. Due to electric fields cells can move by dielectrophoresis, show structural rearrangement, mechanical fracture, membrane electroporation, electro-fusion, etc. The basics of some of these effects are described here in a macroscopic fashion [41, 42].

2.2.1a Polarization of bound charges

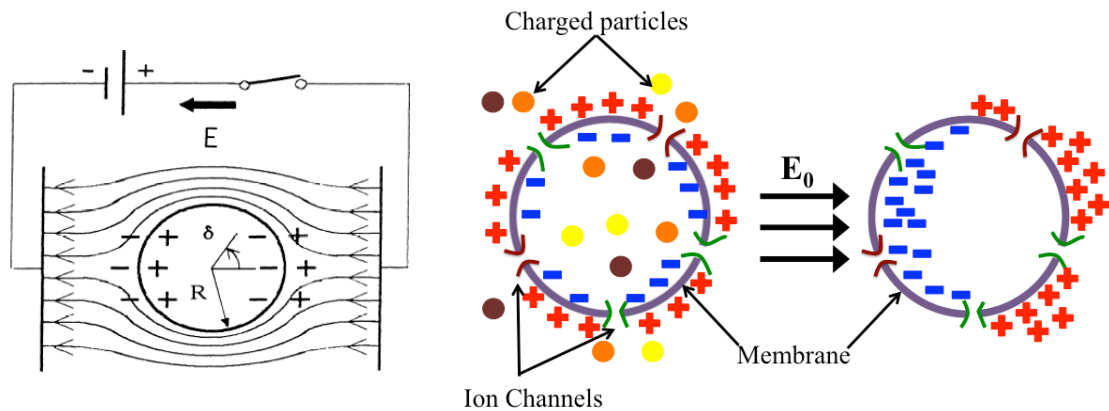


Figure 2-2 Polarization on a cell placed between two parallel plates

In the absence of electric field, opposite bound charges in an atom or molecule are superimposed and annuls each other's effect. Under the electric field, the electrostatic forces acting on the particle separates the charges, thereby forming a dipole with positive and negative charges separated by interatomic distances. This

phenomenon is termed as induced polarization and usually affects dielectric materials. Thus new fields are created which did not exist before.

2.2.1b Orientation induced in permanent electric dipoles

Permanent dipoles like water molecules are randomly oriented in the absence of electric field, but align when a field is applied. With the reversing polarity of the field, the molecules try to rotate back and forth. The total alignment of the permanent dipoles produces new fields. In response to these new fields, the conduction charges move considerable distances resulting in a drift from their resting position. Larger drift can be associated with larger conductivity.

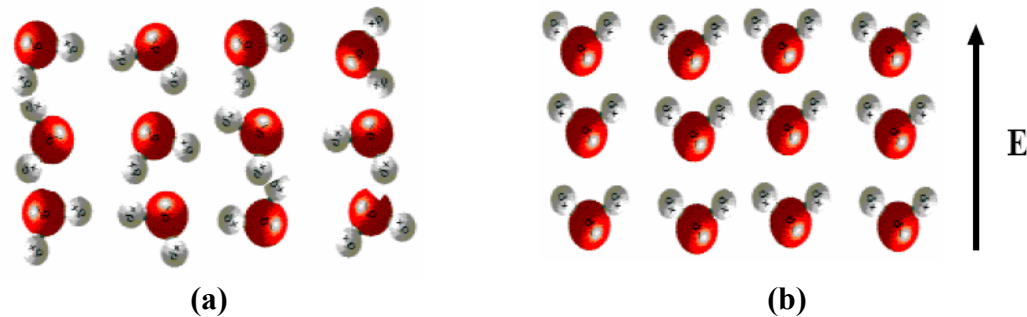


Figure 2-3 (a) Random alignment of water molecules (b) Water molecules aligned to electric field

2.2.1c Drift of conduction charges

Free and loosely bounded charges in the conductive biological material drift away when an external field is applied. Charges move and undergo elastic and inelastic collisions with other particles, thereby resulting in a small macroscopic average velocity in the direction of the applied field.

2.2.1d Pearl-chain effects and electro-rotation

Many biological particles like proteins suspended in an aqueous based media, align themselves to form pearl chains when an external electric field is applied. This alignment is independent of the frequency of the applied field and can occur only when the field strength is higher than a certain threshold [42]. Electro-rotation referred to as the rotation of cells is also observed when cells are placed in a circularly polarized electric field. The pearl chain effect and electro-rotation phenomena could be linked to the real and imaginary part of the induced dipole moment of the particles [43].

2.2.2 Magnetic field induced effects

As mentioned before, all the biological systems are non-magnetic and made up of cells and tissues. Cells are made up of insulating cell membranes, which separate conductive intra- and extracellular bio-electrolytes. Being non-magnetic, magnetic fields cannot directly interact with such fields, however they have a tendency to cause eddy currents at the cell membranes and tissue fluids, which flow in a close loop in a plane perpendicular to the direction of fluid. Based on Maxwell's equations, both currents and electric fields are produced inside the biological system. Such electric fields and currents can interact with the biological system in a secondary fashion [42]. Assuming the body to be homogenous and to have isotropic conductivity, the current density J in the perpendicular plane can be expressed as

$$J = \pi\sigma aBf, \quad (2.17)$$

where σ is the conductivity of the medium, a is the radius of the loop for current induction, B is the magnetic flux density and f is the frequency. However, this current cannot be accurately calculated due to the extreme heterogeneity of the body tissues.

Besides, biological effects like heating, rotation, etc., could be stimulated in the special microstructures like magnetosomes, hemoglobin, biological magnetites, etc., that are made up of paramagnetic and ferromagnetic compounds [44, 45].

2.3 THERMAL EFFECTS

Interaction of *rf* electromagnetic waves with biological tissues can result in thermal mechanisms marked by temperature variations due to energy transfer to tissue. These thermal effects are associated with the absorption of *rf* energy due to electrically conductive bio-matter. Intermolecular forces mutually hold the particles like atoms and molecules, which build up the biomatter. Alternating *rf* electric field produces a time varying current resulting in a rapid transfer of the energy of this current to the particles, which exhibits a resistance due to intermolecular forces, resulting in the heat loss. The power loss refers to the energy absorbed by the dielectric material from the peak electric field E_p and is measured per unit volume and is written as

$$P_{loss} = \frac{1}{2} \sigma |E_p|^2 = \frac{1}{2} \omega \epsilon_0 \epsilon'' |E_p|^2, \quad (2.18)$$

where ω is the angular frequency, ϵ is the permittivity and σ is the conductivity of the tissue. Such heating must be differentiated from the Joule-Lenz heating of the conductive material. When the conductivity is low and the frequency is high enough such that $\sigma \ll \omega \epsilon$, the dielectric heating is the dominant loss mechanism from the incident EM-wave into the matter.

Water is a polar molecule with a large permanent dipole moment, which is randomly oriented in the absence of an applied electric field E . The applied electric field orients the dipole moments to be along the direction of the field. This results in a

work done by the field to rotate the dipoles against the viscosity of the water molecule. Thus, the thermal dissipation arises from the hindered rotation of water molecules causing *rf* energy transfer into heat [5]. The heating mechanism associated with the alternating magnetic fields is different. In such a case, ohmic heating or Joule heating takes place, when eddy current flows through a resistive material. However with alternating electric field heating, the insulating dielectric layers of the tissues are well heated in contrast to inductive alternating magnetic field heating, that targets only on conductive matter.

Kotsuka reported a thermo-graphic experiment using rectangular and cylindrical agar phantoms under alternating *rf* electric field (3 MHz) and magnetic field (1.5 MHz) exposure [46]. The thermographs are shown in the Figure 2-4. This conveys that using magnetic field heating could heat the human body without producing high temperature zones in the insulating layers of subcutaneous adipose fat tissues and is advantageous over electric field heating. This thermal interaction of *rf* electromagnetic waves can be advantageous for several therapeutic purposes. However, since eddy currents generate at surfaces, it is difficult to target deeply seated lesions in the human body, which could lead to the over heating of undesired tissues and organs. Thermal ablation has been achieved by injecting the sodium chloride solution to evaluate the effect of conductivity on tissue. It was found that the sodium chloride concentration had significant but nonlinear effects on electrical conductivity, RF deposition and heating of agar phantoms. It is concluded that increasing conductivity using the saline solution can increase energy deposition, tissue heating and induced coagulation [10].

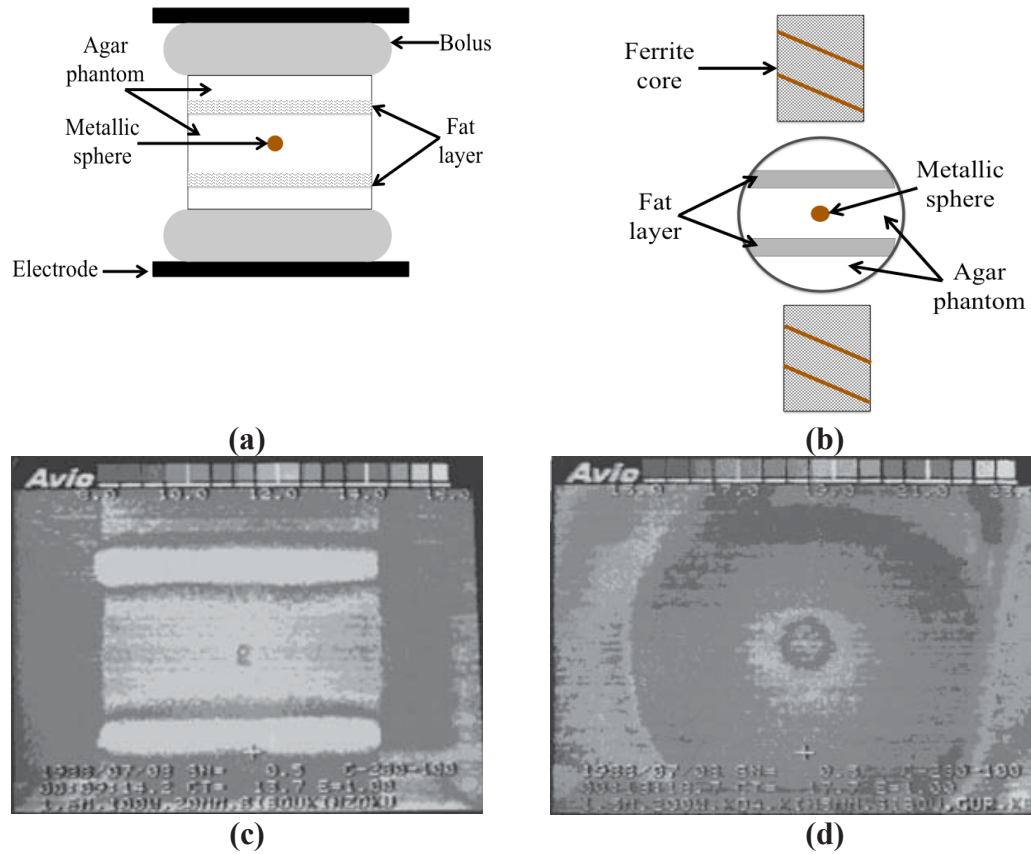


Figure 2-4 Capacitive and inductive applicators and thermographic views of agar phantom with metallic sphere in electric and magnetic field heating

The biological effects of electromagnetic fields do not only depend on the amplitude of the external power density, but also on the displacement (dielectric) field inside the body or tissue. A biological body is an inhomogeneous mass of a lossy dielectric material. Thus for meaningful quantization of any biological effect, the field inside the tissue has to be determined. For example, a rat and a human when exposed to the same external field will have entirely different internal field configurations. This is due to the fact that the internal fields depend on size, shape, and dielectric properties of the body and the organs.

Depending on the frequency of the electromagnetic waves and the complex conductivity of the matter, when passing from one medium to another, they can get

reflected, refracted, transmitted or absorbed. This absorbed energy is converted to other forms of energy usually heat. However, the waves may or may not penetrate the entire body. Penetration of electromagnetic waves is governed by a phenomenon called skin effect that is characterized by skin depth, which is a function of the electric and magnetic properties of the material and can be expressed as

$$\delta_s = \frac{1}{(\omega\mu\sigma/2)^{1/2}}, \quad (2.19)$$

where ω is the frequency of the EM wave, μ is the magnetic permeability of the bio-matter and σ is the electric conductivity of the material respectively.

The dosimetry of EM fields in the radiofrequency regime of the spectrum refers to quantification of amount of absorbed energy on an entity exposed to EM fields. Under the influence of steady state alternating fields, the time averaged rate of energy absorbed per unit volume (W/m^3) at a point inside an object is expressed as [41]

$$P = \sigma |E_{rms}|^2 = \omega\epsilon_0\epsilon'' |E_{rms}|^2. \quad (2.20)$$

To derive total rate of energy absorbed by an object, the value of P should be derived at each point inside the object and then integrated over the whole volume of the object.

For dosimetric quantification, the terms, “Specific Absorption Rate (SAR)” and “Specific Absorption (SA),” have been coined since the early 1970s. It was formalized in Report No. 67 of the National Council on Radiation Protection and Measurements (NCRP) in 1981 as follows, *“In view of the proliferation of terms for describing the electromagnetic radiation conditions in biologic materials and the discipline-oriented interpretation of these terms, it is recommended that the name ‘specific absorption rate’ be used for the quantity defined here, rather than such names as ‘absorbed power*

density per unit mass,''' [40]. “Specific” refers to the normalization to mass, “absorption” means the absorption of EM energy and “rate” means the time rate of change of EM energy absorbed. SAR at a point in the absorbing object is defined as the rate change of energy transferred to an infinitesimal volume at that point normalized by the mass of the infinitesimal volume. SA is the time integral of the SAR and is the energy dose. SAR is expressed as the ratio of absorbed power by absorbing mass and can be expressed as the time derivative of the incremental energy dW absorbed by or dissipated in an incremental mass dm confined in a volume element dV of a given density ρ . It can be written as

$$SAR = \frac{d}{dt} \left(\frac{dW}{dm} \right) = \frac{d}{dt} \left(\frac{dW}{\rho dV} \right). \quad (2.21)$$

Thus, SAR (W/kg) can be considered as an absorbed dose rate and using Poynting theorem could be related to electric fields at a given reference point as

$$SAR = \frac{P}{\rho_m} = \frac{\sigma |E|^2}{\rho_m} = \frac{\omega \epsilon_0 \epsilon'' |E|^2}{\rho_m}, \quad (2.22)$$

where σ is the conductivity of the material, ρ_m is the mass density of the material and E is the rms electric field strength. This SAR is a local SAR. To calculate, the whole-body or tissue average SAR, local SAR should be derived at each point inside the body/tissue and then integrated over the whole volume of the object as

$$SAR_{body} = \int_{body} \frac{\sigma(r) |E(r)|^2}{\rho(r)} dr. \quad (2.23)$$

For the thermal effects produced from the interaction of the rf fields with bio-matter, which will be reviewed in the coming sections, SAR can also be thermodynamically calculated as rate of temperature rise at a given point and can be

determined from measurements of the increment in temperature over a very short period of time following the exposure. In such cases, SAR is defined as

$$SAR = C \frac{\Delta T}{\Delta t}, \quad (2.24)$$

where C is the specific heat capacity of the matter. Thus, identifying level of SARs for *rf* exposure is very significant as SAR values give the quantitative idea about the *rf* induced thermal effects. It is estimated that taking thermoregulation into account, SAR of 0.001W/g produces an increase of 1°C in the human body and higher values of SAR could lead to malformations like retinal, corneal and ocular damages [47, 48].

2.4 DIELECTRIC SPECTROSCOPY: FREQUENCY DEPENDENCE OF PERMITTIVITY AND CONDUCTIVITY

Polarization is a disturbance of the charge distribution within a concerned region induced by an externally applied electric field. Relaxation of such a disturbance occurs in the time domain after a step increment or decrement in the electric field strength.[49, 50] This time-dependence of the polarization is reflected as the frequency dependence of the permittivity. As the frequency of exciting field is increased, high permittivity values measured at low frequencies start decreasing in confined steps. This dependence of the permittivity of biological cell suspensions on a broad frequency range of the applied electric fields results in four significant dielectric dispersions namely, α , β , δ and γ dispersions as shown in Figure 2-5 [7]. Each of these interaction mechanisms has its own kinetics, which determines the main feature of the dielectric spectrum of the tissue [41].

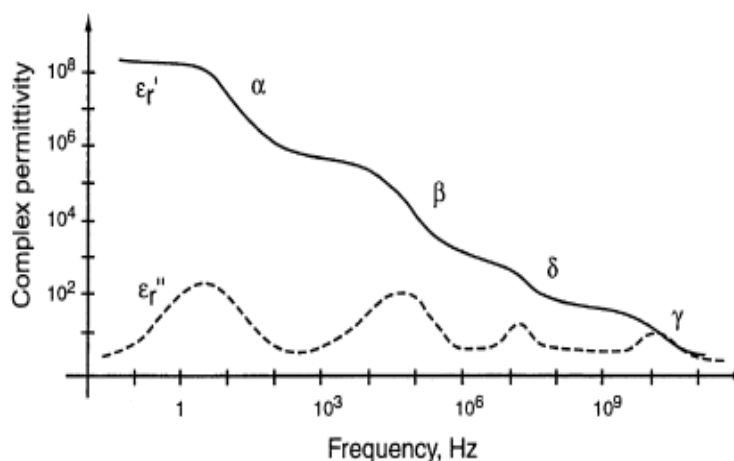


Figure 2-5 Dispersion of bio-matter showing real and imaginary parts of complex permittivity as the function of frequency

Each of the dispersion trends has its own characteristic frequency, which is the median value between those particular two transition levels formed by two consecutive dispersions. α -dispersion occurs in the region of 1 Hz to 10 kHz and is associated with the movement of ions around cell membranes. It is difficult to study because of the inherent counter-ion effects prevailing at such low frequencies. β -dispersion occurs at frequencies between 0.001 to 100 MHz and is due to interfacial polarization and is primarily due to the Maxwell-Wagner effects at the interface of insulating plasma membrane surrounding cells. δ -dispersion around 100 MHz to 1 GHz is due to the interaction with protein bound water molecules of hydration, rotation of amino acids and the partial rotation of the charged side groups of proteins. γ -dispersion occurs at 20 GHz resulting from the relaxation of the polar water molecules [6, 40]. Out of these, β -dispersion is the most significant of all the dielectric dispersions observed from the bio-matters.

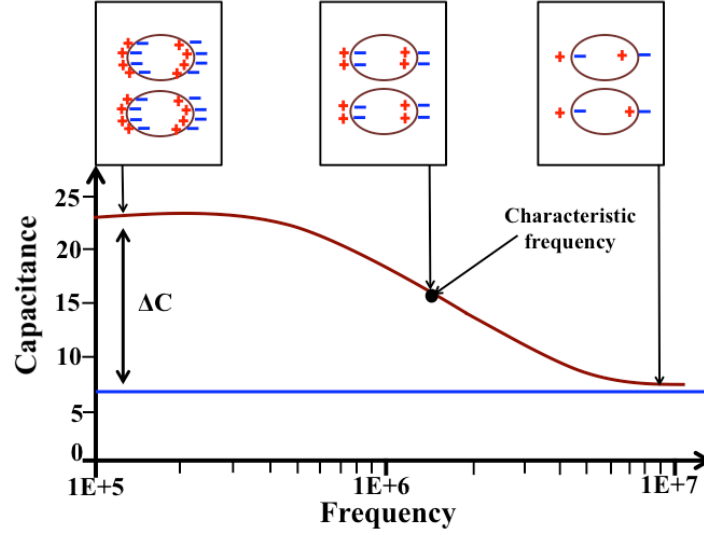


Figure 2-6 Typical β dispersion of a biological cell

β -dispersion accounts for the frequency range below which the externally applied electric field charges up the membrane as shown in Figure 2-6. The intra and extracellular ions takes considerable time to charge the cell membrane fully. With increase in frequency, lesser and lesser number of ions are able to charge the membrane. For β -dispersion, the characteristic frequency f_c at the median level of permittivity-fall is usually around 1 MHz. The characteristic frequency depends on size, shape, membrane capacitance and internal conductivity [6]. This frequency increases with conductivity of the internal and external media. Many reports have been already published where the characteristic frequency was used to calculate the large membrane capacitance [51-53]. β -dispersion goes away at the disruption of the membrane by use of detergents or ionophores. The complex dielectric constant of a cell suspension can be calculated based on Maxwell-Wagner's mixture equation [51, 52] as

$$\epsilon^* = \epsilon_a^* \frac{2\epsilon_a^* + \epsilon_p^* - 2\phi(\epsilon_a^* - \epsilon_p^*)}{2\epsilon_a^* + \epsilon_p^* + \phi(\epsilon_a^* - \epsilon_p^*)}. \quad (2.25)$$

Here ϕ is the volume fraction, ϵ_a^* is the complex permittivity of the medium in which the cells are dispersed, ϵ_p^* is the complex permittivity of the cell with membrane and ϵ^* is the complex permittivity of the whole system consisting of cells dispersed in the medium with volume fraction ϕ . Figure 2-7 shows the double-shelled model of a cell along with the dielectric response showing increase in conductivity and decrease in permittivity with increasing frequency.

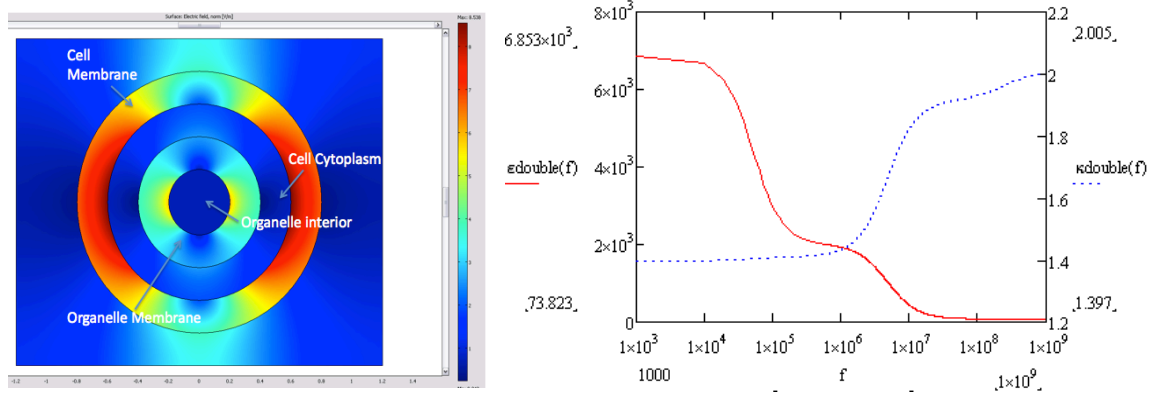


Figure 2-7 Permittivity and conductivity changes as a function of frequency based on the double shell model of a cell using Maxwell-Wagner's mixture equation

The simulations for dipolar electric fields on membrane of the cell and its organelle are done using quasi-static ac-dc modeling in COMSOL. The dispersion curves for permittivity *versus* frequency shows two distinct dispersions, one for the cell membrane and another for the organelle membrane.

2.5 RF ELECTROMAGNETIC FIELDS INDUCED NONLINEAR EFFECTS

Most of the investigated biological systems are quite complex mainly due to their colloidal nature. The dielectric response from the transfer function of complex systems like electrodes, cell-suspensions, etc., contains harmonic content. In such a case, sinusoidal excitation leads to a non-sinusoidal response. To better understand such

complex systems nonlinear response should be analyzed as it could render more information than the linear methods. Nonlinear effects in biological cells have been already reported where membrane embedded proteins, ion-channels, enzymes, and phenomena like electroporation and electro-fusion have been discussed as possible contributing factors [8, 54-56]. Theoretical analysis of conformational changes in membrane proteins in response to time-varying electric fields, resulting in nonlinear dielectric effects has been done [57]. Woodward and McShea have measured nonlinear response from suspensions of yeast cells and *Rhodobacter capsulatus*, when subjected to sinusoidal fields [58, 59]. With the use of specific inhibitors they concluded that H^+ /ATP-ase activity and the photosynthetic electron transport chain are responsible for nonlinear behavior, respectively.

As mentioned before, at kHz range of frequencies, the externally applied electric field charges up the cell membrane fully. Cell membranes are usually non-conducting at these frequencies. Thus, the low frequency exciting electric field polarizes the membrane, which also affects the polar and polarizable enzymes housed in the cell membranes [57]. An enzyme complex holds the Michaelis-Menten kinetics complying that the enzyme and the substrate, associate reversibly to form an enzyme-substrate complex. This association and dissociation stays at a rapid equilibrium. The externally applied sinusoidal field affects the enzyme by making it work chemically to carry an external substrate molecule across the membrane, thereby disturbing this equilibrium state [6]. Changes in these conformational states correlate with the dipole movements during molecular transport and are affected by the external stimulating fields resulting in nonlinear ac field induced shifts in the chemical equilibriums. All

chemical processes like the closing and opening of membrane channels, activation of membranous enzymes and ion adsorption-desorption processes with colloidal particles, when subjected to strong electric fields can produce harmonics.

Yeast's growth phases have also been determined by nonlinear dielectric properties of the measured current [9]. Passechnik modeled such a capacitive current to estimate the intramembranous field through lipid bilayer membranes [60]. The capacitive current density flowing through a membrane when a voltage $U = V + U_0 \sin \omega t$ is applied, is derived as

$$J = \frac{d}{dt} C_0 \left(1 + \frac{k C_0^2}{2 E \epsilon_0 \epsilon} (U + \Delta \phi)^2 \right) (U + \Delta \phi), \quad (2.26)$$

where C_0 is the specific capacitance of the membrane without any applied voltage, E and ϵ is the Young's Modulus and dielectric permittivity of the lipid bilayer membrane, $\Delta \Phi$ is the intra-membrane potential and k is a constant ranging from 1-2. Differentiating and expanding (2.26) to get higher-order terms, the following coefficients are derived:

$$A_1 = \omega U_0 C_0, \quad (2.27)$$

$$A_2 = \frac{3 \omega K C_0^3 U_0^2}{2 \epsilon_0 \epsilon E} (V + \Delta \phi), \quad (2.28)$$

$$A_3 = \frac{3 \omega K C_0^3 U_0^3}{8 \epsilon_0 \epsilon E}. \quad (2.29)$$

At a critical dc external voltage $V = V_c = -\Delta \Phi$, the even harmonic gets annulled, which gives the measure of membrane potential and thus the intra-membranous field. There has been extensive research conducted regarding nonlinear effects in biological samples.

Besides the non-linearity from bio-matter at low frequencies, non-linearity from rectification and the harmonics generation at the electrode-electrolyte interface (EEI) for electrochemical systems have been widely reported [61, 62]. The idea is to study the electrical properties including conductivities at those regimes where the linear Ohm's law is not obeyed. Schwan was among the first few to analyze the harmonic response of such an electrochemical system to a sinusoidal current or voltage excitation. He coined the limit law of linearity where higher current densities tend to onset the nonlinear electrode behavior. Rectifying properties of electrodes were investigated and the change in polarization capacitance and resistance were observed with increasing current density [63]. Richardot calculated theoretical expression for harmonics at lower frequencies based on nonlinear Faradaic charge transfer resistance with reference to Butler-Volmer kinetics [64]. Theoretical expressions to relate the polarization resistance measurement error to non-linearity has been shown [65]. Even, strongly nonlinear dynamics of electrolytes have been analyzed in the absence of the Faradaic current flow [66]. These nonlinear measurements are significant as they could test the linearization of bio-electrochemical systems and could attest the validity of impedance measurements. Such nonlinear measurements could be used as signatures for biochemical phenomena as well as induced charge electro-kinetic phenomena. Table 2.1 presents a review of certain biological effects accomplished from the investigation of harmonic response [15-22].

Table 2.1 Review of biological nonlinear dielectroscopy

Group	Methods	Inferences
Woodward & Kell	Suspensions of <i>Saccharomyces cerevisiae</i>	Resting cells-odd harmonics. Addition of inhibitor of ATP ase, metavanadate inhibits these odd harmonics. Glycolysing cells-even harmonics
Hironobu-Yositake	Suspensions of <i>Saccharomyces cerevisiae</i> with 4-electrode system	Resting cells-odd harmonics. Even numbered harmonics had a peak in logarithmic phase.
Hironobu-Yositake	Suspensions of <i>Saccharomyces cerevisiae</i> with 2-electrode system	Fundamental and odd harmonics decreases with time. Second harmonics of the suspension in the induction phase were larger than those in other growth phases.
Nawarathna <i>et al.</i>	Suspensions of <i>Saccharomyces cerevisiae</i> with 2-gold plated tungsten electrodes.	Odd harmonics for sufficiently high field amplitudes. Inhibitor suppresses the odd harmonics. Third harmonic was seen at lower field but was suppressed at higher field. Glucose results in even harmonics.
Nawarathna <i>et al.</i>	Suspensions of <i>Saccharomyces cerevisiae</i> with SQUID magnetometer	Odd harmonics are larger than even harmonics for resting cells.
Mercier <i>et al.</i>	Suspensions of <i>Saccharomyces cerevisiae</i> using tetrapolar electrode configuration.	Third harmonic in resting cells, showed significant temporal changes with yeast with actively respiring capacity and less significant change in the under-respiring capacity.
Kawanishi <i>et al.</i>	Suspensions of <i>Saccharomyces cerevisiae</i> with 2-gold electrodes in an acrylic cell	Anaerobic, aerobic respiration and fermentation were studied in terms of value of the power spectrum of third harmonic. During aerobic respiration no visible third harmonics were seen.

Chapter 3 RF energy based thermal therapeutics and nanomedicine

The rationale of thermal energy for therapeutic purposes has been used since thousands of years ago for treatment of joints, rheumatic diseases, boils, breast masses, etc. using moist or dry heat locally or by using hot irons for cauterization. In 1868, Busch found that fever induced by certain bacteria can cause tumor regression [67]. Since then and for the last several decades, a huge emphasis has been given to heat therapy for cancer treatment and novel modalities for the oncological therapeutics that are being engineered and investigated.

3.1 THERMAL THERAPY (HYPERTHERMIA AND ABLATION)

The National Institute of Health defines thermal therapy as a type of cancer treatment in which body tissue is exposed to high temperatures up to 42°C, to damage and kill cancer cells, or to make cancer cells more sensitive to radiation therapy or to anti-cancer drugs [67]. The thermal therapy for oncological treatment can be broadly categorized into two different modalities, viz.: hyperthermia and thermal ablation. Hyperthermia is the state of elevated temperature (41- 46°C) for a part of the body or the whole body. In whole body hyperthermia, the temperature is increased to higher levels using techniques such as warm water jackets, blankets, etc. In contrast, with local hyperthermia small areas such as tumor regions themselves are targeted. Based on the type of methodology, hyperthermia can also be termed as external hyperthermia, when it is marked by high-energy waves directed to the tumor site from an *rf* applicator outside the body. Figure 3.1 shows clinical hyperthermia treatment using eight radiating antennae built in the wall of the cylindrical applicator and four waveguide applicators with power adjustability, respectively [20].

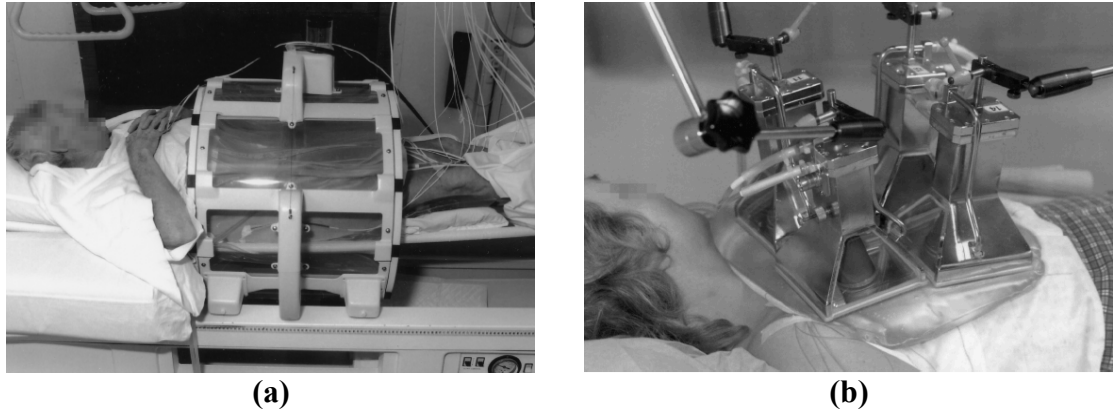



Figure 3-1 External *rf* hyperthermia using antenna array and wave-guide applicators

The internal hyperthermia or more specifically thermal ablation is associated with a thin probe inserted directly into the tumor. The thin probe directly releases a high frequency current that produces heat, elevating temperatures above 56°C resulting in ablation of cells within a localized section of a tumor.

3.1.1 Mechanism of thermal injury

The mechanism behind the cell death due to hyperthermia could be classified as necrosis and apoptosis. Necrosis is a quicker cell death which occurs when the cells are exposed to extreme variance from physiological conditions resulting in damage to plasma membrane potential, inability to maintain homeostasis, rupturing of cell-organelles and cell lysis. In contrast, apoptosis is programmed cell death induced by physiological stimuli like lack of growth factors, etc., and involves activation and enzymatic steps. Figure 3-2 shows the effect of temperature on biological tissues and entails the time requirements for sustained temperatures [42].



Temperature	Time	Physical effects	Biological effects
30-39°C	No time limit	No change	Cell-growth
40-46°C	30-60 min	Changes in the optical properties of tissue	Increased perfusion; thermo tolerance induction; hyperthermic killing
47-50°C	>10 min	Necrosis, coagulation	Protein denaturation; no soluble effects
<50 °C	After ~ 2 min	Necrosis, coagulation	Cell death
60-140°C	Seconds	Coagulation, ablation	Protein denaturation; membrane rupture; cell shrinkage
100-300°C	Seconds	Vaporization	Cell shrinkage and extracellular steam vacuole
<300°C	Fraction of a second	Carbonization , smoke generation	Carbonization

Figure 3-2 Types of cellular injuries at different regimes of temperature

Exposing tissues and cancer cells to temperature range of 41-47°C marks the beginning of apoptosis induction, micro-vascular damage, ischemia-reperfusion injuries, etc. This is referred to as the classical hyperthermia by exposing tissues to elevated temperatures for periods of 30-60 minutes. However, temperatures above 50°C result in irreversible cellular injury necrosis. The ideal case is to achieve selective necrosis and apoptosis at the tumor site without disturbing the healthy tissues.

3.1.2 Role of unique physiology of the tumor in heat therapy

The rationale of heat inducing physiological changes within the tissues is the basis for hyperthermia therapy. When heat is applied, the blood vasculature tries to cool down the tissue by increasing the blood flow and thus dissipates the heat. The lesser the blood flow, the more devastating would be the effect of heat on the tissue. However, the

structural and physiological vasculature of malignant tumors is different than normal tissues. The normal tissue has a typical artery-capillary-vein bed vasculature. The blood vessels are relatively uniform and are adequately adjacent enough to oxygenate well and provide sufficient nutrients to the tissue. However, when the tumor invades the normal cells, neovascularization occurs marked by the creation of new microvessels due to the increased proangiogenic factor expression from the tumor cells [68]. Thereafter, the existing normal blood vessels of the tissue also become physiologically abnormal by developing irregularities like arterio-venous shunts. Figure 3-3 depicts the tumor microcirculation where the tumor blood vessels are highly chaotic, irregular, and tortuous with blind ends and are devoid of smooth muscle enervation [69].

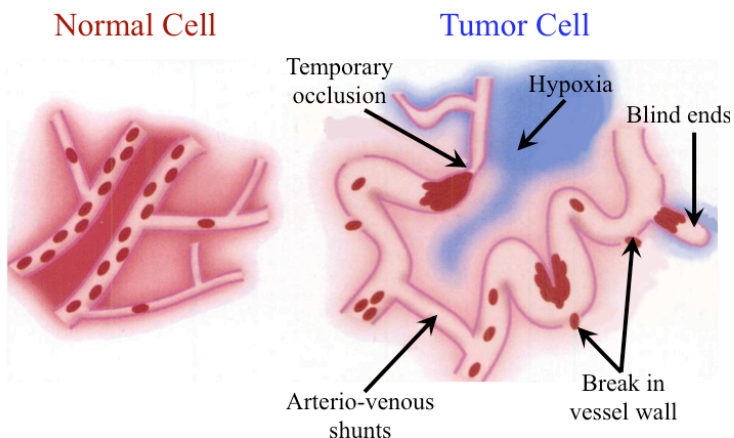


Figure 3-3 Comparison of blood vasculature of a normal cell and a tumor cell

Such blood vasculature leads to a sluggish and irregular blood flow and creates regions of hypoxia between the vessels and the tissue [69]. The tumor blood vessels have irregular and incomplete endothelial linings and membranes, which makes them “leakier” than the blood vessels of normal tissues [68]. This creates regions in tumors, which are deprived of oxygen and nutrients and thus are acidic, making them more sensitive to heat [70, 71]. When heat is applied, the cancer cell cannot get nutrients,

oxygen nor cooling, which enhances their susceptibility to heat in contrast to the normal cells with proper blood vasculature, which can survive heat.

The trends for cell survival rates with respect to exposure and temperature are shown in Figure 3-4 [72]. The cell survival rate is expressed as the ratio of the cell population that survived due to heating to the cell population before heating. With the increase in temperature and time of hyperthermia exposure, the cell survival rate decreases.

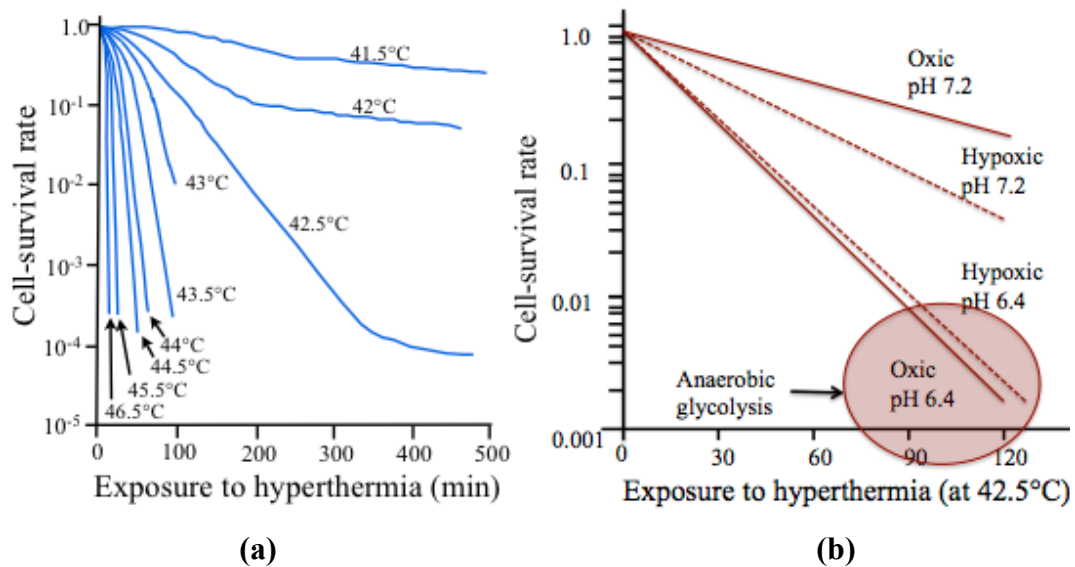


Figure 3-4 Survival rate curves for the Chinese hamster ovarian cells evaluating hyperthermia efficiency

Hyperthermia sensitivity of the cell is affected by the ambient oxygen partial pressure and the cellular pH conditions. With high pH conditions, the cell survival rate is large enough. Due to their uncontrolled growth and chaotic blood vasculature, cancerous cells have anaerobic conditions. With uncontrolled growth, malignant cells are drifted away from the blood vessels beyond the effective diffusion distance of oxygen in the respiring tissue, turning into hypoxic [69]. Thus they exhibit low oxygen partial pressure, which reduces the cell-survival rate. However, owing to the anaerobic

conditions, anaerobic glycolysis is triggered producing lactic acid, which reduces the pH and makes the conditions more acidic and further lowers the cell-survival rate. From the study, it is concluded that hyperthermia is very effective for cancer cells, where conditions of hypoxia and an acidic microenvironment prevail.

3.1.3 Need for a targeted thermal therapy

Currently available *rf* hyperthermia and ablation techniques, even if minimally invasive, are non-selective, and frequently induce thermal necrosis in both normal and malignant cells surrounding the *rf* ablation probes. The inductive heating and capacitive heating themselves are not efficient enough to target the cancer cells. Preferably, the ideal targeted heating should be achieved in a way that there are four zones of cell death (as shown in Figure 3-5) around the heat source, which occupies the lesion site. There should be an innermost strong necrotic zone, followed by a second mildly necrotic zone surrounding the first zone. The third apoptotic zone exists with lower heat levels but remains cytotoxic enough to cause apoptosis and the outermost zone is the zone with very least apoptosis.

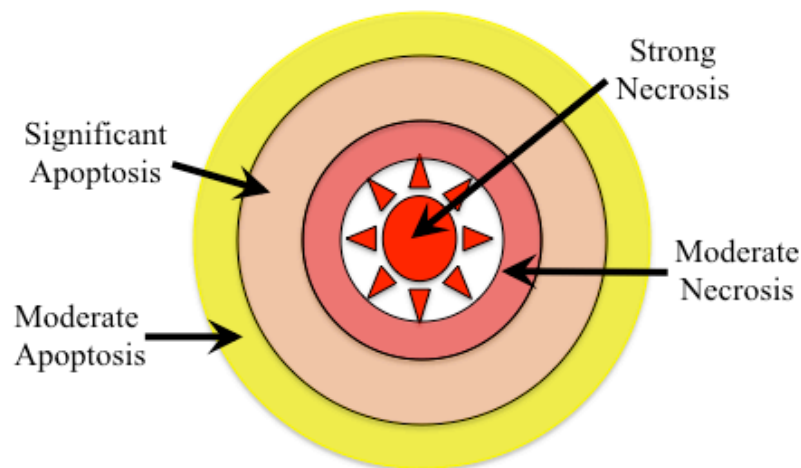


Figure 3-5 Zones of hyperthermia induced cell death

Such targeted modality would selectively kill the cancer cells in the inner zones, leaving healthy cells harmless. However, sometimes such hyperthermia cannot target the micro-metastases outside the thermo-ablation zone and the minimal heat of the moderate apoptosis region makes these cells thermoresistive as shown in Figure 3-6. This would result in relapse of the cancer [73].

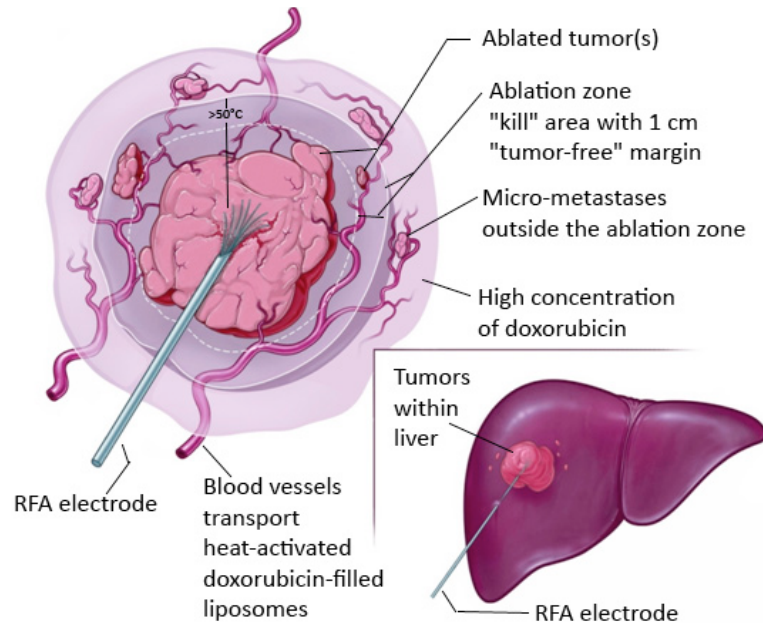


Figure 3-6 Targeted ablation could not focus the micro-metastases outside the ablation zone

The efficacy of hyperthermia treatment modalities by itself is not sufficient enough to substitute for chemotherapy and radiotherapy. However, applying the synergistic effects of hyperthermia as an adjuvant cancer treatment modality to chemotherapy and radiotherapy can significantly enhance oncological treatment. Combining hyperthermia with irradiation and cancer drugs turns out to be effective for clinical therapeutic sessions as the use of hyperthermia stimulates the blood flow to the

cancer site, which delivers higher concentration of cancer drug-molecules, thereby loading the anticancer drugs to such micro-metastatic sites [73].

3.2 MAGNETIC RESONANCE IMAGING GUIDED HYPERTHERMIA

With an objective to achieve targeted heating, the *rf* pulse of the Magnetic Resonance Imaging (MRI) system have been suggested to be used as a source to excite small resonant circuits, which are used as implants [74, 75]. These procedures allow a combination of hyperthermia from the external alternating fields of the MRI system and the MRI diagnosis concurrently. The implanted resonant circuit is a closed circuit connection of an inductor and a capacitor and its delivery to the tumor is achieved through a catheter. The frequency of the ac magnetic field is determined by the gyro-magnetic ratio of hydrogen (the detecting atom), which is 42.6MHz/T. Based on the MRI system (1.5 T, 3 T, etc.), the resonant frequency of the circuit should be matched. An MRI system excites an electromotive force, which induces an electric current that is maximum at resonance. The heat dissipation due to the current flow can be used to increase the temperature of target cancer cells by 10°C when implanted at lesion sites. Figure 3-7 shows an MRI image of porcine meat when exposed to such MRI assisted hyperthermia [74]. Nevertheless, the values for field strength and the frequency for hyperthermia have to be carefully manipulated, as the utmost priority is the human body's safety. Therefore, for clinical and biomedical reasons, an upper limit for frequency and field strength product has been established such that $H.f < 4.85 \times 10^8 \text{ Am}^{-1}\text{s}^{-1}$ [76]. This critical product was later on estimated to $5 \times 10^9 \text{ Am}^{-1}\text{s}^{-1}$ by Hergt based on weaker criteria.[31] Though, this technique seems to be promising with the ability to act locally at cancer sites, yet the technique is not very invasive and cannot

incorporate the specific delivery of chemotherapeutic drugs to be used in adjunct with hyperthermia at the lesions, hence possibilities from the field of nanomedicine are examined.

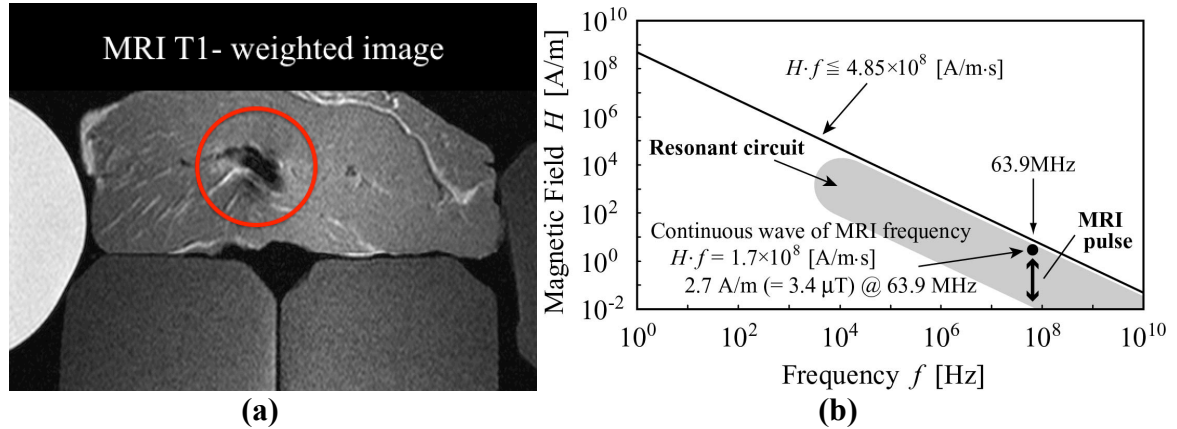


Figure 3-7 (a) MRI Image of a porcine meat with introduced resonant circuit implant (b) Frequency and field strength product and its limitations for such MRI assisted hyperthermia

3.3 NANOMEDICINE

Nanotechnology is the multidisciplinary realm of science, which encompasses ideas of physics, chemistry, engineering, biotechnology, etc., into engineering materials of very small sizes. The advancements in this realm have led to the development of the field of nanomedicine which allows the use of these nanoconstructs as biosensors, lesion targeted drug-delivery capsules and as excellent *in vivo* imaging agents. The diminutive size of nanoparticles allows them to penetrate cells and cell organelles and interact with cellular molecules. This makes them a good candidate for the treatment and diagnosis of various physiological abnormalities and disorders like Parkinson's and Alzheimer's diseases [77], tuberculosis and other lung diseases [78], etc. The concepts of nanomedicine when involved with hyperthermia suggest the possibility of targeted thermal therapy. The current research regarding the use of nanoparticles for cancer

targeting and diagnosis and their applications in the field of hyperthermia will be outlined in the subsequent sections and subsections.

3.3.1 Targeting Cancer

Nanoparticles can be modified in order to carry cancer specific drugs and deliver them to targeted sites. Targeting is very significant for cancer therapies as most of the cancer specific drugs have severe side effects because of unspecific action on benign cells. Selectivity is a function of the ability of nanoparticles to be internalized by cancer cells *in lieu* of healthy cells. Several cancer specific molecules (antibodies, specific ligands or peptides) can be conjugated to nanoparticles encapsulated within polymer capsules. Food and Drug Administration has approved many antibodies like Avastin, Herceptin, Bexxar, etc., to target colorectal, breast cancers, lymphoma, etc. [79]. This surface modification enhances the cancer cell specific binding affinity of the nanocapsules to surface receptor molecules on the tumor cell membrane surface. Thus with this passive targeting approach, these nanoparticles when systemically injected, get bound to these microscopic markers expressed on the cancer cell and by triggering receptor mediated endocytosis are drawn into the cancer cells without being macrophaged.

Depending on the surface morphology, the nanoparticles when injected systemically would be taken by the liver, spleen and other organs of the reticuloendothelial system [22]. The more hydrophobicity on the surface of the particles, the higher is the tendency to be taken by the liver, spleen and lungs. Thus, increasing the hydrophilic nature of the surface of the nanoparticles will reduce its clearance by microphages. Adsorption of proteins like Bovine Serum Albumin can

neutralize the charge on the surface of nanoparticles that facilitates their trajectory *en route* to the target lesion. The idea is to encapsulate MRI contrast agents and chemotherapeutic drugs, along with nanoparticles thereby permitting MRI diagnosis, chemotherapy and hyperthermia simultaneously. Figure 3-8 shows an example where multifunctional nanoparticles are designed for tumor specific drug delivery and to have imaging capability [80].

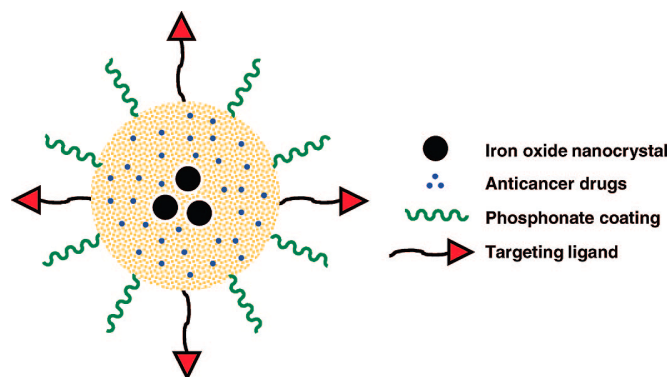


Figure 3-8 Bioconjugated nanocapsules with anticancer drug molecules and iron oxide nanoparticles loaded inside and phosphonate coatings for cell targeting

Superparamagnetic iron oxide nanocrystals are encapsulated in mesoporous silica nanoparticles. Phosphonates and folic acid targeting ligands are conjugated and cancer specific hydrophobic chemotherapeutic drug molecules are stored inside the pores. Modifying the surface morphology by attaching hydrophilic groups enhances the stability of nanoparticle dispersion in water-like media [80].

3.4 NANOPARTICLE ENHANCED HYPERTHERMIA

The innovations in the domain of nanomedicine have allowed the use of nanoscale materials for non-invasive targeted heating for rendering therapeutic cytotoxic temperatures. Molecularly labeled nanoparticles can be aimed to tumor cells and then heated using careful exposure to non-ionizing *rf* electromagnetic fields. This

heating is localized and minimizes the collateral damages to surrounding healthy tissue. Several different nanoparticles like iron oxide nanoparticles, gold nanoparticles and carbon nanotubes have been mentioned to epitomize the *rf* field induced heating [79]. This conversion of electromagnetic energy depends on a number of factors specific to the type of nanoparticles and their response to *rf* fields. However the explication of the mechanisms of nanoparticle's heating is very essential to enable understanding and design of thermo-therapeutic systems. With the change in the biochemical environment of different organs, tissues, cancer cells and cell organelles, the microenvironment of the nanoparticle also changes significantly. This certainly contributes to the disparities in the heating performances of the nanoparticles. Additionally, the contribution from the water-based dispersion medium for the nanoparticles cannot be ignored at the clinical frequencies in the MHz range. The loss from the electrically conductive dispersion medium accounts for the Joule heating *via* ionic conduction in the electrolytic medium. Thus *rf* field induced heat loss from a nanoparticle can be macroscopically classified into (1) primary heat loss from nanoparticle (based on the *rf* interaction heat dissipation mechanism), (2) secondary heat loss from the conductivity of the ionic dispersion medium and (3) heat loss from the polarization of the water molecule. The following sub-sections detail the different types of nanoparticles and their primary heating mechanisms based on their *rf* magnetic and electrical properties.

3.4.1 Magnetic Nanoparticle Hyperthermia

Over the past several years, heating due to alternating magnetic induction fields on colloidally dispersed magnetic and superparamagnetic particles in a liquid matrix have been reported. Heating related properties of magnetic nanoparticles were studied

for many years, which resulted in a significant progress in employing magnetic particles in research and also in clinical applications [34, 81, 82]. Studies on the thermo-therapeutic applications of magnetic materials to promote hyperthermia, commenced in 1957 by Gilchrist *et al.* where fine magnetic particles were injected in the lymph nodes which were subjected to induction heating to destroy the metastases [83]. Since then, several studies including few clinical trials have been performed [29-31, 81, 82, 84, 85]. More insights into physical limitations, cytotoxicity and the heating efficiency are currently obtained to evaluate the feasibility of the method for successful clinical trials. Owing to their size in nanometers, these particles have superparamagnetic behavior. The particles are assumed to be single domain particles with the absence of domain walls. Eddy current heating for such particles is assumed to be negligible. However in reality, these nanoparticles show a hysteresis loop with a negligible remanence and coercivity due to large sized particles or agglomeration in the bulk. Figure 3-9 shows the representative structure of different types of organic polymer functionalized magnetic nanoparticles [30].

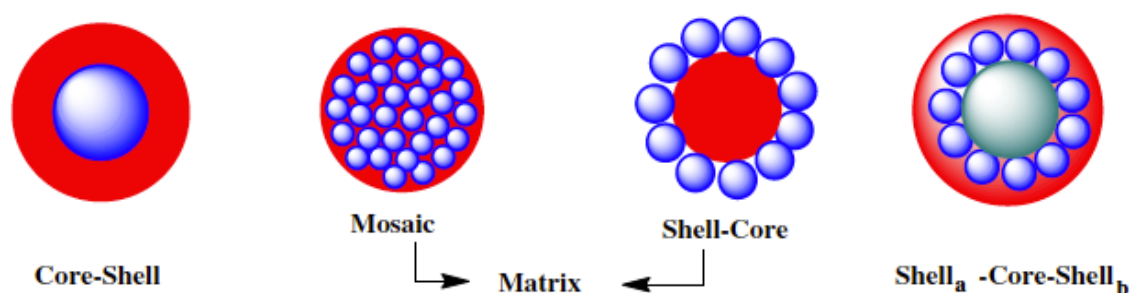


Figure 3-9 Structure of organic materials functionalized magnetic iron oxide core nanoparticles

3.4.1a Mechanism of magnetic heat loss

Rf magnetic fields, when applied to magnetic nanoparticles like iron oxide nanoparticles result in heat generation, which are accounted to the magnetic hysteresis losses or relaxation losses due to Brownian and Néel relaxation modes [86]. Being super-paramagnetic in nature, The *rf* heat dissipation for such single domain magnetic nanoparticles suspended in a colloidal form is caused by the delay in the relaxation of the magnetic moment through either the rotation within the particle (Néel) or the rotation of the particle itself to align with the field (Brownian) [29, 86]. *Rf* loss will also depend on nanoparticles' size and magnetic properties. In smaller nanoparticles the loss is dominated by Néel relaxation while in larger nanoparticles Brownian relaxation is the prevailing mechanism [84]. Thus heat dissipated is given by the average of both relaxations. Volumetric power dissipation in a magnetic field H_0 at a frequency f is given by

$$P = \pi \mu_0 \chi'' H_0^2 f, \quad (3.1)$$

where μ_0 is the relative permeability, χ'' is the out of phase component of the complex susceptibility χ and is defined as

$$\chi = \frac{\chi_0}{1 + j2\pi f\tau}. \quad (3.2)$$

Hence, the real and imaginary components of the complex susceptibility χ are

$$\chi' = \frac{\chi_0}{1 + j(2\pi f\tau)^2}, \quad (3.3)$$

and

$$\chi'' = \frac{2\pi f\tau}{1 + j(2\pi f\tau)^2} \chi_0. \quad (3.4)$$

Here χ_0 is the susceptibility estimated from the Langevin equation and is defined as

$$\chi_0 = \chi_i \frac{3}{\xi} \left(\coth \xi - \frac{1}{\xi} \right), \quad (3.5)$$

where $\xi = \mu_0 M_d H V_m / kT$ and $M_s = \phi M_d$ with M_d & M_s are the domain magnetization and the saturation magnetization of particle, V_m is the magnetic volume, and ϕ is the volume fraction of the magnetization. τ in Equations 3.2, 3.3 and 3.4 is referred to as time constant and is defined as

$$\frac{1}{\tau} = \frac{1}{\tau_N} + \frac{1}{\tau_B}, \quad (3.6)$$

where τ_N and τ_B are the Néel and Brownian relaxation time constants and are defined as

$$\tau_N = \frac{\sqrt{\pi}}{2} \tau_0 \frac{\exp\left(\frac{KV_M}{k_B T}\right)}{\sqrt{\frac{KV_M}{k_B T}}}, \quad (3.7)$$

and

$$\tau_B = \frac{3\eta V_H}{k_B T}. \quad (3.8)$$

Here, K is the anisotropy constant, k_B is the Boltzmann's constant, T is the absolute temperature, V_M and V_H are the magnetic and hydrodynamic volumes of the particle and can be written as $V_M = 4\pi R^3/3$ and $V_H = (1 + \delta/R)^3 V_M$, with R and δ , the thickness of an adsorbed surfactant layer and radius of the nanoparticle respectively. Thus, the power dissipation of magnetic nanoparticles can be expressed finally as

$$P = \pi \mu_0 \chi_0 H_0^2 f \frac{2\pi f \tau}{1 + (2\pi f \tau)}. \quad (3.9)$$

3.4.2 Non-magnetic gold nanoparticle hyperthermia

Gold nanoparticles undergo plasmonic absorptions mechanisms and show a typical characteristic extinction spectrum. By this process, the electrons of the gold resonate in response to incident radiation resulting in absorbing and scattering of light [87, 88]. This phenomenon can be exploited to use gold nanoparticles to achieve local tumor-ablative temperatures by conjugating them to biological cancer specific moieties. However, in past few years, several groups reported heating of gold nanoparticles under shortwave *rf* fields. Such non-resonant capacitively coupled fields tend to heat gold nanoparticles resistively to obtain a huge number of 300 kW/g for specific power loss for gold in all the cases [35-37, 89]. Some of these numbers are mentioned in the Table 3.1. The field applicator design for hyperthermia reported on the gold nanoparticles was done using a Kanzius *rf* capacitive heating machine or similar applicator design [36, 90]. As shown in Figure 3-10, the Kanzius machine is based on a capacitive field arrangement in which the gold samples are placed within the field generated at 13.56 MHz within two metal plate electrodes coated with an insulating Teflon layer [37].

Table 3.1 Thermal power dissipation values for gold nanoparticles reported by different groups.

Study	Gold conc.	Dissipative power of gold
Moran et al. 2009	1 ppm	380×10^6 W/kg
Curley et al. 2010	1 ppm	300×10^6 W/kg
Kruse et al. 2011	16 μ g/mL	$356 \pm 78 \times 10^6$ W/kg

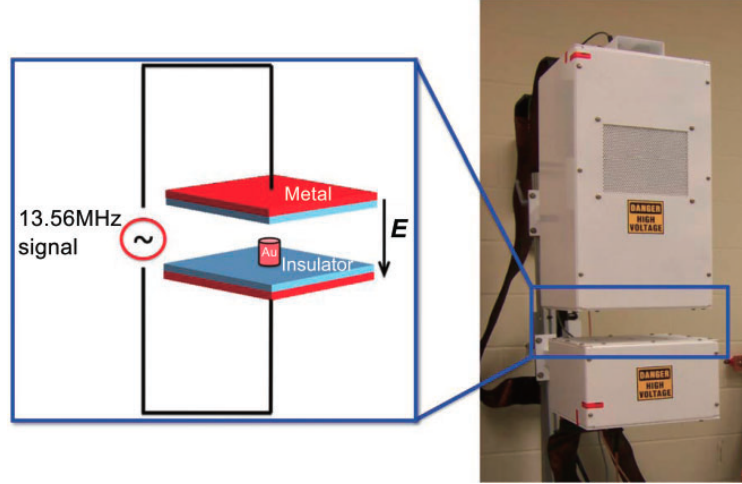


Figure 3-10 Capacitive *rf* field heating using the Kanzius machine at 13.56 MHz

In one study, human cell lines Hep3B cells and Panc-I cells were treated *in vitro* with 67 μ M/L gold nanoparticles and no intrinsic cytotoxicity or anti proliferative effect was observed. When exposed to *rf* fields, an average of 98% of cells were killed at *rf* exposure [35]. These *in vitro* experiments give an insight to treat cancer *in vivo* by labeling gold nanoparticles with antibodies specific to cancer cells, thereby loading higher concentration in cancer cells. Once internalized, local heating and thermo-ablations of tumor cells can be obtained.

3.4.2a Mechanism of non-magnetic heat loss

These high values of SAR at non-plasmon resonant *rf* frequencies are attributed by authors to be caused by resistive heating (Joule-Lenz) of gold nanoparticles because of small nanostructures [37]. Assuming nanoparticles to be conductors of a constant cross section, the heat generated by a gold nanoparticle under *rf* electric fields is estimated by

$$I^2 R = \sigma(\omega) [adE^2], \quad (3.10)$$

where $\sigma(\omega)$ is the Drude model conductivity of gold, E is the magnitude of the electric field, a is the area of the cross section of the gold nanoparticle and d is its size. Although these reports are impressive and indicate a potential for clinical hyperthermia, underlying physical mechanisms behind the *rf* heating of gold nanoparticles are not clear and should be explicated. On careful analysis of the theoretical physics at the nanoscale, accounting such high values for SAR to ohmic or Joule-Lenz heating is not realistic. Pierce performed numerical modeling studies to calculate electric field in and around a gold nanoparticle, but could not get high enough volume power density values to account for the high heating rates reported [91]. The other possible heat loss could be due to the frictional losses because of viscosity in the dispersion medium. Such viscous losses are also analyzed, but the drift velocity induced by Coulombic forces, is not enough to induce a collision to result in such energy dissipation and thus could not account for the heat loss [91].

3.4.2b Polarization losses at the nanoparticle

Studies have been done to show that none of the established theories including dielectric losses from the purified and impurified samples can endorse the notion of *rf* heating of gold nanoparticles [92]. However if such dielectric losses are enhanced due to the ambience of the nanoparticle, then such high losses reported on the gold nanoparticle could be addressed. Our research group is also working towards elucidating this heating mechanism and the dielectric properties of the nanoparticle. In order to analyze the polarization of a nanoparticle, we used the quasi-static application mode in the AC/DC module of COMSOL Multiphysics 3.5a and studied the field distribution on the nanoparticle. COMSOL Multiphysics is a Finite Element Method

(FEM) solving tool. The equation used by COMSOL for the analysis is the continuity equation in the following form

$$-\nabla \cdot ((\sigma + j\omega\epsilon_0\epsilon_r)\nabla V - J^e) = 0, \quad (3.11)$$

where σ is the electrical conductivity, ϵ is the permittivity, ω is the angular frequency, V is the electric potential and J_e is the external current density. Assuming spherical particle configuration as shown in Figure 3-11, with appropriate boundary and subdomain conditions applied to all active boundaries including material interfaces and physical boundaries, at an input potential of one Volt, the polarization plots for a metallic particle and a dielectric particle are obtained as shown in Figure 3-12.

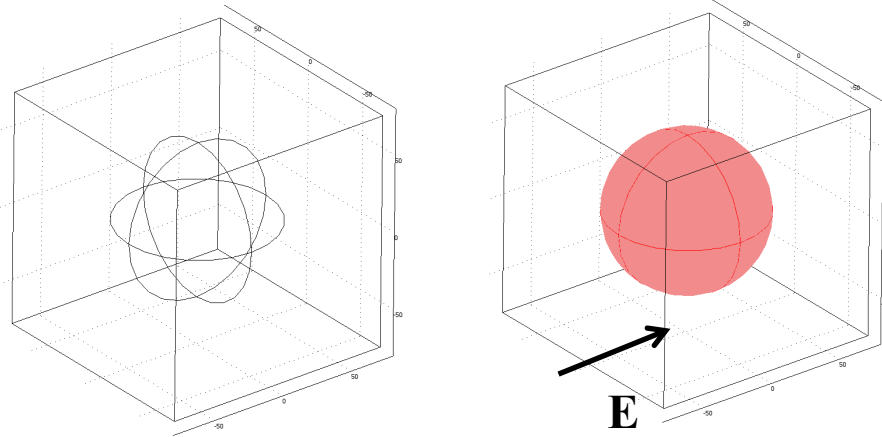


Figure 3-11 Subdomain-Boundaries of the nanoparticle with direction of applied electric field shown

Figure 3-12 shows the absolute magnitude of the electric field distribution around a spherical nanoparticle. Figure 3-12(a) shows the case of a metallic nanoparticle where the enhanced field caps at the poles on the particles are observed. This leads to a dipole formation on the particles resulting in polarization under the influence of the field. A similar polarization is observed on dielectric particles, marked by a shift in the axis of polarization by 90° .

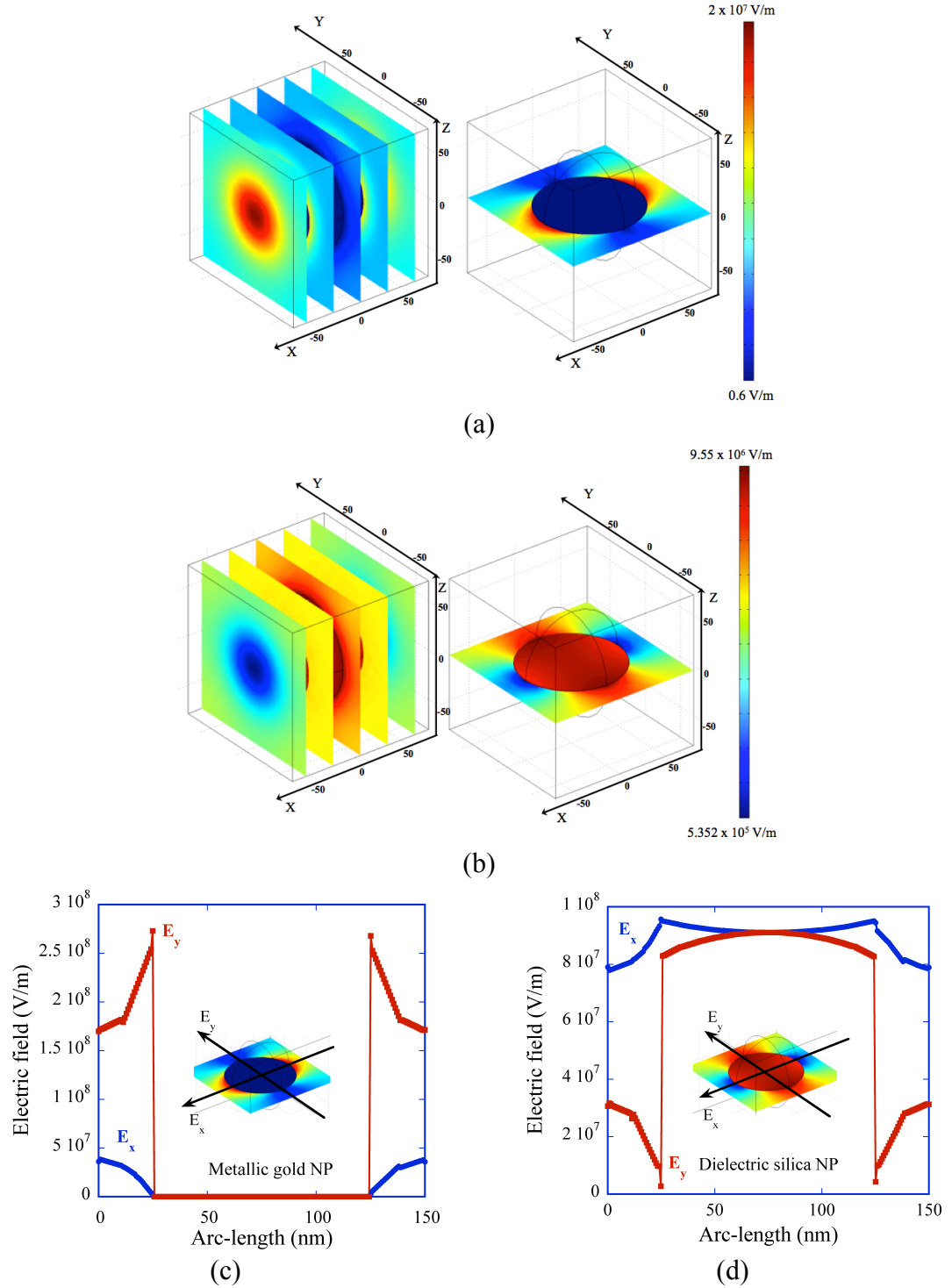


Figure 3-12 Electric field distribution around a nanoparticle and a slice plot in xy plane for (a) metallic gold nanoparticle (b) dielectric silica nanoparticle; Electric field magnitudes along x and y axis for (c) metallic and (d) dielectric particle

The magnitude of polarization as shown in Figure 3-12 is a function of conductivity and permittivity of the particle. With this polarization under the influence of an external electric field, the dipole field around the particles can interact with the ions at the particle's surface due to the surrounding electrolyte solution.

An electrical double layer exists at the particle-electrolyte interface due to the redistribution of ions by the surface charge/potential of the colloidal particles. The interaction of the dipole fields with the double layer could result in rf loss. The electric double layer and charge around the particle is shown in Figure 3-13.

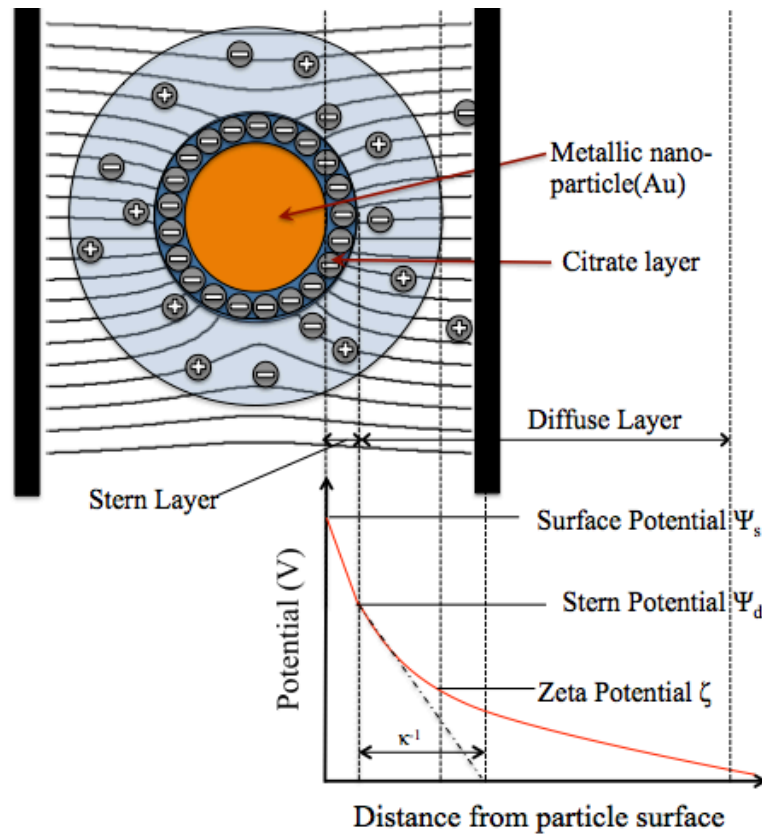


Figure 3-13 Electrical double layer around particle showing redistribution of the charges around nanoparticle due to the surface charge

The effective conductivity of the double layer as distribution of the ions of the solution around the particle as a function of radius and distance away from the surface was derived as

$$\sigma_d(r, a) = \frac{3}{2} \left(\frac{e^2}{k_B T} D n_\infty \right) \cosh \left[\psi_s \left(\frac{a}{r} \right) e^{-\kappa a \left(\frac{r}{a} - 1 \right)} \right], \quad (3.12)$$

where D is the diffusivity of the particle, n_0 is the bulk concentration, ψ_s is the surface potential and κ^{-1} is the Debye length *i.e.*, the thickness of double layer around the particle. This effective conductivity of the double layer has been used to model the heat loss associated with such particles in alternating electric fields.

3.4.3 Carbon Nanotube Hyperthermia

Owing to their varied surface chemistry and distinctive thermal properties, carbon nanotubes emerge as very adaptable candidates to be used in nanomedicine. Carbon nanotubes have been shown to act as strong optical absorbers in near infra-red light. Nanophotothermolysis is the term used for laser-facilitated ablation of cancer cells. Nanophotothermolysis of tumors mediated by intracellular internalization of carbon-nanotubes have been used in *in vitro* [93] and *in vivo* [94, 95] studies. Recently, carbon nanotubes have also been reported to release heat significantly under capacitively coupled *rf* fields [96]. Such an approach also opens the door to a clinical technique for hyperthermia, however bio-cytotoxicity issues of carbon nanotubes must be addressed.

3.5 CONCEPT OF VOLUME FRACTION

While working with nanoparticles suspended as colloidal mixtures, the concept of volume fraction is very important as it gives us information about the total mass/volume of material of the nanoparticle present in the sample which contributes to the *rf* heat enhancement. Volume fraction of a constituent in a mixture is defined as the ratio of volume of the constituent to the sum of volumes of all constituents prior to mixing. The concentration of the nanoparticle sample C (mg/mL) is identified as

$$C = \rho N_d v_{NP}, \quad (3.13)$$

where N_d is the particle number density (particles/mL), ρ is the material density of the particle, and v_{np} is the volume of one nanoparticle. From the definition, the volume fraction V_f of N nanoparticles in a colloidal suspension is the ratio of the total volume of nanoparticles V_{NP} in the suspension to the total volume of suspension V_{TOT} and is expressed as

$$V_f = \frac{V_{NP}}{V_{TOT}} = \frac{v_{NP} N}{V_{TOT}} = \frac{v_{NP} N_d V_{TOT}}{V_{TOT}} = v_{NP} N_d = \frac{C}{\rho}. \quad (3.14)$$

3.6 SAR STUDIES ON NANOPARTICLES

Simply increasing field strength and frequency cannot increase the heating efficiency of the nanoparticles, as higher values would result in the inductive heating of the healthy tissue. There are already clinically established upper limits of the frequency and magnetic field strength product $f.H$. Heating related properties with regard to SAR values of magnetic nanoparticles have been studied for many years and a significant progress in employing magnetic particles even in clinical applications can be seen. However, the caloric contribution of the dispersion medium cannot be ignored for

precise SAR calculations. The quantification of heat from the nanoparticles could be done as

$$SAR = C \left(\frac{\Delta T}{\Delta t} \right) \frac{mass_{nanofluid}}{mass_{nanoparticles}}. \quad (3.15)$$

As mentioned in section 2.4, SAR was formerly presented as a parameter describing the energy dose absorbed by a body when irradiated by an *rf* electromagnetic wave. Subsequently it was implemented to describe the *rf* loss enhancement due to nanoparticles when nanoparticle enhanced heating studies were performed. For magnetic and non-magnetic nanoparticles, power loss is proportional to $fH^2\chi''(f)$ and $\sigma(f)E^2$, respectively. For the radio-frequency range, χ'' and σ has no frequency dependence. Thus, normalization must be done with fH^2 and E^2 factors for magnetic and electric SARs, respectively for comparison and evaluation purposes. The un-normalized SAR of the magnetic nanoparticle can thus be expressed as

$$SAR_M = \frac{\pi\mu_0\chi''}{\rho_{NP}} f |H_z|^2, \quad (3.16)$$

where ρ_{NP} is the density of the nanoparticle sample. Many groups have reported the un-normalized SAR values for such magnetic nanoparticles for different field strengths and frequencies within a wide range of 15 to 1200 W/g.[29-31, 81, 82, 84-86] At a certain electric field, SAR for a nanoparticle heated in the field can be calculated from the power loss P as

$$SAR_E = 0.5 \left(\frac{\sigma_{NP}}{\rho_{NP}} \right) |E_L|^2. \quad (3.17)$$

Here ρ_{NP} is the mass density of the nanoparticle sample. Limits for electric fields and frequency should be clinically set, so that heating is controlled and safe for the human body.

3.7 CLINICAL TRIALS USING NANOPARTICLES

Clinical trials of hyperthermia along with chemotherapy using a magnetic field applicator as shown in Figure 3-14 have already been successfully achieved [81]. The feasibility of the thermotherapy using superparamagnetic ferrite nanoparticles with concentration of 112 mg/mL has been studied to assess an imaging based approach for non-invasive estimation of three-dimensional temperature distribution in glioblastoma patients. The assessment of such a study is shown in Figure 3-15 [81].



Figure 3-14 Clinical magnetic field applicator for hyperthermia

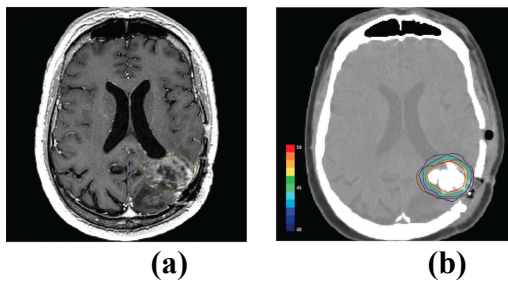


Figure 3-15 (a) Preoperative MRI with tumor area identified (b) Iron oxide nanoparticles injected with isothermal lines showing the calculated intra-tumoral temperatures.

The hyperthermia was performed using an alternating magnetic field with a frequency of 100 kHz and variable field strength of 2.5-18 kA/m. Iron oxide nanoparticles were injected in the tumor sites of glioblastoma patients. Thermotherapy was well tolerated at magnetic field strengths of an average 8kA/m and the maximum intra-tumoral temperatures of 42.4-49.5 °C were obtained. The isothermal curves represent the estimated intra-tumoral temperatures. SAR of 718 W/kg was obtained at 100 kHz.[81]

3.8 DESIGN OF MULTIFUNCTIONAL NANOBIOCONJUGATED VECTORS

3.8.1 Hyperthermia with other modalities

Even though, hyperthermia can be used by itself to shrink and even completely eradicate malignant tumors, most of the times, the results are temporary and tumors show regrowth and come back as referred in Section 3.1.3. With the effectiveness of oncological therapeutics like chemotherapy and radiotherapy identified, hyperthermia can certainly be used in conjunction with such cancer treatment modalities [97]. Such biological rationale for a synergetic combination of hyperthermia and radio or chemotherapy is being evaluated. The complementary effect is due to the sensitivity of cells in hypoxic and acidic areas prevalent in cancers, which are radiation-resistant. Heat has a sensitizing effect to radiation therapy [98]. Hyperthermia increases the blood flow that causes tissue oxygenation and thus increases the radio sensitivity. At milder temperatures, hyperthermia increases perfusion in the cancer lesions, which increases drug delivery and oxygenation enabling radiotherapy to be very effective if used in conjunction. In a similar fashion, delivering adequate amounts of chemotherapeutic

drugs to deep-seated solid tumors is very difficult. Due to the increased blood flow from hyperthermia, the intracellular drug uptake and intra-tumor drug concentration increases thereby providing complementary synergetic effects to the cancer treatment. These advantages from the combined therapeutics have led many researchers to conduct investigations on the effectiveness of radio-chemotherapy and the use of nanomedicine to engineer a rational approach for the cancer modality.

3.8.2 Design of nanostage vectors

Nanomedicine has allowed novel effective cancer treatment modalities involving drug delivery, imaging and hyperthermia simultaneously. The overall objective is to selectively target drug delivery to malignant tumors and to minimize drug delivery to critical normal tissues. With the design of nanovectors, the idea of temperature-triggered drug release has been proposed. Figure 3-16 shows the realization of magnetically vectored nanocapsules for tumor penetration and remotely switchable on-demand drug release.[32]

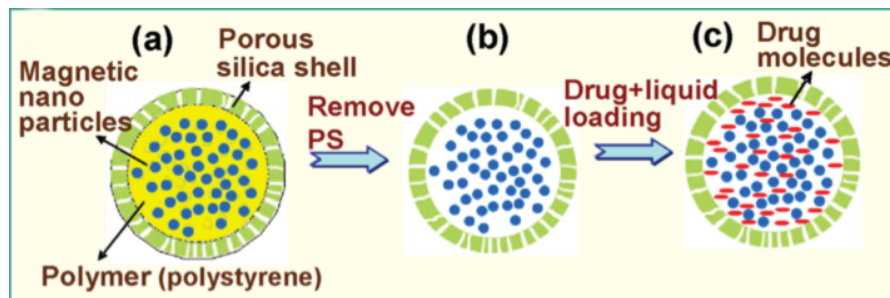


Figure 3-16 Fabrication of porous silica magnetic nanocapsules as a chemotherapeutic synergetic drug carrier

Ten nm magnetic nanoparticles of iron oxide are incorporated into a polystyrene sphere. The polystyrene sphere is then encapsulated in a porous silica shell capsule of 100-150 nm diameter. The polystyrene polymer is then dissolved within the capsule

and the hydrophobic or hydrophilic chemotherapeutic drug molecules like Camptothecin, Doxorubicin, etc. are loaded. The porosity of silica shells is adjusted to be minimally permeable to the loaded drug carrying solutions without an external magnetic field, but on-demand permeable to the application of the remote magnetic field. Housing the drugs in hydrophilic porous silica shells makes them inert to microphages, thus preventing their removal from the blood stream. However these nanocapsules could be guided to tumor sites using a magnetic field or could be functionalized using cancer specific antibodies, dendrimers, etc., so that they can reach the target lesions systemically. The magnetic field results in hyperthermia of the nanoparticles, which raises the temperature of the drug liquid and thus helps them release into the tumor sites. Once released into the tumor, the nanoparticles can still undergo hyperthermia and the drug molecules are delivered resulting in combined thermal and chemotherapy.

The idea is to systemically inject bio-conjugated nanoconstructs with cancer specific targeting moieties attached into the blood stream as shown in Figure 3-17. Pores of discoidal and hemispherical silicon nanoconstructs have been successfully loaded with MRI contrast agents [99]. These nanoconstructs could be loaded with iron-oxide nanoparticles and functionalized using natural receptor ligands, peptide ligands, whole antibodies, aptamers, etc., thereby actively targeting them into cancer cells [26]. Thus these nanoparticles are laden into targeted lesions, which is ensured by enhanced contrast imaging; alternating electromagnetic fields can be applied resulting in selective hyperthermia and ablation. Accordingly using such nanoconstructs, targeting, imaging and hyperthermia can be concurrently achieved. Another example is a liposomal drug

delivery in which mild temperature sensitive liposomes are used to co-encapsulate drugs, imaging contrast molecules and nanoparticles and then systemically injected and guided to the tumor sites as shown in Figure 3-18 [100]. The co-release of MRI contrast agents, the magnetic nanoparticles and the drug molecules provides visualization, hyperthermia and quantification of chemotherapeutics drug release in a non-invasive fashion.

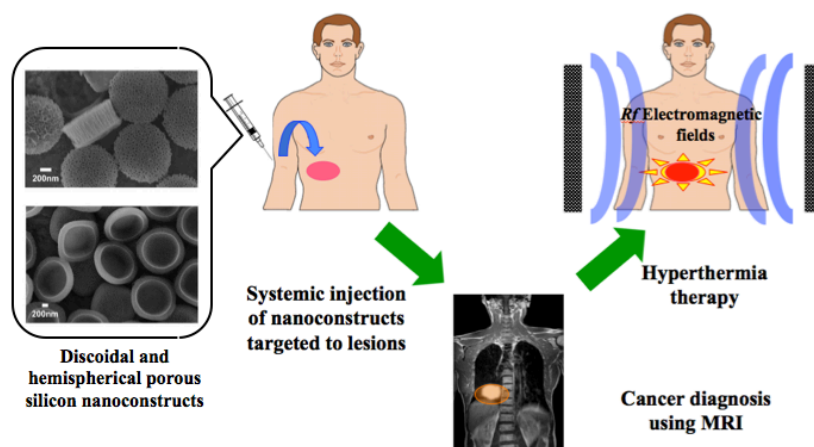


Figure 3-17 Cancer treatment philosophy using systemic injection of nanoconstructs loaded with MRI contrast agents and nanoparticles

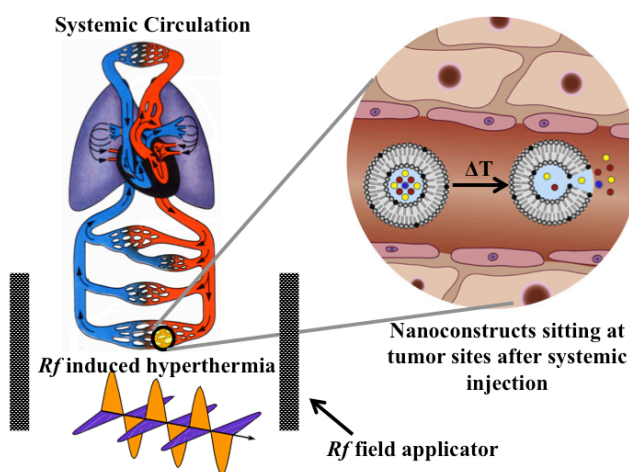


Figure 3-18 Schematic representation of temperature-induced release from temperature sensitive liposome nanocapsules

Chapter 4 Problem Statement

Biological nonlinear response has been linked with enzyme activities, cell membranes, ion-channels, etc. However, to identify such distinctive biological nonlinearities using any electrode arrangement, the intrinsic nonlinear effect from electrode-electrolyte interface should be well accounted. The conventional technique of single tone harmonic distortion measurements is not a very sensitive technique for low power biological nonlinear response investigation. In this work, the Intermodulation Distortion (IMD) technique is used to investigate biological non-linearity owing to its higher sensitivity to probe low power nonlinear response. Preliminary measurements were done to understand the behavior of electrolytes and buffers. The analysis of the electrode-electrolyte double layer model is done and a correlation between ion concentration and double layer impedance is derived. The method can thus be advantageously utilized to investigate bio-electro-chemical signatures of cells and microorganisms arising from cellular respiration and other metabolic activities.

Besides the rf induced nonlinear effects as bio-chemical signatures, rf induced thermal effects have also been suggested for cancer therapeutics. Both metallic and magnetic nanoparticles have been reported to enhance the heat specifically at non-resonant rf fields. However mass and size requirements for such nanoparticles for hyperthermia in tumors of different sizes are not yet well established. The objective is to investigate and optimize the properties and heating efficiency of nanoparticles and engineered nanoconstructs to study rf induced hyperthermia. Unlike DC situations, the rf electric and magnetic fields cannot be separated from each other and are linked to each other using Maxwell's equations. Thus, an attempt to exploit both electric fields as

well as magnetic fields for hyperthermia is done in this work. An *rf* heating system using the electrical resonance technique is developed and deployed.

Further studies must be done to perform dosimetric analysis for tissues, medium and nano-constructs. It is very significant to understand exposure levels and absorption of *rf* energy. For *rf* frequencies, the specific absorption rate (SAR) is considered as the dosimetric measure and its determination is critical to examine various parameters including exposure time, power output from a single nanoparticle point source and the estimated total mass of nanoparticles required to heat the total targeted tumor volume. SAR is required to identify the feasibility of substantial heating rates for concerned tumor volumes. To validate the notion about SAR, modeling using calorimetry and electromagnetics is desired. Such an approach will lead to more accurate SAR measurements, but needs to be well normalized to frequency and magnetic field strength, so that the comparison between different studies including different clinical and *in vitro* setups could be performed. At a particular frequency, comparison of heating rates of nanoparticles and tissues in both the electric and magnetic field should be performed to compare the superiority and the mechanism. The challenge is to deliver the adequate heat energy to the tumor site and the ability to obtain sustained temperatures. Additionally, it is substantial to understand how various body fluids and *in vivo* environments can affect SAR. Thus, there is a significant need to investigate hyperthermia of the nanoparticles dispersed in conductive biological buffers and their surface modification using physiologically relevant molecules like proteins.

Chapter 5 *Rf* Intermodulation distortion measurement setup

5.1 INTRODUCTION

Nonlinear dielectric spectroscopy is a technique by which harmonics generated by a dielectric (like biological samples) in response to an external sinusoidal field excitation can be measured. The objective is to study the electrical properties of charged-surface/electrolyte interfaces that exist at cell membranes, planar electrodes and nanoparticle's surface. All electrical systems behave in a nonlinear fashion in some way. The non-linearity of solid-state devices are well studied, however passive elements like capacitors, resistors and inductors also become nonlinear when they reach their extreme operating regimes. To understand and identify the nonlinear behavior, the concept of superposition should be well understood. Linear systems have transfer functions such that they obey the superposition principle i.e., the ratio of the output to the input signal consisting of the sum of multiple elementary signals, which can be stated as the sum of the individual response of each elementary input signal. In mathematical terms, we can write it as follows

$$\begin{aligned} \text{If } y_1(t) = S_L[x_1(t)] \& y_2(t) = S_L[x_2(t)] \& x(t) = k_1x_1(t) + k_2x_2(t) \\ \text{then } y(t) = S_L[x(t)] &= k_1y_1(t) + k_2y_2(t). \end{aligned} \quad (5.1)$$

Systems that obey this theory are linear and those, which do not are non-linear. The conventional technique for studying nonlinearities is the measurement of the total harmonic distortion (THD), in which the system is driven by a single-tone input signal as shown in Figure 5-1(a). Due to the nonlinear characteristics of the transfer functions, higher order spectral components are present in the output signals. Such

signals, when Fourier-transformed, appear to also contain second, third, and higher order harmonics. The mathematics behind such phenomena can be explained using a hypothetical non-ohmic resistor (which is not linear) and its transfer function is given as $i = aV + bV^2 + cV^3$, where a , b and c are real numbers. For a voltage excitation of $V_s = v(t) = V \cos \omega t$, the following output current components are generated:

$$i_a(t) = av(t) = aV \cos \omega t, \quad (5.2)$$

$$i_b(t) = bv^2(t) = bV^2 \cos^2 \omega t = \frac{b}{2} + \frac{b}{2} V^2 \cos 2\omega t, \quad (5.3)$$

$$i_c(t) = cv^3(t) = cV^3 \cos^3 \omega t = \frac{c}{4} V^3 \cos 3\omega t + \frac{3c}{4} V^3 \cos \omega t. \quad (5.4)$$

Therefore, from the above analysis we see that because of the nonlinear transfer function, the second and third order spectral components are introduced into the output.

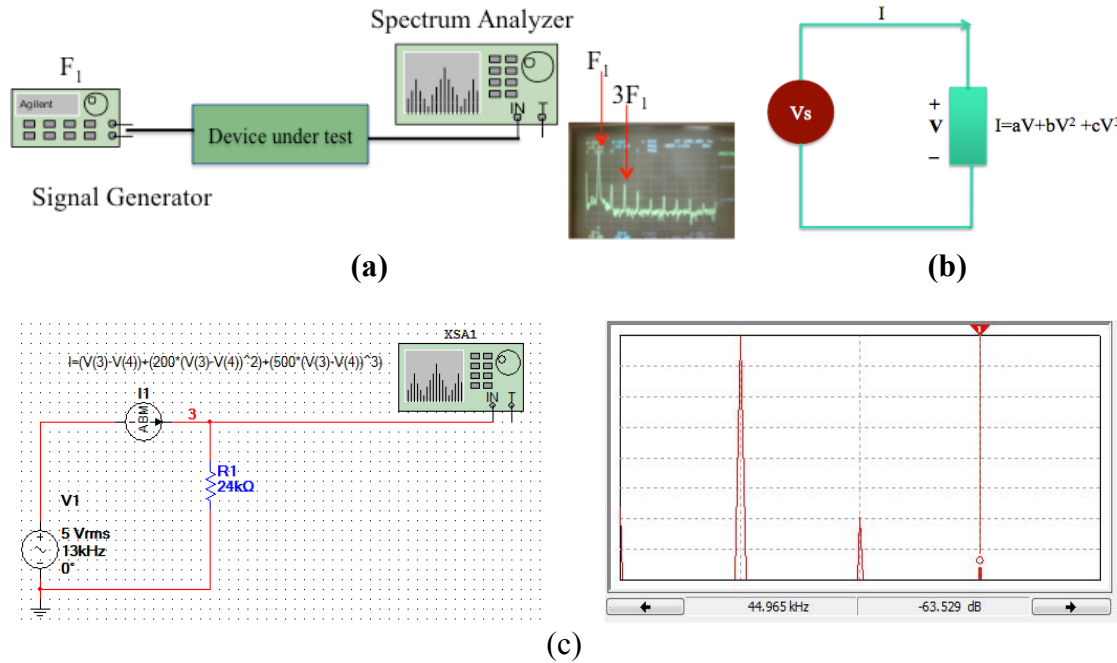


Figure 5-1 (a) Total Harmonic Distortion (b) Non-ohmic resistor (c) Multisim simulation for a nonlinear circuit element

When this output current is Fourier transformed, the output spectrum is marked by a spectral regrowth beyond the linear component, giving rise to second and third harmonics as 2ω and 3ω components. Multisim analysis for a nonlinear electrical element of transfer function $i = v + 200v^2 + 500v^3$ was performed to understand the concept of THD for nonlinear spectrum analysis. Results are shown in Figure 5-1(c). However as higher order harmonics have decreasingly small amplitudes and are buried under the vector analyzer's noise, total harmonic distortions become difficult to detect and study. In addition, studying higher order harmonics in some cases, becomes really impossible due to the bandwidth limitation of the spectrum analyzer. So higher power levels are required, which themselves have a tendency to drive the system itself into a nonlinear system.

In the present work, we realized a very sensitive setup based on the detection of intermodulation distortion (IMD) peaks. This technique has already been widely accepted as a comprehensive method to study radiofrequency and microwave nonlinearities in electronic circuits [101] and also in superconductors [102]. When a system with nonlinear transfer function is subjected to a dual frequency excitation, it produces several nonlinear components showing up as beat frequencies of even and odd orders referred to as intermodulation products. These components occur as sidebands in the output power response. To understand this, the same example of a nonlinear resistor can be considered which in this case is exposed to a dual-tone input. For a voltage excitation of $V_s = v(t) = V_1 \cos \omega_1 t + V_2 \cos \omega_2 t$, the following output current components are generated:

$$i_a(t) = av(t) = aV_1 \cos \omega_1 t + aV_2 \cos \omega_2 t \quad (5.5)$$

$$i_b(t) = bv^2(t) = b[V_1 \cos \omega_1 t + V_2 \cos \omega_2 t]^2$$

$$= \frac{b}{2} \left[V_1^2 + V_2^2 + V_1^2 \cos 2\omega_1 t + V_2^2 \cos 2\omega_2 t + 2V_1 V_2 (\cos(\omega_1 - \omega_2)t + \cos(\omega_1 + \omega_2)t) \right] \quad (5.6)$$

$$i_c(t) = cv^3(t) = c[V_1 \cos \omega_1 t + V_2 \cos \omega_2 t]^3$$

$$= \frac{c}{4} \left[V_1^3 \cos 3\omega_1 t + V_2^3 \cos 3\omega_2 t + 3V_1^2 V_2 [\cos(2\omega_1 + \omega_2)t + \cos(2\omega_1 - \omega_2)t] + 3V_1 V_2^2 [\cos(\omega_1 + 2\omega_2)t + \cos(\omega_1 - 2\omega_2)t] + 3(V_1^3 + 2V_1 V_2^2) \cos \omega_1 t + 3(V_2^3 + 2V_1^2 V_2) \cos \omega_2 t \right]. \quad (5.7)$$

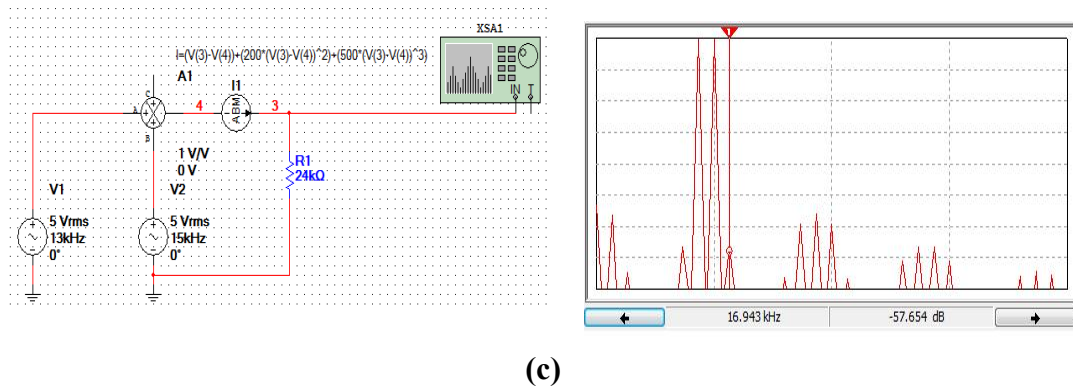
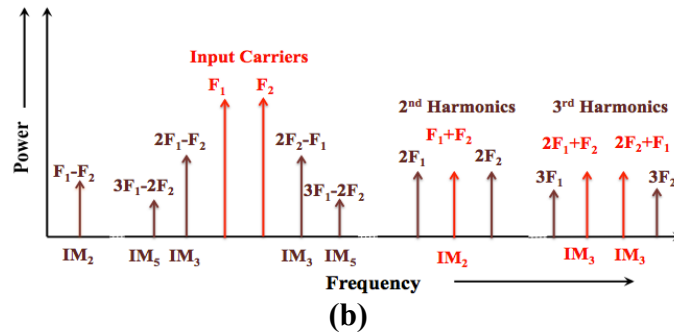
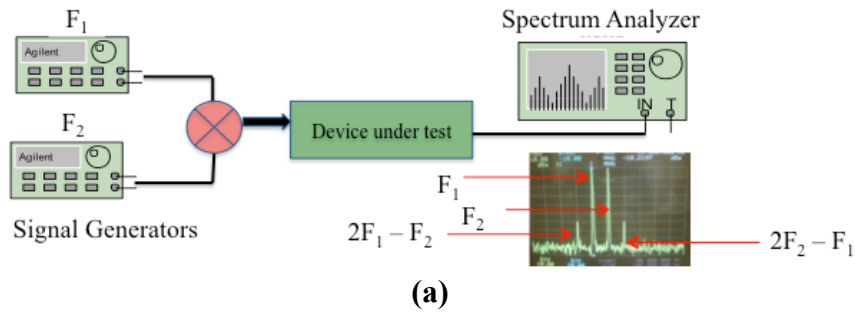


Figure 5-2 (a) Intermodulation Distortion (b) A complete intermodulation distortion spectrum (c) Multisim simulation for a nonlinear circuit element

The Fourier-transformed spectrum for the outputs (Equations 5.5-5.7) using dual tone excitation creates two linear outputs and six nonlinear components arranged in four different frequencies. The sidebands $2\omega_1 - \omega_2$ and $2\omega_2 - \omega_1$ are known as third order intermodulation products (IMP). From now onwards, the frequency in radians ω will be replaced by the frequency f . Typically, in the case of nonlinearity, an IMD spectrum contains many higher order peaks; however to conserve bandwidth only the fundamental (f_1 and f_2) and third order IMP peaks ($2f_1 - f_2$ and $2f_2 - f_1$) are measured in our case as a function of the input power. A very significant advantage of the IMD technique, related to its sensitivity, is its capability of probing nonlinearities at very low power levels, which allows avoidance of thermal effects that occurs at high power levels. Otherwise, like in the case of THD, the system should be driven at a higher power to observe harmonics, which itself might induce non-linearity into the system. Multisim analysis for the similar nonlinear electrical element with transfer function $i = v + 200v^2 + 500v^3$ is performed to comprehend the concept of IMD for nonlinear spectrum analysis. It is observed that to study the nonlinear behavior for the same element, reference to the third order IMP peak using two frequencies could be made which is relatively at a higher power level than the third harmonic peak for the same element using one frequency.

Thus, a current-voltage response represented by the transfer function $i = H(v)$ can be expanded into a power series: $i = a_1v + a_2v^2 + a_3v^3 + \dots$. For excitation by a two-tone signal of the same amplitude: $v = v_{in}[\cos(\omega_1t) + \cos(\omega_2t)]$, using Equation 5.5, the linear output power P_{linear} at the fundamental frequency is proportional to the input power P_{in} [101] and can be expressed as

$$P_{linear} = \frac{1}{2} a_1^2 v_{in}^2 = k P_{in}. \quad (5.8)$$

Hence,

$$v_{in}^2 = \frac{2kP_{in}}{a_1^2}. \quad (5.9)$$

Considering the third order intermodulation product from Equation 5.7, the third-order IMP's output power P_{3IMP} [101] can be written as

$$P_{3IMP} = \frac{9}{32} a_3^2 v_{in}^6. \quad (5.10)$$

From Equation 5.9, the third order IMP's output power, can be re-written as

$$P_{3IMP} = \frac{9}{4} \left(\frac{k}{a_1^2} \right)^3 a_3^2 P_{in}^3, \quad (5.11)$$

where a_1 and a_3 are expansion coefficients and k is a parameter of the measuring system. From Equations 5.8 and 5.11, it can be inferred that for each dB rise in the input power, the fundamental and third-order IMPs increase by 1 dB and 3 dB, respectively.

The output power, when plotted against the input power, should follow the 1-dB/dB slope line for fundamentals (f_1 and f_2) and 3-dB/dB slope line for the third-order IMP sidebands ($2f_1-f_2$ and $2f_2-f_1$) as shown in Figure 5-3. An important parameter while referring to IMD is the third order intercept point (TOI), which is an imaginary point obtained by the intersection of extrapolated 1dB/dB slope line of the output fundamental power and the extrapolated 3-dB/dB slope line of the IMD power. The third order intercept point is a property of the system's transfer function.

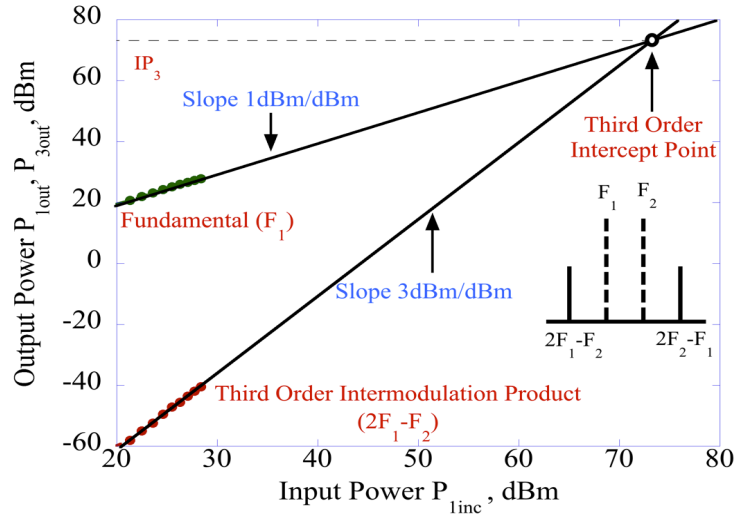


Figure 5-3 Fundamental and IMD input power per tone

5.2 INTERMODULATION DISTORTION SETUP TO MEASURE BIOLOGICAL NONLINEARITY

The IMD setup as shown in Figure 5-4 is constructed for liquid samples [103]. An ultra-low distortion function generator DS-360 (Stanford Research Systems) operated in two-tone mode was used to drive an LCR parallel circuit resonator (Figure 5-5) [103].

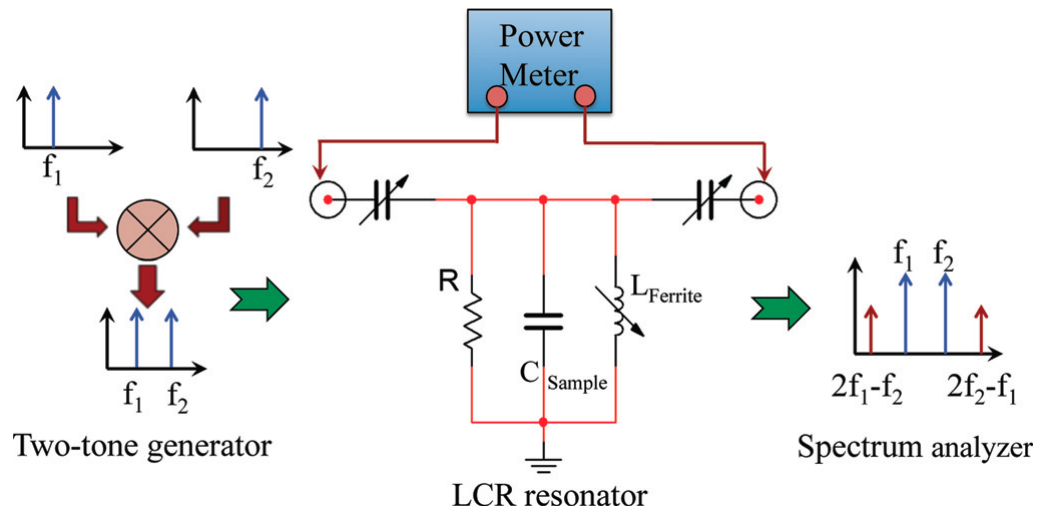


Figure 5-4 Two-tone intermodulation distortion measurement setup

An Agilent power meter N1912A monitored the input and output power signals of the resonator. The output frequency response was measured by the spectrum analyzer (SR785; Stanford Research Systems). The sample container was built as a capacitor, an RC component of an LCR resonator, and consists of parallel plate gold electrodes (Figure 5.6 (a) and (b)). Capacitor electrodes were made of a gold layer (2000 Å) deposited on a glass substrate with a Cr adhesion layer. These planar electrodes of size 17.5 mm × 15 mm were patterned using optical lithography and spin-coated at about 1000 rpm with a thin Teflon (DuPont-AF) layer for protection and insulation. Teflon on the electrodes ensures the absence of any net faradaic current through the capacitor cell, thus making the resistive component of the resonator relatively large. Spacers of neoprene rubber were used to separate the two plates of electrodes by 0.5 mm.

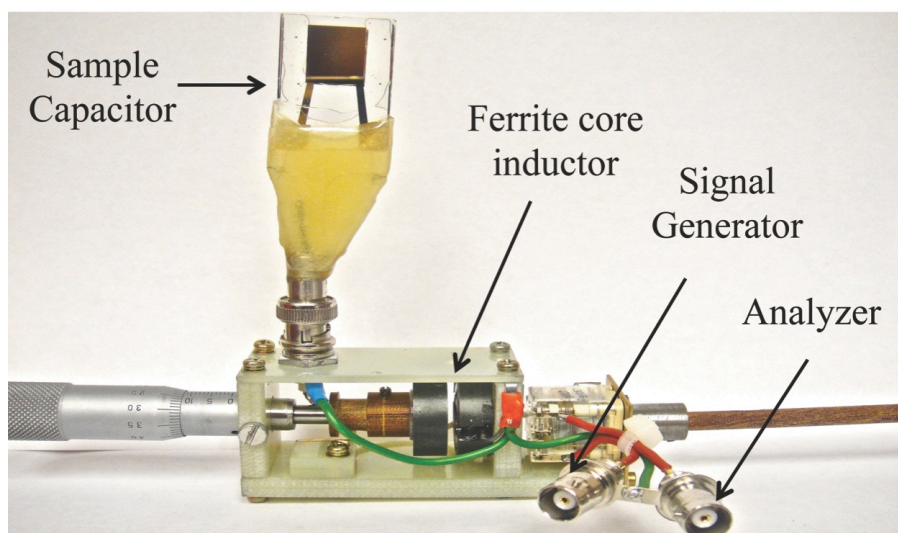


Figure 5-5 LCR resonator showing adjustable ferrite core-based inductor

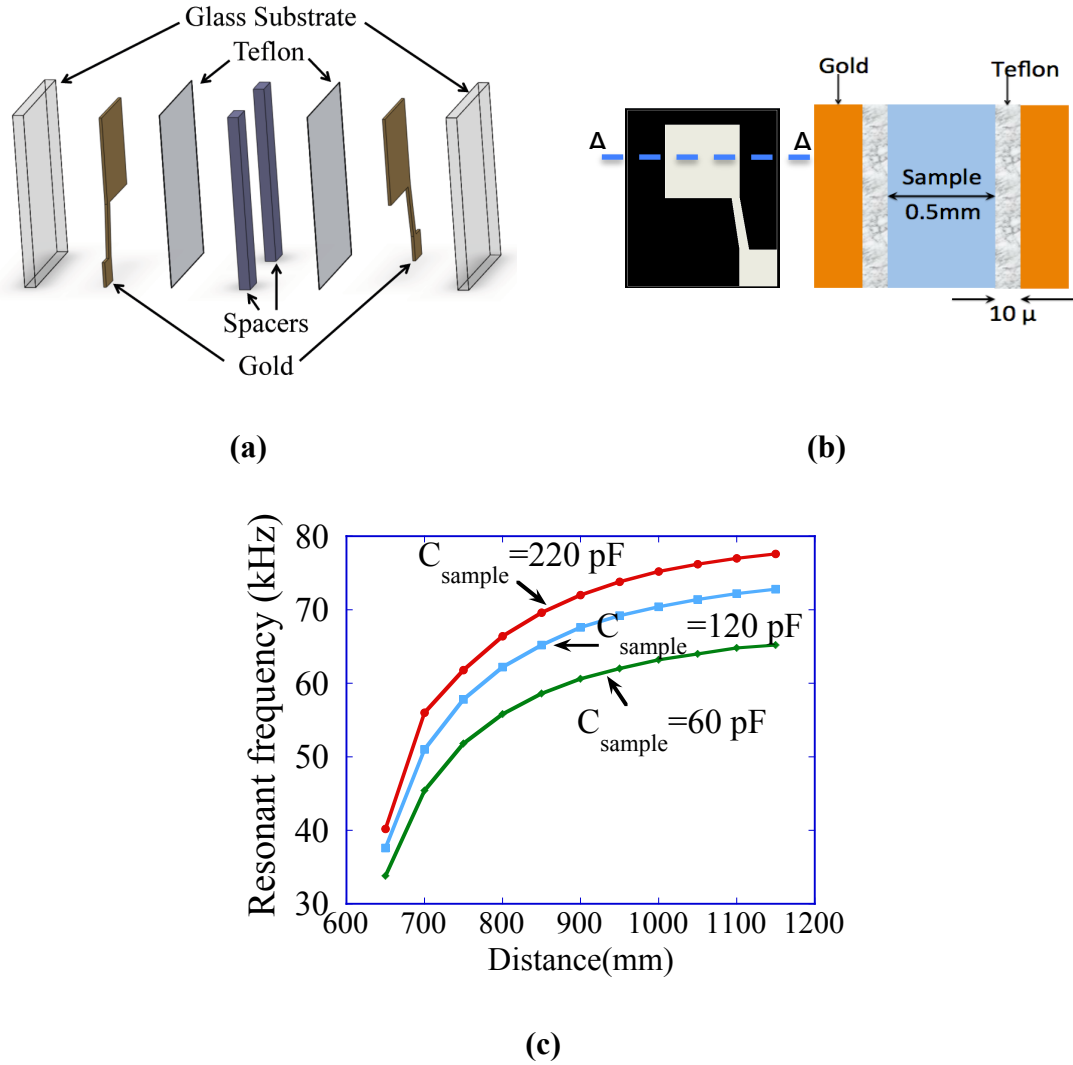


Figure 5-6 (a) Expanded view of the sample capacitor (b) Lateral and top view of the sample capacitor (c) Resonant frequency sweep *versus* distance between the ferrite cores for different sample capacitances

An equivalent circuit of such sample container comprises of five capacitances connected in series: two for the insulating layer, two for the interface double layers, and one for the solution. We assumed that the nonlinearity comes only from the capacitance and resistance of the double layers at the electrode interface with the solution. Other components such as the bulk electrolyte, Teflon layer, and inductor were assumed to be linear.

5.3 MEASUREMENT PROCEDURE

When the LCR circuit is tuned to the resonant frequency f_r , the impedance of the parallel resonator is equal to the resistance R of the sample capacitor. It results in the proportionality of the input and output power at resonance and makes the coefficient k in Equation 5.8 equal to 1. Any deviation from this k value will be a function of the resistive R component in the capacitor, which is large in this case because of the Teflon electrode coating. For each measured sample, the setup is first tuned to the resonant frequency f_r of the LCR resonator using a network analyzer. The resonance frequency can be selected from a wide kHz range by changing the separation between the ferrite cores, as shown in Figure 5-6(c). Once the f_r value is known, two tone signals at equal power can be selected to drive the resonator. These signals have two fundamental tones: f_1 and f_2 centered at the resonance peak, with a difference between f_1 and f_2 frequencies of approximately 100 Hz. The third-order IMPs $2f_1-f_2$ and $2f_2-f_1$ were observed where all the output signal frequencies f_1 , f_2 , $2f_1-f_2$ and $2f_2-f_1$ were within the pass-band of the resonator. By adjusting the input power, plot 1-dB and 3-dB slope lines were plotted and nonlinearity was hence analyzed. To identify the intermodulation spectrum of each sample, the power levels of the fundamental tone and the third-order IMPs at frequencies $2f_1-f_2$ and $2f_2-f_1$ were measured in the spectrum analyzer as a function of the resonator input power. At each input power, the frequency was adjusted to the resonant frequency and the third-order IMD sidebands peaks were monitored for the output power maximum.

Chapter 6 Results on bio-electrochemical nonlinearity

6.1 PRELIMINARY MEASUREMENTS WITH DI WATER

The first measurements were done with the sample capacitor filled with deionized water Nanopure Systems at 18 M Ω -m resistivity. No third-order IMPs were observed above the noise limit of -65 dBm, implying that there are no nonlinear effects in pure water in this power range; whatever was measured was under the limit of our sensitivity of -65 dBm.

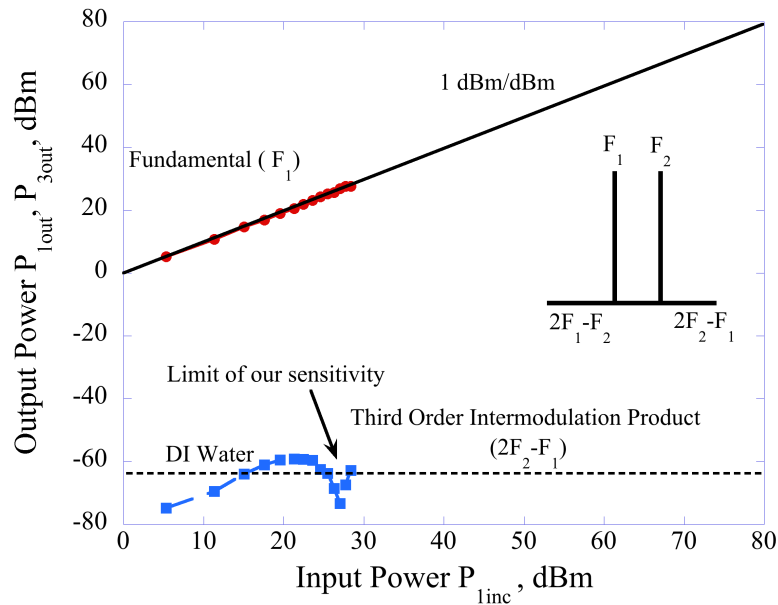


Figure 6-1 Output power for the fundamental and the third-order intermodulation product *versus* input power for DI Water

6.2 MEASUREMENTS WITH AQUEOUS SOLUTIONS OF NaCl

Next, the IMD spectra for 0.01M, 0.1M and 1M sodium chloride aqueous solutions were measured. As shown in Figure 6-2, for all concentrations of ions, the output power followed the standard 1-dB/dB slope line and 3-dB/dB slope line behavior between the fundamental and third-order IMP sidebands, respectively. The

two plots of slopes 1 and 3 for each sample were then extrapolated to determine the intersection points, called the third-order intercept points IP_3 , which can be treated as a figure of merit of the degree of nonlinearity. We found the IP_3 values to be dependent on ion concentration.

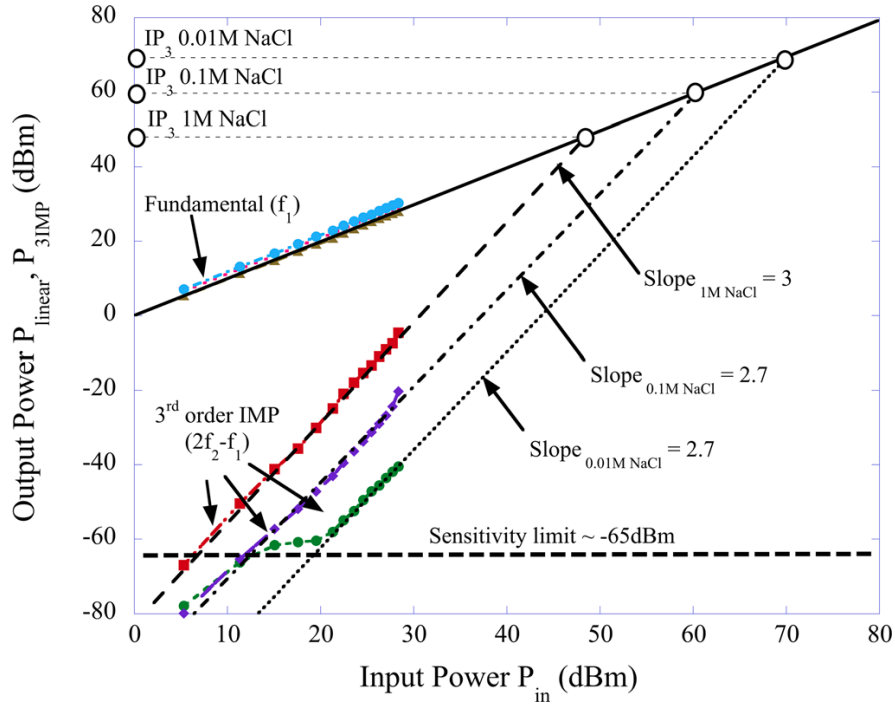


Figure 6-2 Output power for the fundamental and the third-order intermodulation product *versus* input power for 0.01 M NaCl, 0.1 M NaCl and 1M NaCl solutions

The higher the molar concentration of NaCl, the quicker is the onset of non-linearity in terms of input power. The nonlinear conductivity of the electrolyte could be accounted for such nonlinear behavior [66]. However, the input power is not high enough to onset non-linearity. Hence, to explore this non-linearity, further experiments were done with polyvalent electrolytes and under different frequency.

6.3 SUPPLEMENTAL MEASUREMENTS WITH VARYING VALENCY AND FREQUENCY

To understand the non-linearity from electrolytes, further supplemental experiments were done using polyvalent electrolytes. 0.1 M aqueous solutions for sodium chloride (NaCl), calcium chloride (CaCl_2) and lanthanum chloride (LaCl_3) were chosen as 1:1, 2:1 and 3:1 electrolytes. It is observed as shown in Figure 6-3 that with an increase in the valency of ions, the onset of non-linearity was quicker. It is suspected that it could be the effect of valency and concentrations and could be the nonlinear nature of the electrode-electrolyte interface. As the conductivity of electrode-electrolyte interface has ion concentration and valency dependence, electric double layer could attribute for these nonlinear impedance behavior.

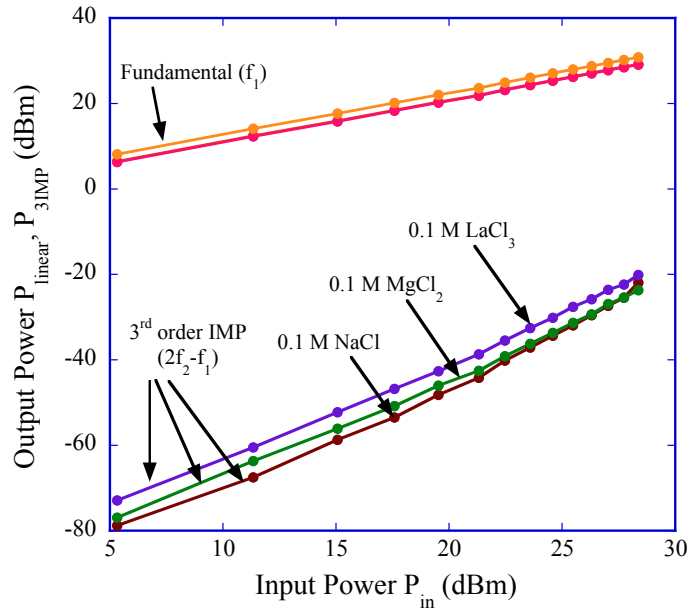


Figure 6-3 Output power for the fundamental and the third-order intermodulation product *versus* input power for aqueous solutions of 0.1 M NaCl, 0.1 M MgCl_2 and 0.1M LaCl_3

To further analyze this suspected non-linearity from electrode-electrolyte interface, we did another test by changing the resonant frequency of the resonator and thus driving the input power to the sample at different frequencies within the kHz range as presented in Figure 6-4. Thus, three frequencies 35, 50 and 80 kHz are used to study IMD on 0.1 M NaCl. A very distinct onset of nonlinearity as evident from the third order IMP's dependence on input power was observed at lower frequencies between 35 and 80 kHz. Until 15 dBm of input power, the third order IMPs for 80 kHz were under the sensitivity limit, however distinctive higher output power for third order IMPs at 35 and 50 kHz were observed. As double layer impedance also shows frequency dependence[104], this motivated us to study the nonlinear behavior of the electrode-electrolyte, which is addressed in detail in Section 6.5.

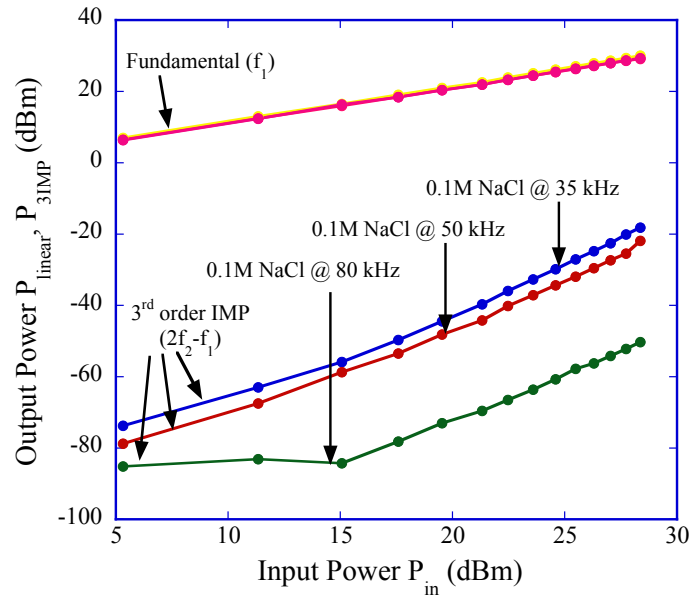


Figure 6-4 Output power for the fundamental and the third-order intermodulation product *versus* input power for aqueous solutions of 0.1 M NaCl at 35, 50 and 80 kHz

6.4 MEASUREMENT ON BUFFERS AND YEAST SAMPLES

The yeast species *Saccharomyces cerevisiae* were cultured in the Yeast Peptone Dextrose (YPD) media for growing yeast at 30°C for about 12-14 hours. The yeast cells are harvested from the media by centrifugation at 4200 rpm for about 20 minutes. The supernatant was discarded and the pellets were washed with Phosphate Buffer Saline (PBS) and then suspended in the PBS solution, pH adjusted to 7 and in deionized water. Samples of yeast cells were taken when they were in an exponential growth phase (approximately after 12 hours). IMD measurements as shown in Figure 6-5 with yeasts samples in PBS solution and in DI water revealed that at such low frequencies the non-linearity due to the electrode-electrolyte interface is dominant over the biological non-linearity and cannot be avoided.

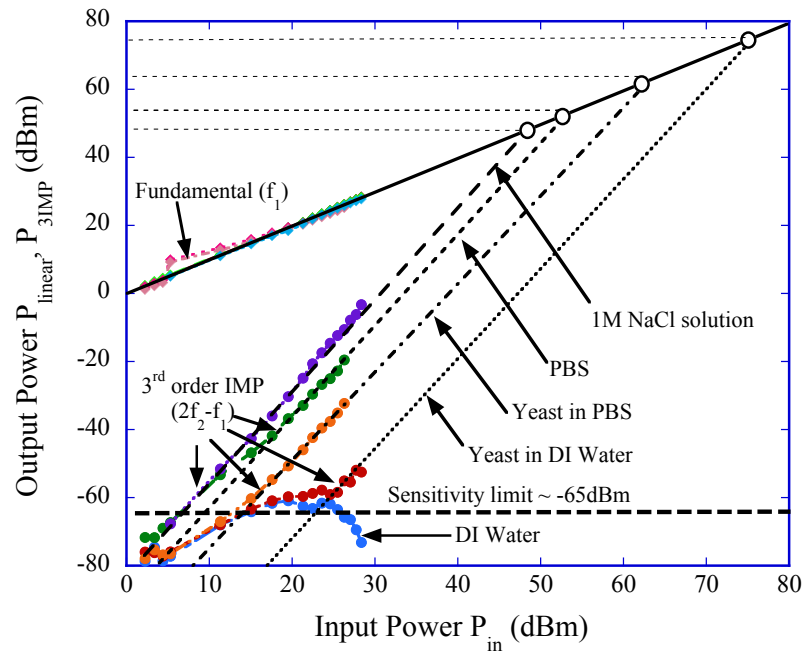


Figure 6-5 Output power for the fundamental and the third-order intermodulation product versus input power for 1 M NaCl, PBS and yeast cells suspended in PBS and DI Water

Figure 6-5, shows that yeast in DI water follows the trend of DI water, until the input power of 20 dBm, where there is a kink showing a nonlinear behavior other than water. Also the amplitudes of third order IMPs for the PBS buffer were higher than yeast in the PBS solution itself. This shows that the control solution itself is having nonlinear impedance at such frequencies and masks off the biological nonlinear effect, which has been reported by various other groups [15-22].

6.5 EXPLANATION OF NON-LINEARITY DUE TO ELECTRODE-ELECTROLYTE INTERFACE

From the measurements done with electrolytes, buffers and yeast samples, it is evident that at such low frequencies, the effects from the bio-electrolyte itself overshadow the biological non-linearity. Hence a model for non-linearity from the electrode-electrolyte interface is developed. This model justifies for variation in ion concentration of the electrolyte.

6.5.1 Double layer model for electrode-electrolyte interface.

A simple case of a symmetric binary electrolyte, ($z:z$) with dielectric constant ϵ and the same diffusivity D and valency z for cations and anions is considered. A pair of flat electrodes is placed in the electrolyte to form a capacitor. Both electrodes have the same surface potential, ψ_s , due to the electrochemical reaction with the electrolyte. Due to the surface potential, there is a spatial distribution of ion concentration near the surface resulting in the formation of an electrical double layer [105] as shown in Figure 6-6. Using Equations 5.23 and 5.4 taken from reference [105], the spatial distribution of ions is expressed as

$$n_{\pm}(x, \psi_s) = n_{\infty} \exp\left(\mp \frac{|z|e}{k_B T} \psi_s \exp(-\kappa x)\right). \quad (6.1)$$

Here n_+ and n_- are concentration values for cations and anions, respectively; n_{∞} is the ionic concentration in the bulk solution, k_B is Boltzman constant, T is the temperature and κ^{-1} is Debye length defined as the length where the potential distribution in a double layer is in equilibrium with the charge distribution of the ions. Debye length can be conveyed as

$$\kappa^{-1} = \left(\frac{\epsilon k_B T}{2e^2 z^2 n_{\infty}} \right)^{1/2}. \quad (6.2)$$

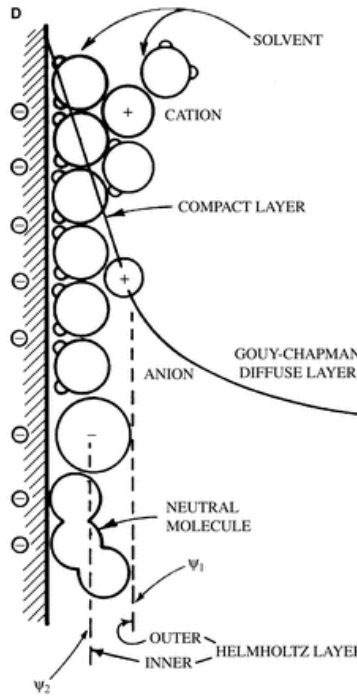


Figure 6-6 Schematic representation of the electrical double layer[106]

Local conductivity of an electrolyte is proportional to the ion concentration, which in our case leads to the expression (see Reference [107]'s Equation 6.73),

$$\sigma(x) = \frac{e^2}{k_B T} z^2 D(n_+(x) + n_-(x)). \quad (6.3)$$

Inserting Equation 6.1 into Equation 6.3, and using the relation $\cosh(z) = (\exp(z) + \exp(-z))/2$, Equation 6.3 can be expressed as

$$\sigma(x, \psi_s, v) = \gamma z^2 n_\infty \cosh(|z| \alpha(x) (\psi_s + v)). \quad (6.4)$$

Here v is an applied voltage to the gold electrodes, $\alpha(x) = \exp(-\kappa x)e/k_B T$, and $\gamma = 2e^2 D/k_B T$. Since ψ_s is a constant, σ is a nonlinear function of v . Under an applied field $E = v/\epsilon h$ (h is the distance between the two electrodes) in a time interval dt , a current $I = \sigma(x = \kappa^{-1}, v) v A / \epsilon h$ will flow through a plane, which is located at the κ^{-1} distance away from the surface and has an area of A . According to the continuity theorem, $\nabla J = -\partial \rho / \partial t$, this current will charge or discharge the double layer, resulting in a change of electric charge $dq = I dt$. It introduces a polarization current I_{cond} (displacement current) in the capacitor which can be written as

$$I_{\text{cond}}(v) = \gamma \left(\frac{A}{\epsilon h} \right) n_\infty \cosh[\alpha(\kappa^{-1})(\psi_s + v)] v. \quad (6.5)$$

Assuming valency $z=1$, this nonlinear function can be Taylor expanded at a fixed potential ψ_s up to the third order:

$$I_{\text{cond}}(v) = \gamma \left(\frac{A}{\epsilon h} \right) n_\infty \left[\cosh(\alpha \psi_s) v + \alpha \sinh(\alpha \psi_s) v^2 + \frac{\alpha^2}{2} \cosh(\alpha \psi_s) v^3 \right]. \quad (6.6)$$

From Equation 6.6 the third order coefficient of the series can be written as

$$a_3 = \frac{\gamma \alpha^2}{2} \left(\frac{A}{\epsilon h} \right) \cosh(\alpha \psi_s) n_\infty. \quad (6.7)$$

It is seen that a_3 is proportional to concentration n_∞ or to molarity M defined as $M=n_\infty/1000N_A$ (N_A is the Avogadro's number). The expression for the nonlinear capacitive current at the electrode electrolyte interface is derived from the surface charge density at the electrode electrolyte interface equation (Reference [105] Equation 5.52) as

$$q_s(v(t)) = 2[2\epsilon k_B T n_\infty]^{1/2} \sinh\left(\frac{|z|\alpha(\psi_s + v(t))}{2}\right). \quad (6.8)$$

The capacitive current I_{cap} density in the capacitor can be defined as a time derivative of surface charge density as

$$I_{cap}(v(t)) = \frac{dq_s}{dt} A, \quad (6.9)$$

and can be written as

$$\frac{dq_s}{dt} A = j\omega A [2\epsilon k_B T n_\infty]^{1/2} \cosh\left(\frac{|z|\alpha(\psi_s + v(t))}{2}\right) v(t). \quad (6.10)$$

The Taylor's expansion of capacitive current function is similar to the polarization current in Equation 6.6 as

$$I_{cap}(v) = j\omega \frac{\alpha A}{2} [2\epsilon k_B T n_\infty]^{1/2} \left[\cosh\left(\frac{\alpha}{2}\psi_s\right)v + \frac{\alpha}{2} \sinh\left(\frac{\alpha}{2}\psi_s\right)v^2 + \frac{\alpha^2}{4} \cosh\left(\frac{\alpha}{2}\psi_s\right)v^3 \right], \quad (6.11)$$

and the third order coefficient extracted from Equation 6.11 can be written as

$$a_3 = j \frac{\omega \alpha^3 A}{8} [2\epsilon k_B T]^{1/2} \cosh\left(\frac{\alpha}{2}\psi_s\right) \sqrt{n_\infty}. \quad (6.12)$$

Such a coefficient of the capacitive current is proportional to the square root of concentration. It is concluded that the expansion coefficients of the polarization and capacitive components of the double layer current have linear and square root proportionality to concentration, respectively.

6.5.2 Mathematical analysis of the electrode-electrolyte non-linearity

The IP_3 values for concentrations of 1M, 0.1M and 0.01M are noted in Table 6.1.

Table 6.1 P_{3IMP} and a_3 for respective molar concentrations

Molarity (M)	IP_3 (dBm)	P_{3IMP} (dBm)	a_3
0.01	69.2	-47.2	4.384×10^{-7}
0.1	59.6	-31.26	2.747×10^{-6}
1.0	47.5	-13.32	2.173×10^{-5}

From Equations 5.8 and 5.11, the relation between IP_3 and a_3 was found to be $a_3 = (2/3)a_1^3/IP_3$. The coefficient a_3 from the extrapolated IP_3 value [101], could be estimated but instead Equation 5.11 is used to calculate a_3 since it involves more reliable interpolated IMP data. Rearranging Equation 5.11, and substituting constants $k=1$, $a_1=1$, and using dBm units, a_3 can be expressed as

$$a_3 = \frac{2}{3} 10^{\frac{P_{3IMP}(dBm) - 3P_{in}(dBm)}{20}}. \quad (6.13)$$

To analyze the data, we selected three P_{3IMP} points for each molarity corresponding to the input power P_{in} of 25.48 dBm as shown in Figure 6-7; a_3 values were calculated using Equation 6.13 and are presented in Table 6.1. These three a_3 values are plotted *versus* molarity as circular dots in Figure 6-8. The electrical double layer model [103] derived in section 6.5.1 is used to interpret the results. The

expressions for polarization and capacitive currents have been derived, which are related to the resistive and capacitive nature of the double layer, respectively.

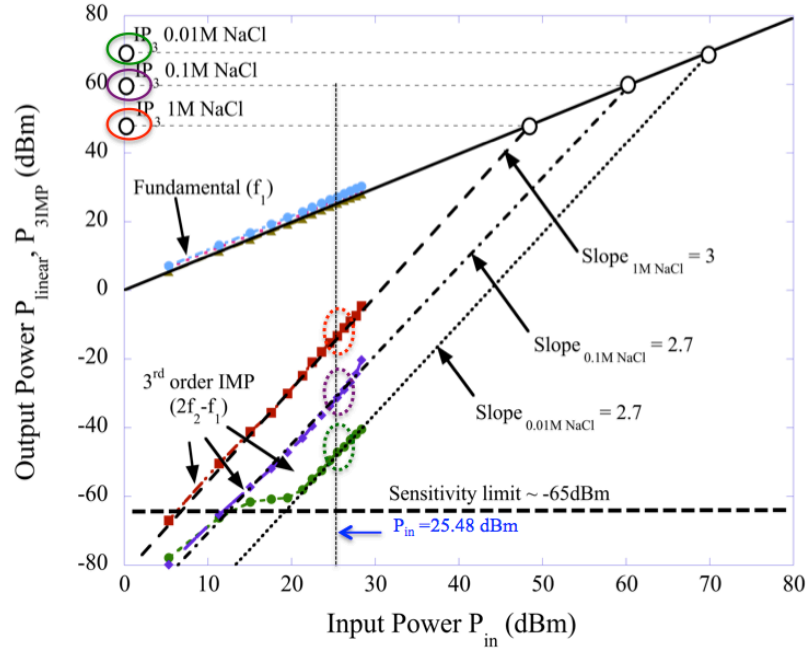


Figure 6-7 Output power for the fundamental and third order intermodulation product *versus* input power

The third-order coefficient of the Taylor's expansion of the resistive ionic current, which flows against the electrode and polarizes the sample between the two electrodes, was derived as Equation 6.7 and can be re-written as

$$a_{3cond} = \alpha^3 D e \left(\frac{A}{\epsilon h} \right) \cosh(\alpha \psi_s) n_{\infty}. \quad (6.14)$$

It can be seen that this coefficient is proportional to the ion concentration n_{∞} , or molarity M , defined as $M = n_{\infty} / 1000 N_A$. Here ψ_s is the surface potential, $\alpha = e / k_B T$, e is the electron charge, A and h are the area and distance between the electrodes, ϵ is the dielectric constant of the electrolyte, and D is the ionic diffusion coefficient in m^2/s units. The third-order coefficient of the capacitive current is derived in Equation 6.12 as

$$a_{3cap} = j \frac{\omega \alpha^3 A}{8} [2 \epsilon k_B T]^{1/2} \cosh\left(\frac{\alpha}{2} \psi_s\right) \sqrt{n_\infty}. \quad (6.15)$$

The capacitive component coefficient is proportional to the square root of ion concentration. Capacitive and conductive components of nonlinear mechanisms appear at the same electrode-electrolyte interface: one at the electrode surface and the other in the double layer side of the interface. It is equivalent to capacitors connected in parallel and they both experience the same electric potential v . As a result, the two response currents can be added and all the corresponding expansion coefficients of the two power series can be added as well, as shown in Equation 6.16. These two expressions allow us to use the following equation for fitting the experimental data

$$a_3(M) = aM + bM^{0.5}. \quad (6.16)$$

The nonlinear function of double layer conductivity has a factor proportional to the electrolyte concentration M (mol/L), and thus all coefficients of the power expansion of the nonlinear part of the function are also proportional to M , as shown in Equation 6.14. Likewise, the nonlinear capacitance of the double layer, where the nonlinear part of the function denotes the surface charge (whose variation with respect to potential is its capacitance), has a factor proportionate to the square root of concentration, $M^{1/2}$ as evident from Equation 6.15. Three equations were formed by substituting the three experimental points into Equation 6.16 and were solved for ‘a’ and ‘b’ using the least squares method. The obtained results are as follows: $a=1.910 \times 10^{-5}$, and $b=2.626 \times 10^{-6}$. Using Equation 6.16, a curve demonstrating these two parameters (Figure 6-8) is plotted. As evident, the curve is a perfect fit with the three experimental data points.

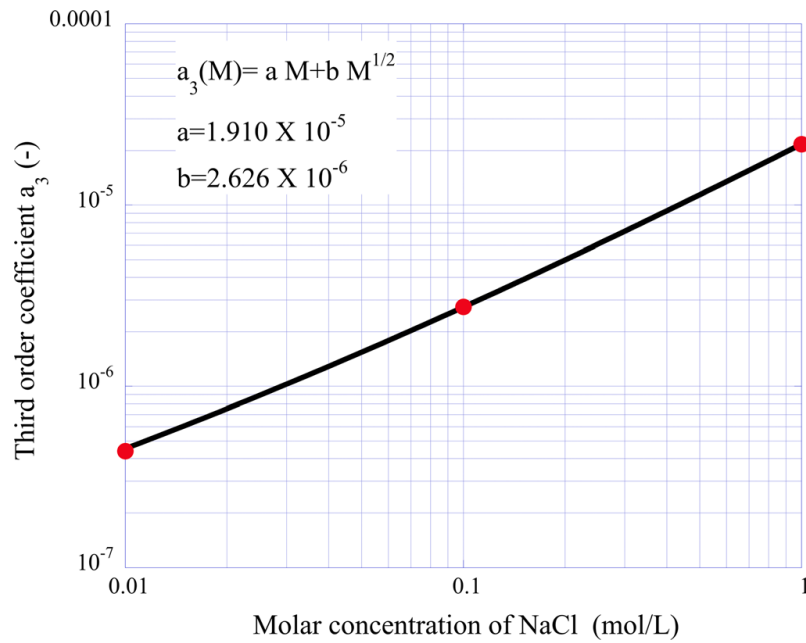


Figure 6-8 Plot of Equation 6.16 (black curve) and experimental data (red dots)

6.5.3 Electronic schematic capture analysis of the nonlinearity due to electrode - electrolyte interface

Geddes and DeBoer investigated the rectifying properties of the metal electrodes in contact with saline solutions and suggested to use back-to-back Zener diodes for representing electrolytic rectification [63]. The use of diodes hints on the nonlinear rectifying properties of the electrode-electrolyte interface. Hence, with the use of a spectrum analyzer component in Multisim, Figure 6-9 (a) was laid out and stimulated to see the nonlinear response. The value of sample resistance R_1 was approximately changed in order to simulate different molarities of NaCl. Figure 6-9 (b) shows the fundamental and third order intermodulation product peak for 0.01 M, 0.1 M and 1M NaCl solution as -91.835 dBm, -61.856 dBm and -50.927 dBm respectively for

an input power of approximately 8 dBm. The difference between the IMPs for ‘0.01 M & 0.1 M’ and ‘0.1 M & 1M’ is 30 dBm and 11 dBm respectively.

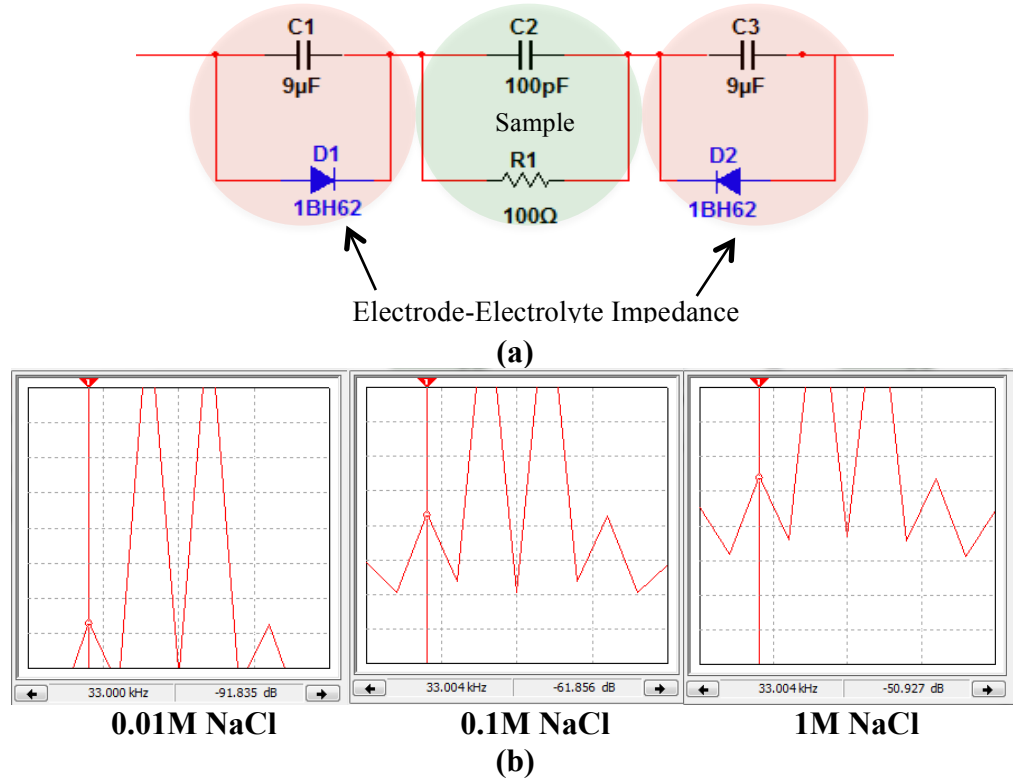


Figure 6-9 (a) Diode representation of non-linearity of the electrode-electrolyte interface (b) Intermodulation distortion peaks from the Multisim simulation of the diode circuit for 0.01M, 0.1 M and 1M NaCl solutions

From Figure 6-10, it is obvious that the trends follow the same order numbers but do not exactly match with the experimental values. Thus, it is confirmed that there is an unavoidable contribution of the non-linearity from the insulator-coated gold electrode-electrolyte interface to the observed nonlinearity in an aqueous electrolyte solution. This effect is intrinsic and interferes with the nonlinear signal from the bio-electrolytes and cells. Ascertaining the capacitive and conductive components of non-linearity from the electrolyte using this method, intermodulation distortion technique

could be used to distinguish the nonlinear signal of the biosample confined within an electrode arrangement.

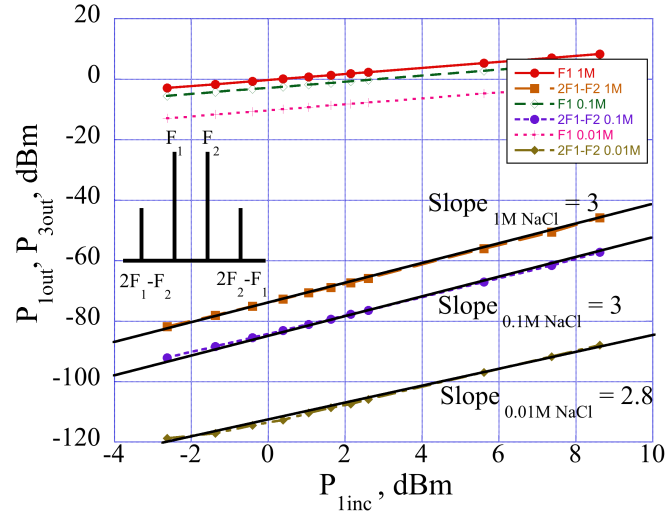


Figure 6-10 Output power for the fundamental and the third-order intermodulation product *versus* input power for 0.01 M, 0.1M and 1M NaCl aqueous solutions simulated from circuit level analysis

Chapter 7 *Rf* electromagnetic fields induced hyperthermia setup

7.1 INTRODUCTION

Noteworthy advances and novelties in the technology abetted by progressive computational tools have led to development and improvement of numerous ultrasound, microwave and RF devices for hyperthermia. In medical domains, these devices that emit energy are termed as applicators. Applicators are positioned around the organs or affected tissues and the energy is focused on the tumor to elevate its temperature.

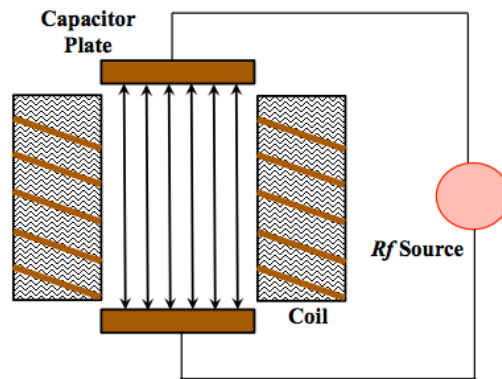


Figure 7-1 Capacitive and Inductive Heating System

The key idea behind a development of any setup for hyperthermia using *rf* approach is to either exploit alternating electric or magnetic fields. The applicators could be classified as capacitive heating or inductive heating applicators based on capacitive or inductive coupling respectively. The basic concept behind the capacitive and inductive heating mechanism (Figure 7-1) has already been discussed in section 2.5. Previous designs of systems and methods of hyperthermia included cascaded several LC-sections impedance matching network. Additionally multi-element array

applicators like a ring of radiating elements have been investigated to focus energy deposition and increase the value of deep tissue SAR with respect to surface SAR.

7.2 BLOCK DIAGRAM OF HYPERTHERMIA SETUP

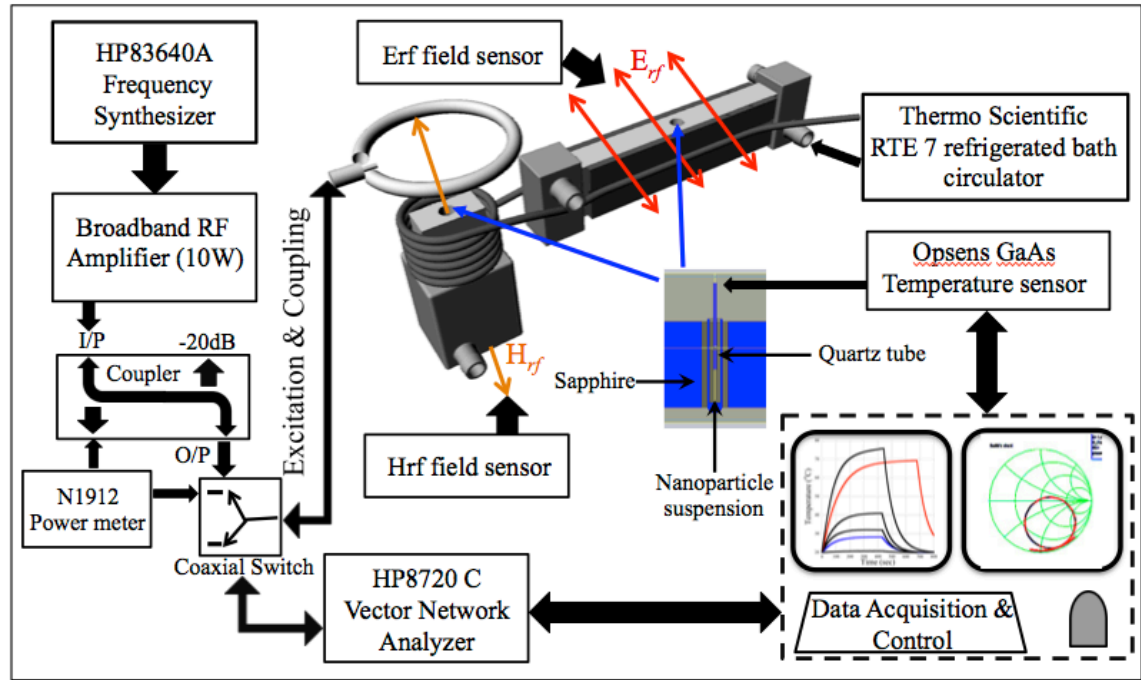


Figure 7-2 Schematic representation of hyperthermia setup

7.3 LCR RESONATOR

The quasi-static approach of an LCR (Inductance Capacitance Resistance) resonant circuit is utilized to realize the set up for hyperthermia because of its low input power requirement. A circuit is said to be in resonance when the average stored magnetic and electric energies in the inductive and the capacitive elements in the circuit are equal. The basic operational circuit for a resonance is shown in Figure 7-3. Two important parameters that describe a resonant circuit are resonant frequency (f_r) and quality factor (Q). The frequency at which resonance occurs is termed as resonant

frequency and is defined as $f_r = 1/2\pi\sqrt{LC}$. The quality factor (Q) is another important characteristic of the resonant circuit and is the measure of loss of the resonant circuit and is defined as the product of the angular frequency ω and the ratio of the energy stored in the circuit to the energy loss per second. Higher Q value refers to lower loss. At resonance, quality factor can be expressed as, $Q = (2\pi f_r L)/R = 1/(2\pi f_r RC)$. Thus Q increases with reduction in resistance of the resonant circuit.

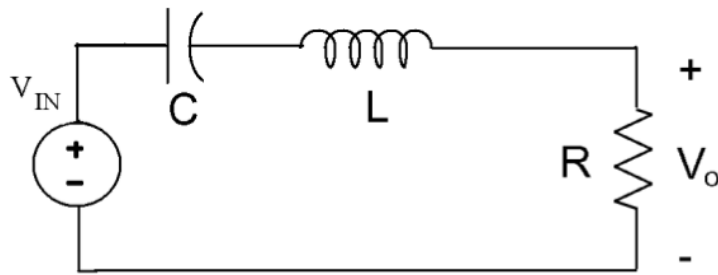


Figure 7-3 A series LCR resonator circuit

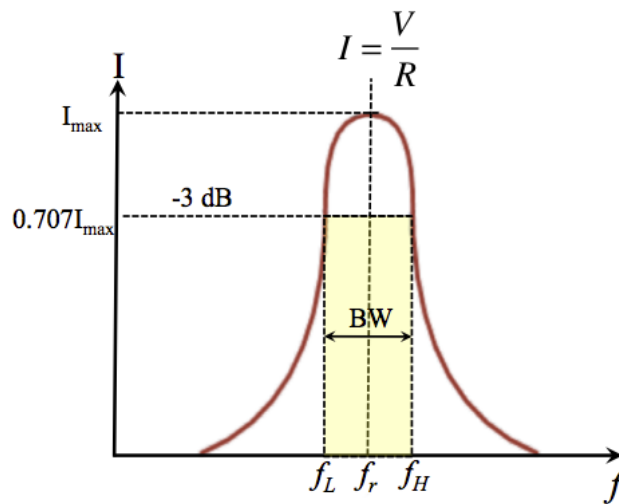


Figure 7-4 Response of a series LCR resonant circuit with its current response

Figure 7-4 shows the current response of the series LCR resonance circuit. At resonance, the input impedance is minimum and the current is at its peak.

7.3.1 Design

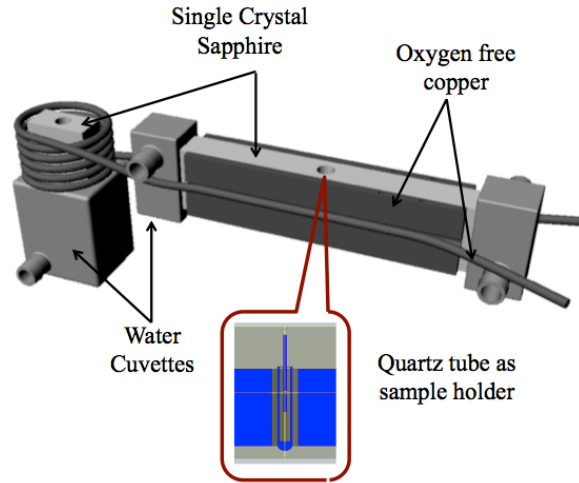


Figure 7-5 LCR resonator made up of oxygen free copper metal to realize the capacitive plates and the inductive coils; the sample is placed in a quartz tube mounted in cavities drilled in sapphire

High Quality factor (~ 500) LCR resonator provides adequate rf amplification thereby dissipating rf energy principally in the resonant circuit and not in the whole system, thus rationalizing the problems of stabilization of cooling temperatures. To achieve a high quality factor (Q), we have used oxygen-free copper metal to realize the capacitive plates and the inductive coils. The capacitor in the LCR resonator is constructed with two water-cooled copper plates separated by a single crystal 12 mm thick sapphire ($\epsilon_r = 11$, $\tan\delta = 0.001$). The resonator solenoid is made of six turns of 3 mm outer diameter copper tube wound into a coil of diameter 40 mm and length 21 mm and distance per turn of 0.1 mm. An additional piece of single crystal sapphire is placed inside the solenoid. Both of the sapphire crystals are water cooled and thus used as sink

owing to its excellent thermal conductive properties. The resonator is designed in a way such that the sample of about 150 μL is placed in a quartz tube of inner and outer diameter of 2.5 mm and 3 mm mounted in cylindrical cavities drilled in the sapphire crystals of the capacitor and solenoid as shown in the Figure 7-5. Precisely machined out Teflon plugs are used to hold the quartz tube perfectly symmetrical in the cylindrical cavity. This would maintain the thermal equilibrium around the quartz tube by keeping it vertical. If the tube were inclined in the sapphire cavity, the sample would be exposed to non-uniform field lines, due to which a temperature gradient or thermal imbalance might be created. Low loss tangent of Teflon also does not allow any heat dissipation on plugs, thus preventing any additional heat sources.

7.3.2 Coupling and RF excitation

To obtain maximum power transfer between our RLC resonator and the feedline, the resonator has to be matched to feed at the resonant frequency. To determine the resonant frequency, a network analyzer HP8174 is used (Figure7-6). The analyzer is controlled by a Labview program, which takes into account the feedline calibration, and gives information about the resonant frequency, coupling and the quality factor. The coefficient of coupling is ensured to be one, so that the resonator is critically coupled to the feedline and the input and output impedance are matched to 50Ω . We have followed the principles of cavity perturbation while exposing the samples to be analyzed, to alternating electric or magnetic fields in our resonator. The actual fields of the cavity with such small perturbations are not very different than the unperturbed cavity. For such each entry of sample into the resonant cavity, the shift in

resonant frequency is noted. Once the resonant frequency is determined, the frequency sweeper HP83640A is used to excite the resonant circuit as shown in Figure 7-7.

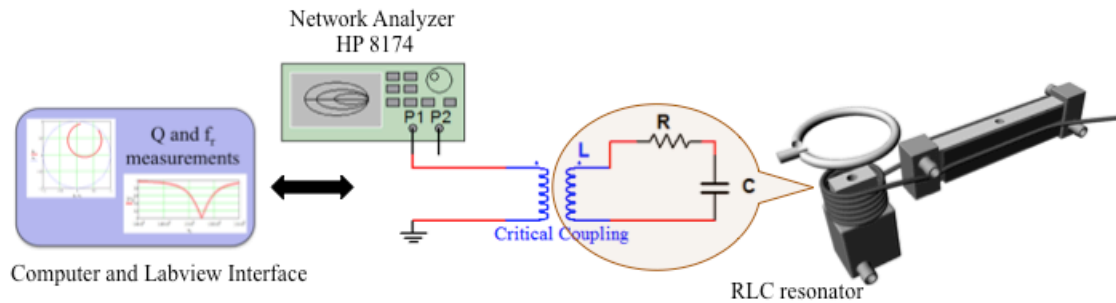


Figure 7-6 Coupling and Q and f_r measurements using a network analyzer and LabView Interface.

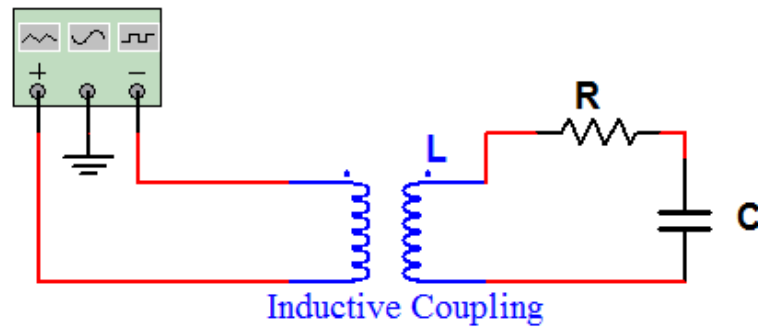


Figure 7-7 Driving input power to the critically coupled resonator using frequency sweeper coupled with amplifier

7.4 TEMPERATURE SENSING AND HEAT SINK

In a strong EM field environment, we preferred to use a non-inductive optical fiber temperature sensor. The sensor is based on the temperature dependence of the band-gap of GaAs semiconductor crystal, which is bonded to the tip of an optical fiber. A signal conditioner is used to send light to the GaAs crystal *via* the optical fiber. The GaAs crystal absorbs wavelengths of light below the band-gap spectral position and reflects the wavelength above the band-gap. The band-gap spectral position is

calculated from the light spectral intensity distribution of the reflected light and is calibrated to the absolute temperature. This temperature sensor is immersed in the quartz tube filled with the sample and is aligned to be at the center of the tube, so that uniform temperature sensing is ensured as shown in Figure 7-8. The temperature and band gap dependence is governed by

$$E_g(T) = E_g(0) - \frac{\alpha T^2}{T + \beta}, \quad (7.1)$$

where typical values for $E_g(0)$, α , β are 1.519 eV, 5.41×10^{-4} eV/K and 204 K respectively.

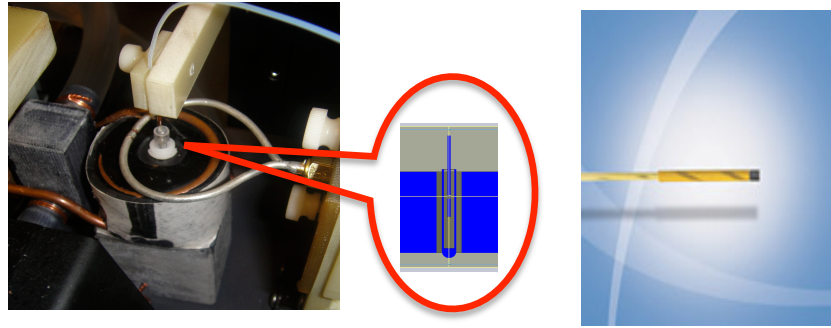


Figure 7-8 Ga-As monocrystal based optical fiber temperature sensor

A refrigerated bath circulator from Thermo Scientific is used to allow a constant sink temperature of about 20°C. Flowing water through the copper plates and the copper coil allows their cooling. The two ends of sapphire are also cooled using pockets/cuvettes allowing flow of water, attached to them. This cuts out the heating of the test-sample by the system components itself, thereby maintaining uniform temperature all over the setup and thus negating a huge error component. Sapphire being a good thermal conductor takes the heat away from the sample. This helps to achieve the saturation temperature. However, for specific absorption rate analysis, only

the first few seconds from the temperature *versus* time curve are taken into consideration.

7.5 FIELDS IN THE RESONATOR AND POWER MEASUREMENTS

7.5.1 Theoretical electric and magnetic fields

The electric field induced across the capacitor depends on input power and the coupling coefficient between the resonator and the exciting loop is

$$V_c \propto MP_{in}^{1/2}. \quad (7.2)$$

Here V_c is the voltage induced across the plates of the capacitor of the resonator, P_{in} is the input power, and M is the coupling coefficient or the mutual inductance between the solenoid of the resonator and the exciting loop. The magnetic fields are oriented along the z-axis and are perpendicular to the plane of the coil. The intensity H_z is proportional to the input current induced in the solenoid, which is a function of input power and can thus be represented as

$$H_z \propto I_c(P_{in}). \quad (7.3)$$

Figure 7-9 shows the simulated electric fields and magnetic fields *versus* input power for such a resonator setup. With an increase in input power, higher would be the current induced into the solenoid coil and thus larger will be the voltage across the capacitor, resulting in a higher electric field generated between the plates. The voltage induced V_c and thus the electric field E across the capacitor has a square root dependence with the input power. Magnetic field H is dependent on the resonator current, which is a function of input power and thus has a squared root dependence on input.

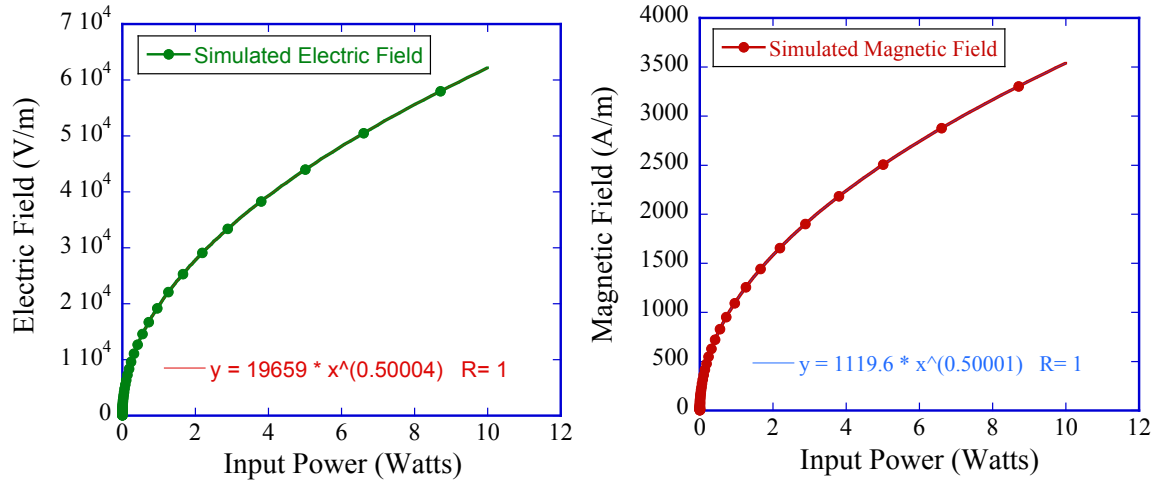


Figure 7-9 Simulated electric and magnetic fields *versus* input power

7.5.2 Experimental techniques to measure fields

Electric field and magnetic field in the capacitive and inductive cavities of the resonator are measured using Agilent Oscilloscope. For electric field measurements, the voltage on the capacitor plates is indirectly measured, from which the value of the fields can be calculated. Such voltage measurements are realized by connecting a limiting capacitor of 1 pF to the measuring probes of the oscilloscope. The limiting capacitor along with the probe capacitor forms a capacitive divider arrangement as shown in Figure 7-10.

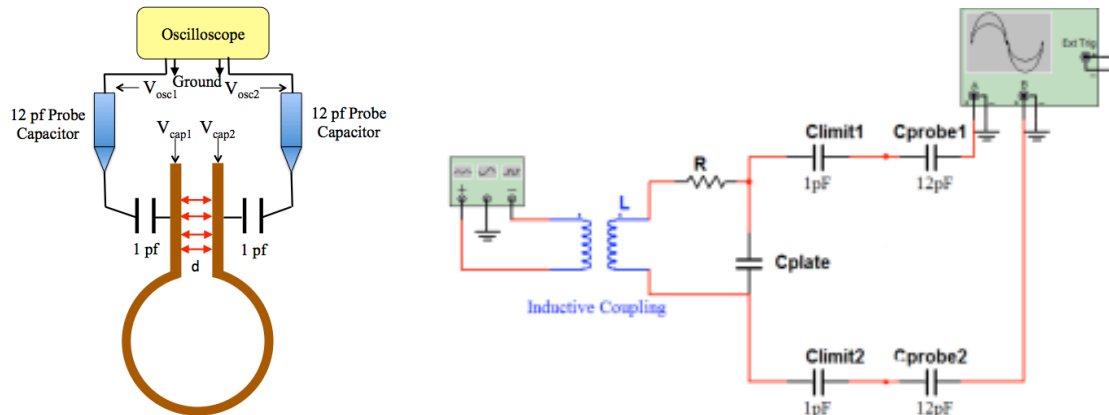


Figure 7-10 Circuit to measure electric field between the capacitor plates.

The voltages measured with oscilloscope are substituted in the Equation 7.4, which gives

$$V_{cap} = V_{osc} \left(\frac{C_{probe} + C_{lim}}{C_{lim}} \right). \quad (7.4)$$

Thus, the electric field between the plates of the capacitor is defined as

$$E_d = \left(\frac{V_{cap1} - V_{cap2}}{d} \right) = \frac{\Delta V_{cap}}{d}. \quad (7.5)$$

To measure the time varying H-field produced by the inductive field coil of the resonator, we used a small loop called a ‘search coil’ and placed it in the center where the sample is put for H-field exposure. The Figure 7-11 represents the search coil arrangement to measure the magnetic field of the inductive field coil.

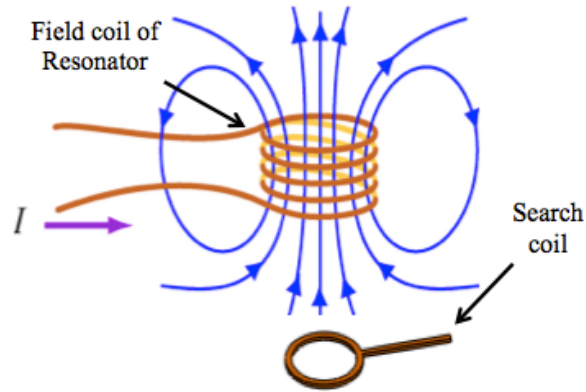


Figure 7-11 Measurement of magnetic field using search coil

The voltage induced in the search coil is measured on the oscilloscope and can be related to magnetic field present due to field coil B as

$$B_{pp} = V_{pp} / \omega NA, \quad (7.6)$$

$$H_{pp} = B_{pp} / \mu, \quad (7.7)$$

where ω is the resonant frequency, N is the number of loops in the search coil and A is the area of search coil. For the field coil present in the air and the radius of search coil 'a', the equation for a peak magnetic field H_p can be rewritten as

$$H_p (A/m) = \frac{V_p}{8\pi^3 f N a^2} \times 10^7. \quad (7.8)$$

7.5.3 Experimental fields' dependence on measured input power

The power input from the frequency synthesizer was coupled through an amplifier. So the input power fed to the resonator (output from amplifier) with respect to input power from the frequency synthesizer has been plotted in Figure 7-12.

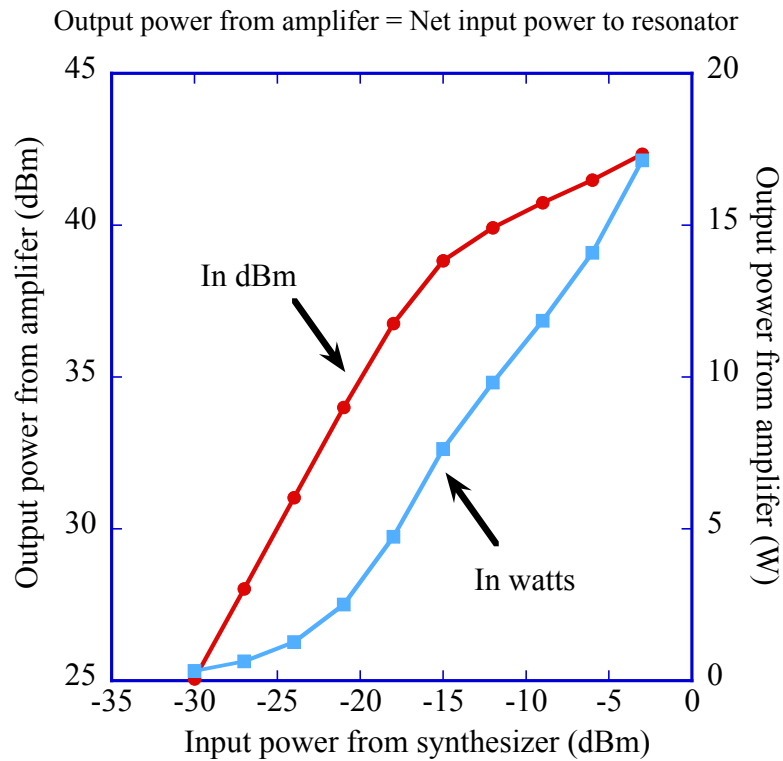


Figure 7-12 Input power fed to the resonator (output from amplifier) with respect to input power from the frequency synthesizer

The power measurements were done using an Agilent N1912A power sensor. The electric field between the capacitor's plates (with spacing $d = 12.75\text{mm}$) and magnetic fields inside the solenoid coil with (number of turns $N=5$) at 30 MHz measured experimentally using the techniques mentioned in Section 7.5.2 are tabulated as follows in Table 7.1 and 7.2.

Table 7.1 Calculation of electric field between the plates of the capacitor

Input power (dBm)	Input power (W)	ΔV_{osc} (V)	$E_p = \frac{\Delta V_{cap}}{d} = \frac{13}{2} \frac{\Delta V_{osc}}{d}$ (kV/m)
-30	0.3206	20	10.196
-27	0.6353	28.1	14.325
-24	1.2676	40	20.392
-21	2.5119	56.3	28.702
-18	4.7424	78.7	40.121
-15	7.6384	98.1	50.011
-12	9.8175	110	56.078
-9	11.8577	119	60.666
-6	14.0929	131.3	66.937
-3	17.1396	145	73.921

Table 7.2 Calculation of magnetic field within the solenoid

Input power (dBm)	Input power (W)	V_{rms} (V)	$H_p = \frac{V_{rms} \sqrt{2}}{8\pi^3 f a^2} \times 10^7$ (A/m)
-30	0.3206	1.29	932.2
-27	0.6353	1.83	1322.5
-24	1.2676	2.58	1864.45
-21	2.5119	3.6	2601.9
-18	4.7424	4.96	3584.35
-15	7.6384	6.32	4567.1
-12	9.8175	7.1	5130.8
-9	11.8577	7.71	5571.6
-6	14.0929	8.42	6084.7
-3	17.1396	9.38	6778.5

Figure 7-13 (a) and (b) shows the plots of calculated electric and magnetic fields from Table 7.1 and 7.2 *versus* input power with a square root dependence of fields on power.

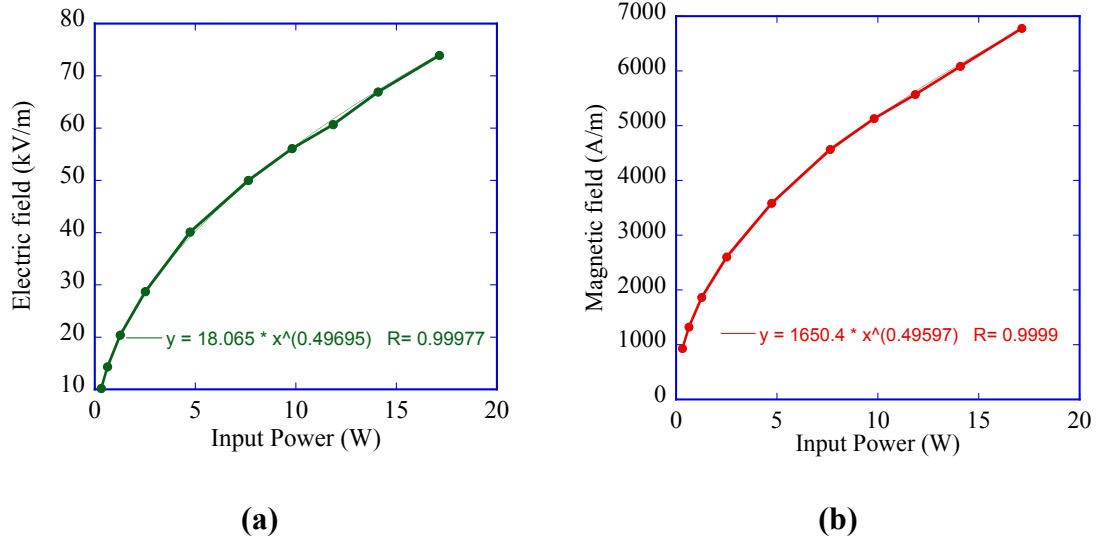


Figure 7-13 Square root dependence of (a) electric field between the capacitor plates (b) magnetic field within the solenoid *versus* input power

7.5.4 Heating of superparamagnetic iron oxide nanoparticles with varying input power placed in capacitor and solenoid

A preliminary study to test the heat response from the experimental setup as a function of input power was done by heating a colloidal suspension of iron oxide nanoparticles. As per definition, they are expected to exhibit both electric field and magnetic field induced losses. The stock solution of 5 nm superparamagnetic iron oxide nanoparticle suspensions of 5mg/mL concentration from Sigma Aldrich was diluted 64-fold to reduce the concentration and then exposed to alternating electric and magnetic fields at 29 MHz. The dilution was important as otherwise at higher fields very high heating rates resulting in boiling are observed. This would cause instability in the system and would make the field dependence study challenging. The input power from the sweeper was gradually increased, resulting in corresponding increments in electric

and magnetic fields. For each increment, the heating was recorded and the trend was studied as shown in Figure 7-14.

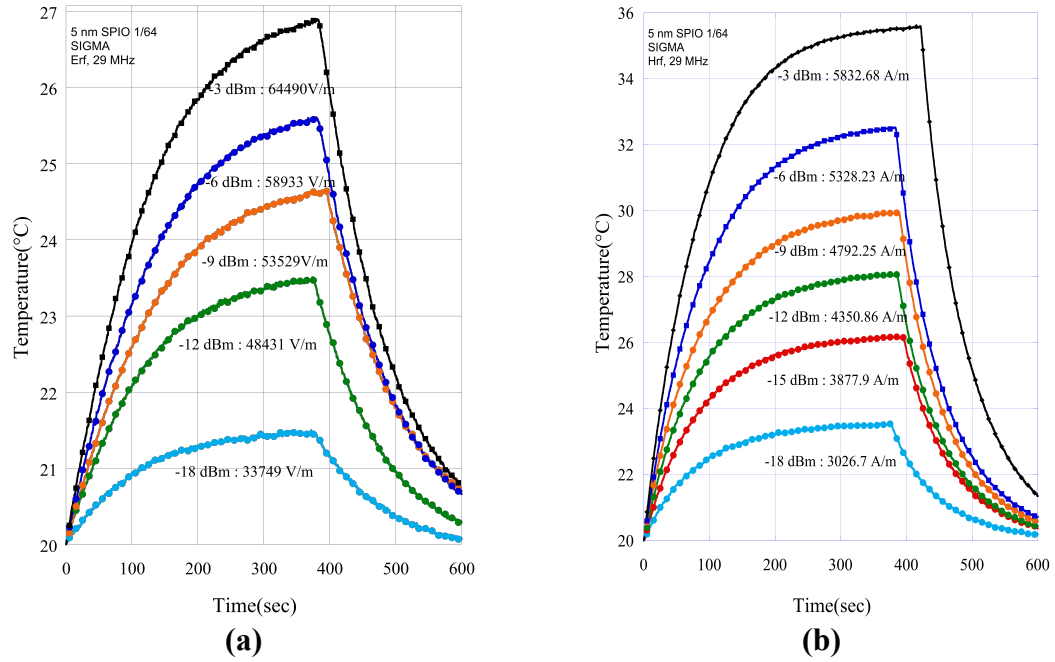


Figure 7-14 Heating curves for iron oxide nanoparticles in (a) electric and (b) magnetic fields

A squared dependence of heating rate on field strength is observed from the slopes as shown in the Figure 7-15 for initial heating for the first 20 seconds.

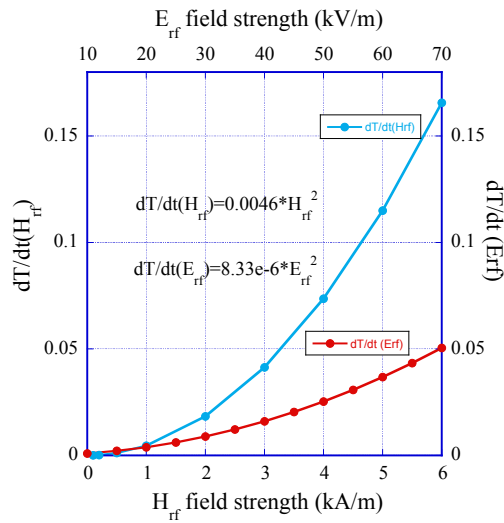


Figure 7-15 Heating slopes of SPIO in E and H fields *versus* the field strengths

Chapter 8 Results: Hyperthermia

8.1 CAPACITIVELY-COUPLED FIELD HEATING

The preliminary analysis of metallic nanoparticle's heating from a capacitively-coupled electric field's interaction is studied by placing the particles in the capacitor of the hyperthermia setup. Since, all nanoparticle samples employed in the study are suspended in a water-based dispersion media, DI water is always characterized for reference.

8.1.1 Electric field heating of gold nanoparticles with varying concentrations

Temperature rise is measured as a function of time with onset of power for a suspension of 5 nm gold nanoparticles obtained from Ted Pella Inc. in a water-based medium. The sample is placed in a quartz tube between the two plates of the capacitor at 150 MHz at 10 W of input power. This input power corresponds to 1000 V across the capacitance plates and matches to an electric field strength E of about 1.5×10^5 V/m. Concentration of gold nanoparticles was 5×10^{13} particles per mL which results in a volume fraction of 3.27×10^{-6} for 5 nm particle size. Further dilutions of two-fold and four-fold were done to study the change in concentration of gold in the nanoparticle suspension as shown in Figure 8-1. These heating trends were fit with a fitting model, in which rise in temperature was accounted from two sources; one from the water based nanoparticle sample and other from the quartz tube. The heating of the medium (water) was also considered and subtracted from the heating of the suspension itself to obtain the net contribution of heat exclusively from the particles. As mentioned in the section 7.3, the nanoparticle samples are placed in a quartz tube with a very small loss tangent.

The contribution to heat loss is ignored for the first few seconds when the heating just starts and is in a very linear regime. Therefore, the slope $\Delta T/\Delta t$ of this linear regime of the temperature *versus* time curve is used to analyze the heat absorption rate of the sample.

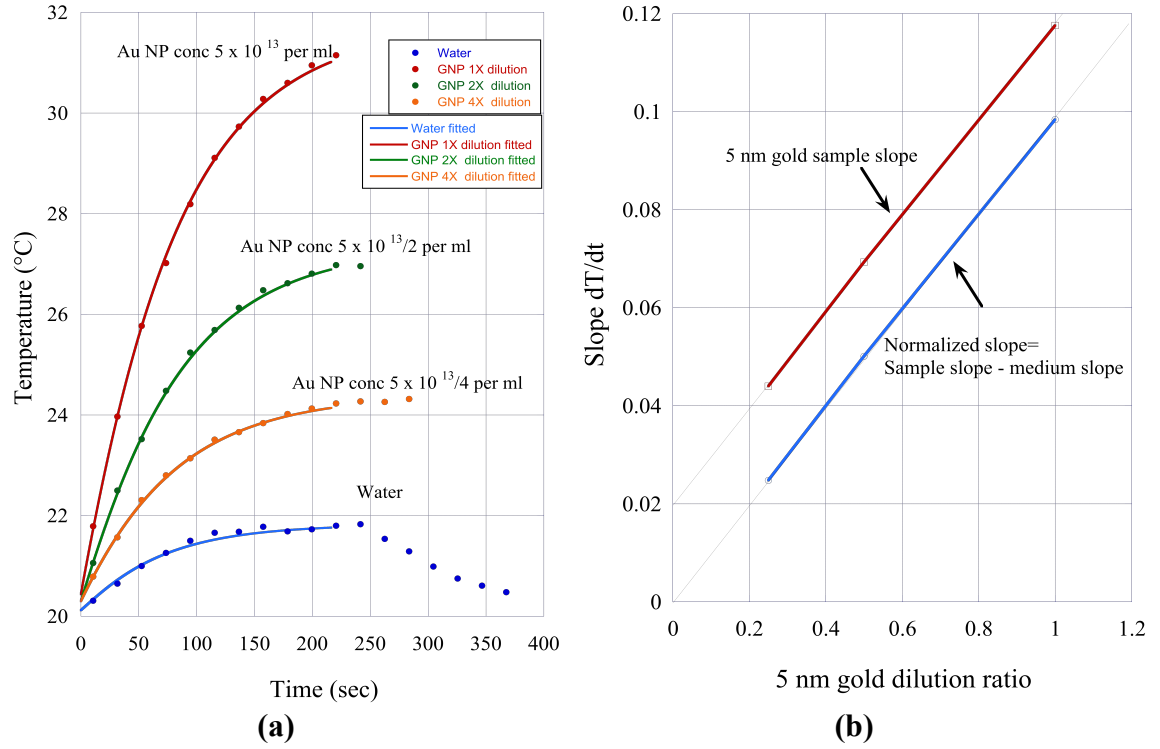


Figure 8-1 (a) Temperature *versus* time curves for gold nanoparticle and the two and four fold dilutions (b) Normalized slopes *versus* dilution ratio

A set of equations based on calorimetry and electromagnetics is derived to analyze the electromagnetic fields induced calorimetry of the nanoparticle samples. Heat loss per unit volume of the sample P (W/m^3) can be thermodynamically expressed in terms of slope $q = \Delta T/\Delta t$ as

$$P = C_{ps} \rho_s q, \quad (8.1)$$

where C_{ps} is the constant pressure specific heat capacity of the sample ($\text{J}/\text{kg}^\circ\text{C}$) and ρ_s is the sample's mass density (kg/m^3). As defined before, the specific absorption rate

(SAR) is the power absorbed per unit volume of the sample and is calculated as P/ρ_s . It can also be calorimetrically expressed as $C_{ps} \Delta T/\Delta t$ (W/kg). For aqueous solution based suspensions, values of C_{ps} and ρ_s are taken to be those of water as 4.18×10^3 J/kg°C and 10^3 kg/m³. When a material is exposed to an alternating electric field E , the power loss per unit volume can be expressed as

$$P = \frac{1}{2} \sigma |E|^2 = \frac{1}{2} \epsilon_0 \epsilon'' \omega |E|^2, \quad (8.2)$$

where the material is assumed to be a lossy dielectric with electrical conductivity of the material σ , the imaginary component of dielectric constant ϵ'' and ω is the angular frequency of the alternating electric field. It is always considered that a sample of nanoparticle suspension with total volume V_T consists of the nanoparticles' volume V_{NP} and the dispersion medium (solution) with volume V_S and in case of dilution of the suspension, the volume V_W of DI water added keeping the total volume V_T constant. The conceptual realization is shown in Figure 8-2. In such a case, calorimetrically the heat equation is written as

$$C_{ps} \rho_s q V_T = P_{NP} V_{NP} + P_S V_S + P_W V_W, \quad (8.3)$$

where P_{NP} , P_S and P_W are the power loss per unit volume from the nanoparticle, dispersion solution and DI water added, respectively.

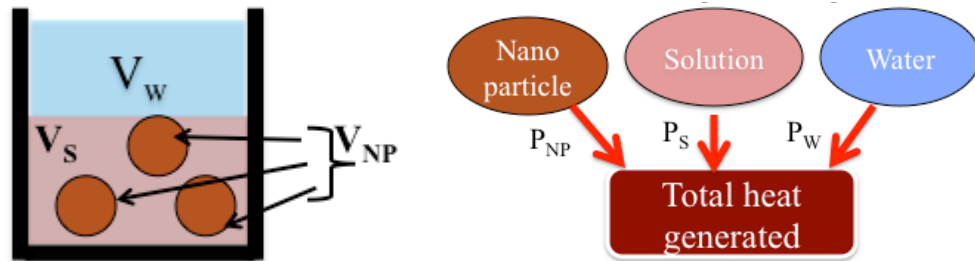


Figure 8-2 Calorimetric components of heat from nanoparticle suspension

For such analysis, volume fraction of nanoparticles and dilution rate are defined as $V_f = V_{NP}/(V_{NP} + V_S)$ and $x = (V_{NP} + V_S)/V_T$ respectively. Hence in terms of V_f and x , Equation 8.3 can be written as

$$C_{ps}\rho_s q = \left[P_{NP}V_f + P_S(1 - V_f) \right] x + P_W(1 - x). \quad (8.4)$$

Before calculating the rf loss of particle, it is significant to contribute the heating loss of the dispersion medium (solution), itself in the electric field. In the preliminary measurements of gold nanoparticles, it is assumed that gold nanoparticles are suspended in water. Hence DI water is referenced as the suspending medium and the heating slope of DI water is taken into account as a control test solution for analysis. Thus, solving Equations 8.2 and 8.4 for water as a medium, the following equations can be derived;

$$C_{ps}\rho_s q_{sol}^c = \frac{1}{2} \sigma_{sol}^c |E|^2, \quad (8.5)$$

and

$$\sigma_{sol}^c = \frac{2C_{ps}\rho_s q_{sol}^c}{|E|^2}. \quad (8.6)$$

Here q_{sol}^c and σ_{sol}^c are the slope of heating and conductivity of dispersion solution when placed in a capacitor, which is DI water in the present case. Furthermore, the local electric field E at the sample is βE_y with β as the dielectric polarization-screening factor, which is assumed to be 0.11 owing to experimental design, and E_y is the electric field between the two metal plates of the capacitor. In a similar fashion like Equations 8.5 and 8.6, the conductivity for a nanoparticle suspension kept in the capacitor, can be derived as

$$\sigma_{NP}^c = \frac{1}{xV_f} \left[\frac{2C_{ps}\rho_s q_{sus}^c}{|E|^2} - \sigma_w^c (1-x) \right] - \sigma_{sol}^c \frac{1-V_f}{V_f}. \quad (8.7)$$

If there is a no dilution using DI water (x=1), Equation 8.7 reduces to

$$\sigma_{NP}^c = \frac{1}{V_f} \left[\frac{2C_{ps}\rho_s q_{sus}^c}{|E|^2} - \sigma_{sol}^c (1-V_f) \right]. \quad (8.8)$$

Thus, SAR [W/kg] for nanoparticle at a certain frequency ω and a local electric field E can be defined as

$$SAR_E = \frac{\sigma_{NP}^c}{2\rho_{NP}} |E|^2 = \frac{\sigma_{NP}^c}{2\rho_{NP}} |\beta E_y|^2, \quad (8.9)$$

where ρ_{NP} is the mass density of the nanoparticle. Using the slopes from Figure 8-1 and assuming the nanoparticles to be suspended in water and then water itself is used for dilution, the effective conductivity and SAR for the water gold nanoparticles are tabulated in Tables 8.1 and 8.2 respectively.

Table 8.1 SAR and conductivity of DI water

Slope of water	βE_y (kV/m)	Cond. of DI Water (S/m)	SAR of DI Water(W/kg)
0.024	16.500	0.00074	100.73

Table 8.2 SAR and conductivity calculations of gold nanoparticle's stock suspension and relative dilutions

Dilution ratio (x)	Volume Fraction	Slopes (q)	Cond. of Gold NP (S/m)	SAR of NP (W/kg)
1	3.27×10^{-6}	0.147	1156.42	8.16×10^6
0.5	3.27×10^{-6}	0.087	1184.09	8.35×10^6
0.25	3.27×10^{-6}	0.055	1164.18	8.21×10^6

8.1.2 Electric field heating of porous silicon shells loaded with gold nanoparticles

A conceptual design of silicon-gold nanoconstructs with drug loading capability and functionalization by attaching cancer cell targeting moieties to make them tumor specific is shown in Figure 8-3. The rationale behind fabrication of such nanoconstructs is the combination of chemo and thermo modalities. Gold nanoparticles encapsulated in silicon porous shells were heated in electric fields at 57 MHz.

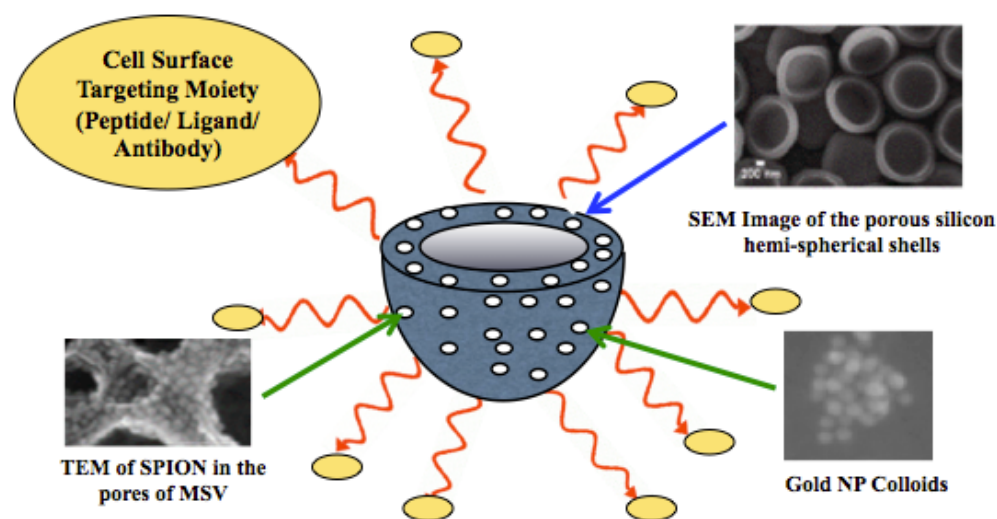


Figure 8-3 Conceptual design of silicon gold nanoconstructs

Figure 8-4 shows the comparison of heating trends of nanoparticles in silicon shells with heating of control solution. The control solution contains the same concentration of Au nanoparticles and is prepared by the same protocol by which the gold particles were encapsulated inside the shells. A comparison with gold stock solution is also done. It is assumed that the concentration of gold nanoparticle is reduced in the process of encapsulation; hence the volume fraction of the particles encapsulated is less than the volume fraction of the stock solution.

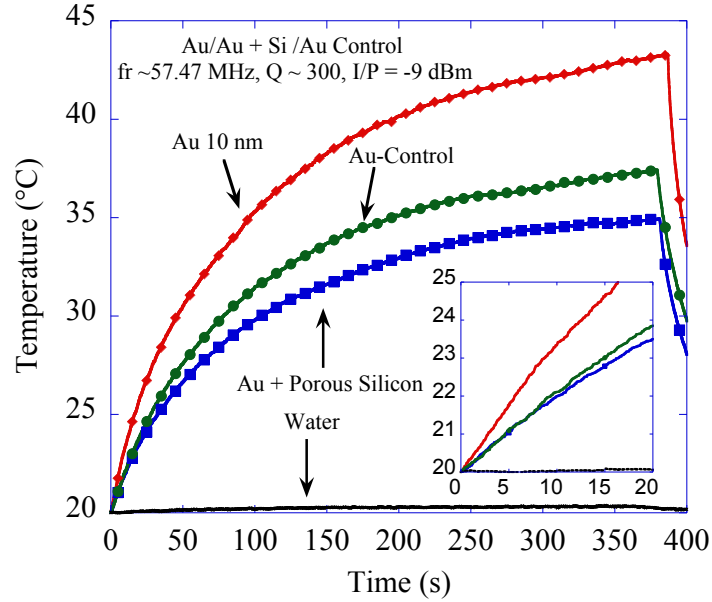


Figure 8-4 Electric field heating of Au nanoparticles and Si hemispheres loaded with Au

From the temperature *versus* time plot, it is evident that the nanoconstructs and the control nanoparticle solutions, heat to the same level for the first 20 seconds, but later on the trend deviates from each other. The different saturation temperatures observed could be accounted to the change in heat conductivity of the samples due to the encapsulation of the gold nanoparticles into silicon.

8.2 CAPACITIVELY AND INDUCTIVELY COUPLED FIELD HEATING

The *rf* hyperthermia system was designed to analyze both magnetic and non-magnetic types of nanoconstructs, however in the last section, the temperature *versus* time curves for only non-magnetic nanoparticles placed in the capacitor of the resonator were done. In the following sections, heating of the samples would be analyzed by placing them in a solenoid as well.

8.2.1 Magnetic field and electric field heating of deionized water

With an objective to assess magnetic losses in a solenoid, we started with DI water to test as a basic control solution in both the solenoid and capacitor at 30MHz and the thermographic data for DI water is recorded in Figure 8-5.

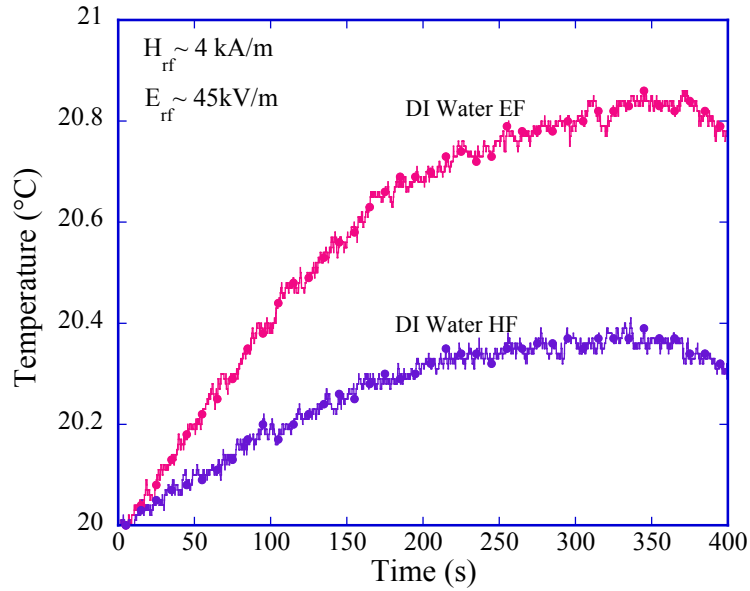


Figure 8-5 Temperature *versus* time curves for DI water when placed in a solenoid and capacitor

The losses in capacitively coupled fields are higher than inductively coupled fields, which could be attributed to the fact that the polarization losses in the capacitor for water molecules are higher than the eddy current losses in the solenoid. The slopes for heating of the water in the inductor and capacitor are recorded to be 0.002 and 0.004 respectively.

8.2.2 Effect of conductivity on magnetic field and electric field heating

Five nm gold nanoparticles were placed in the solenoid and capacitor at 30 MHz as shown in Figure 8-6. Surprisingly, gold nanoparticles are heated quite high in the

solenoid in comparison to those placed in the capacitor. One cannot expect that the significant change in the heating can be attributed to eddy current loss as ohmic heating is negligible [91] and theoretically the gold nanoparticle has no magnetic susceptibility. Hence, some new experiments are deliberated to change the conductivity of DI water. The simplest approach to change the conductivity of DI water is to add a calculated amount of sodium chloride (NaCl).

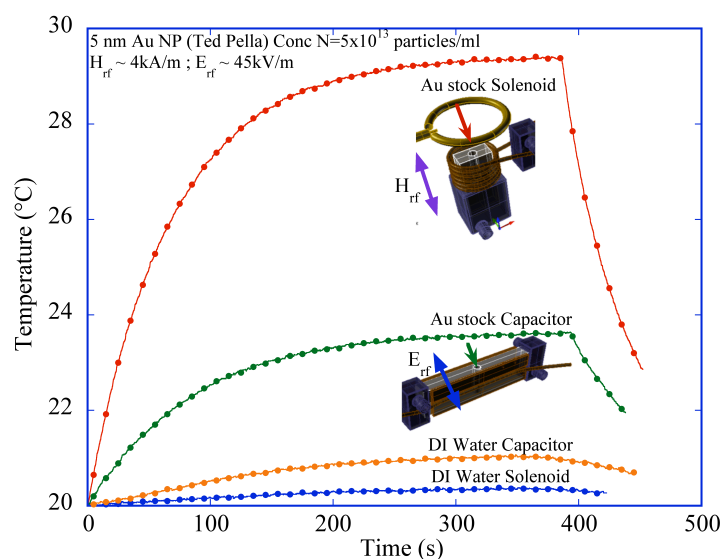


Figure 8-6 Temperature *versus* time curves for 5nm gold particles and DI water as a control, when placed in the solenoid and the capacitor

Table 8.3 Molar concentration of aqueous NaCl solutions and their dc conductivity shows the concentration of NaCl solutions and their calculated dc conductivity employed for the heating analysis.

Table 8.3 Molar concentration of aqueous NaCl solutions and their dc conductivity

Molar Conc. (mM)	1.25	2.5	5	10	30	60	100	150	200	300
DC Cond. (S/m)	0.1575	0.315	0.063	0.126	0.378	0.756	1.26	1.89	2.52	3.78

Figure 8-7 (a) displays that 2.5 mM NaCl solution shows the similar behavior as observed in the case of the gold nanoparticle's suspension. Several solutions of different NaCl concentrations including a concentration of physiological saline solution were also analyzed. Instead of expected linear increase in the heating slope of solutions with respect to salt concentration, the trend of heating slopes observed is very non-linear. However, such trends of nonlinear effects of NaCl concentrations on conductivity and *rf* ablation have been already reported by Goldberg where hyperthermia was induced into porcine tissues by injecting saline solutions [10].

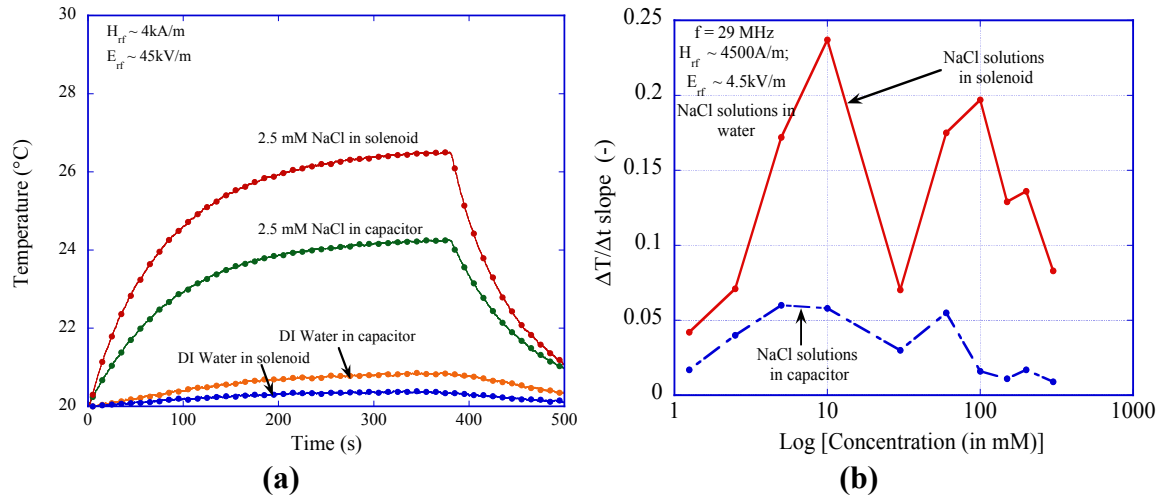


Figure 8-7 (a) Effect of conductivity change on heating of DI Water by making 2.5mM NaCl solution (b) Heating slopes of NaCl in electric and magnetic fields *versus* the salt concentration

Although Figure 8-7 (b), shows a very nonlinear heating slope *versus* concentration, yet for analysis only the first few points up to 5mM are taken into account as shown in Figure 8-8. This regime of the slope *versus* concentration is relatively linear. To simply analyze a test sample per se, a random tap water sample on one day was taken and heated and then based on the slopes of the tap water in the

solenoid and capacitor, the molar concentration of salt equivalence for the conductivity of tap water was calculated.

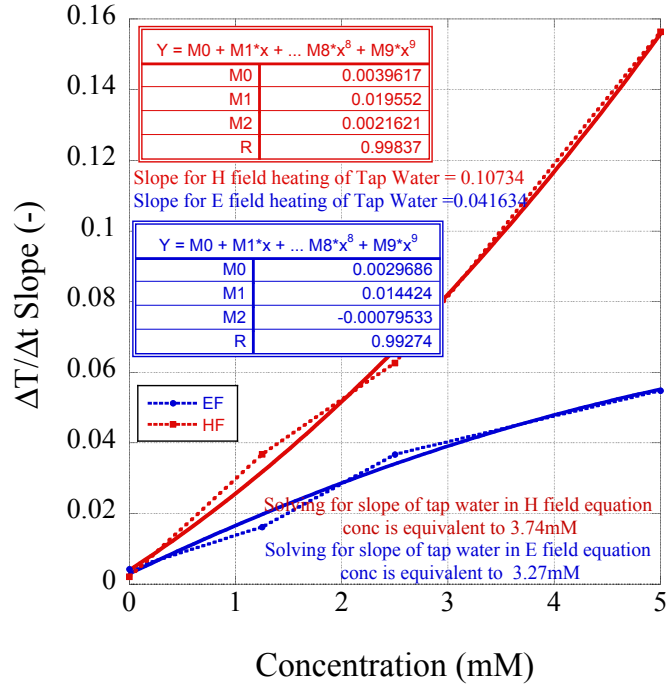


Figure 8-8 Slopes of $\Delta T/\Delta t$ from heating 1.25mM, 2.5mM and 5mM NaCl solutions in solenoid and capacitor

Accounting for such losses to hysteresis will not be an adequate reason behind supporting the notion of heating conductive samples in a magnetic field. To address this, we expanded a concept about the presence of electric fields within the solenoid [108], which could account for the loss due to conductive suspensions in alternating electromagnetic fields. This notion is elaborated more in the following section.

8.3 PRESENCE OF CONSERVATIVE AND MAGNETICALLY INDUCED FIELDS IN THE SOLENOID OF THE RESONATOR

Considering the cylindrical coordinate system, the solenoid produces an alternating *rf* magnetic field H_z in the axial *z*-direction. According to Faraday's law of

induction, this magnetic field H_z creates an alternating electric field referred to as the magnetically induced electric field E_ϕ , oriented in the circumferential ϕ -direction. Furthermore, an axial electric field E_z also subsists due to the scalar electric potential of the coil winding [109]. E_ϕ is accountable for eddy current losses while H_z is responsible for spin related losses. Usually, in most solenoid configurations, the E_z component is at the least of the equivalent order of E_ϕ magnitude, and notably contributes to the total rf electric field $E_s = E_\phi + E_z$, thereby affecting the sample heating [108]. This heating due to interaction of E_z with both nanoparticles and the suspending solution, if ignored may lead to an erroneous calorimetric analysis and subsequently an overestimation of the SAR of the nanoparticles.

A finite element method-simulating tool, Ansoft HFSS, is used to study the field components in the solenoid and capacitor by simulating the exact experimental geometry, the results of which are shown in Figure 8-9.

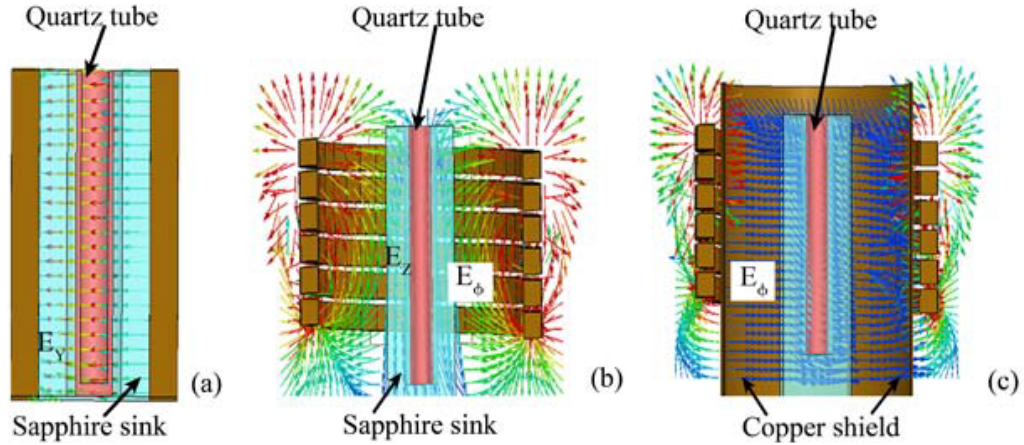


Figure 8-9 Electric fields in capacitor, solenoid and solenoid with shield

To study the distinctive effects of the E_z and E_ϕ fields in the solenoid, only E_z is changed because E_ϕ cannot be varied without disturbing the rf source. Hence, the

influence of E_ϕ on the sample is analyzed while suppressing E_z by imposing perfect-electric-conductor (PEC) boundary conditions. A PEC boundary condition refers to the boundary condition where the electric field is normal but the magnetic field is tangential to the surface. A cylindrical copper shield with a longitudinal single gap or multi gaps (to prevent eddy currents) is inserted in the solenoid to realize the PEC boundary condition as shown in Figure 8-9. *Rf* fields in the solenoid for samples with different permittivity and conductivity were simulated as presented in Figure 8-10.

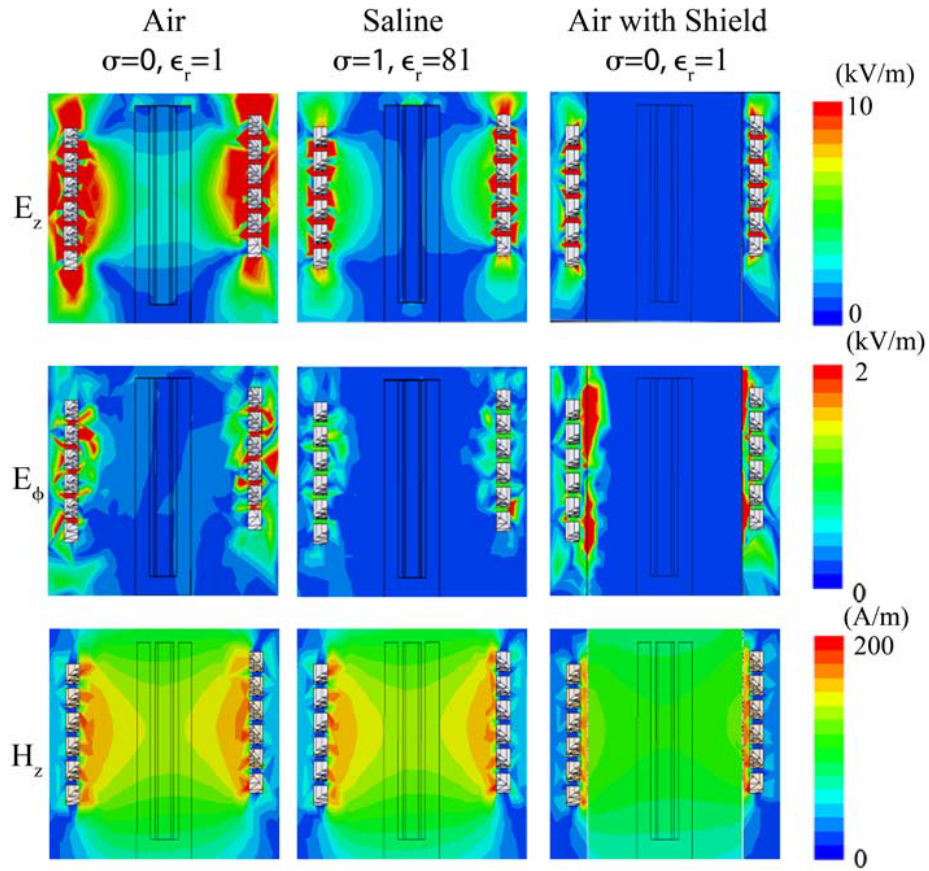


Figure 8-10 Fields E_z , E_ϕ , H_z for (a) empty quartz tube (b) quartz tube filled with physiological saline solution and (c) shielded solenoid with saline solution

Three components (E_z , E_ϕ , H_z) for each of the following cases: (1) empty (air) quartz tube ($\epsilon_r=1$, $\sigma=0$ S/m), (2) quartz tube filled with physiological saline solution ($\epsilon_r=81$, $\sigma=1.94$ S/m) and (3) shielded solenoid with saline solution are shown in Figure 8-10. The effect of the copper shield on E_ϕ , E_z and H_z field components in the solenoid clearly demonstrates a strong suppression of the E_z with only a slight reduction of E_ϕ and H_z components. Thus, to experimentally filter out conservative fields within a solenoid, realizing PEC conditions by shielding is significant.

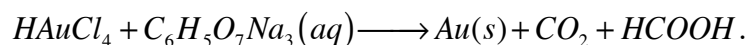
8.4 HEATING OF NANOPARTICLES PLACED IN CAPACITOR AND SOLENOID

From Section 8.3, it is evident that samples when placed in the solenoid will also exert an electric field E_s . Thus, this field E_s should be incorporated in our calorimetric equations to explain the heating of non-magnetic nanoparticles in the solenoid. For non-magnetic nanoparticles, the loss term due to magnetic field H_z is ignored. However for magnetic nanoparticles, an extra term would be added in the calorimetric-electromagnetic heat loss equation to account for the magnetic losses.

8.4.1 Heating of gold nanoparticles and control solutions in fields coupled in the capacitor and solenoid

Although huge numbers for the dissipative power of gold nanoparticles have been reported in literature, a new notion in contrast has been presented [38, 39] that heating is only ohmic due to ionic conduction from the bulk solution and that there is no heating from gold nanoparticles. This could be true to some extent as is evident from the results of conductive solutions.

To test such a concept of heating we used a meticulous protocol for the preparation of gold nanoparticles. It was studied that while gold nanoparticles are fabricated, citrate ions are flushed into the reagents. These ions will certainly increase the electrical conductivity of the bulk solution. These citrate ions act as reducing as well as capping agents for gold nanoparticles and thus help the gold nanoparticles to stay in colloidal forms by developing surface charge on the particles, thereby repelling particles which refrains them from coagulating. For example, 1.8 mL of 38 mM citrate is added to 15 mL of Au^{3+} for 15nm particles. The particle diameter can be varied by adding larger or smaller amounts of citrate to decrease or increase the particle size [110]. The standard fabrication protocol in terms of a chemical equation can be written as



Thus, proper control solutions accounting for the conductivity of citrate ions in the bulk have been prepared to test the gold nanoparticle heating and verify the high numbers for gold dissipation.

8.4.1a Preparation of control and test solutions for gold nanoparticles

Various sizes of commercial gold nanoparticles (5, 10, 20, 50, 100 and 200 nm) were obtained from Ted Pella Inc. as shown in Figure 8-11(a). Gold nanoparticles were ultra-centrifuged at 150000xg for one hour. The supernatants were collected and aliquots of each of the supernatants were purified using ZebaTM spin desalting columns 7K MWCO (Thermoscientific #89882), after equilibrating the columns with DI water. Aliquots of the stock solution, supernatant and filtrates were analyzed using the UV-Vis spectroscopy technique to check the presence of gold nanoparticles in it. The stock

solutions of the gold nanoparticles show a typical UV-Vis peak for the gold nanoparticles, which is absent or relatively very small (for particles of size 5, 10 and 20 nm) in the supernatant. However, the filtrates from the spin desalting columns are devoid of such peaks and the spectra are flat as evident from Figure 8-12.

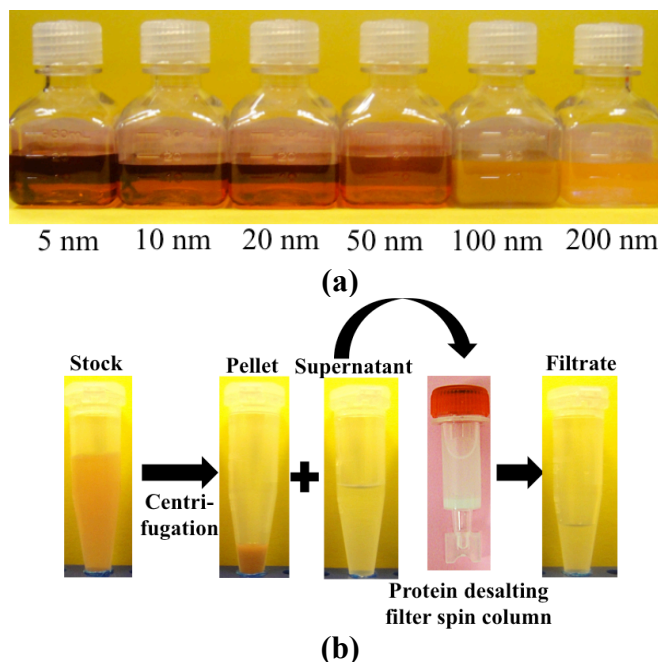


Figure 8-11 (a) Gold nanoparticle stock solutions (b) Centrifugation and filtrate preparation

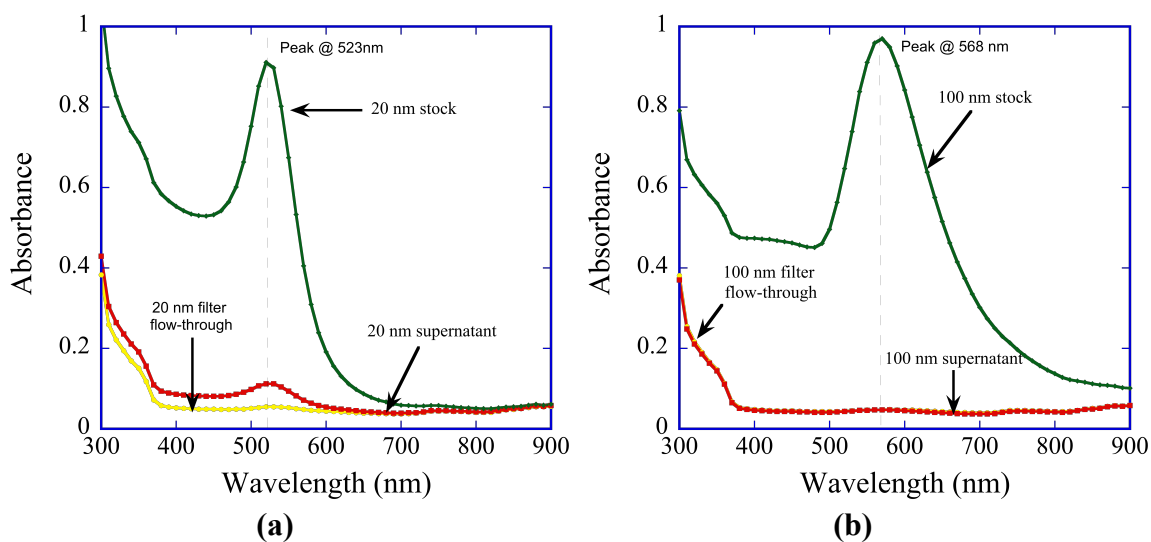


Figure 8-12 UV-Vis absorbance spectra for (a) 20 nm and (b) 100 nm gold nanoparticle's stock, supernatant and flow-through filtrate

Under this assumption, filtrates are used as control solutions for gold nanoparticle heating rather than DI water, considering that it contains everything but nanoparticles. The shift in the peak of about 45nm between 20 nm and 100 nm is accounted for the size difference in the particle. UV-Vis spectra also showed that there is no aggregation in the stock of gold nanoparticles. Scanning electron microscopic (SEM) analysis was also done to check on the population of nanoparticles and ensure the absence of nanoparticles in the respective filtrates of the gold nanoparticles. Micrographs shown in Figure 8-13 present an adequate population of nanoparticles for 20 and 100 nm stock samples. However, there is almost a negligible presence of the particles in filtrates for each of 20 and 100 nm filtrate samples.

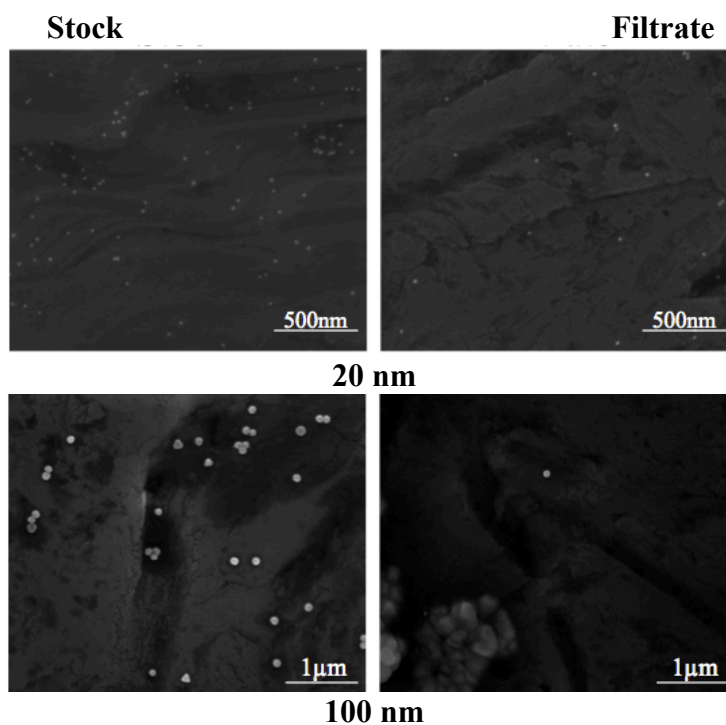
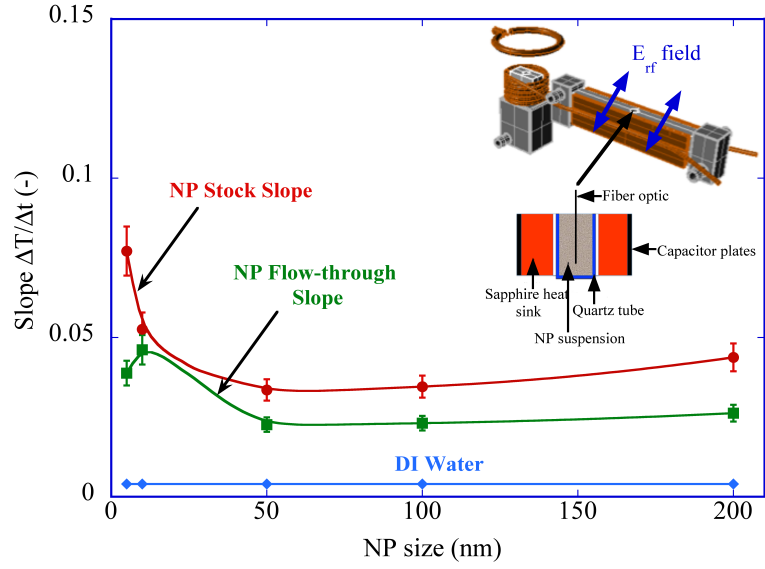


Figure 8-13 SEM images of 20 nm and 100 nm gold nanoparticles' stock and filtrate

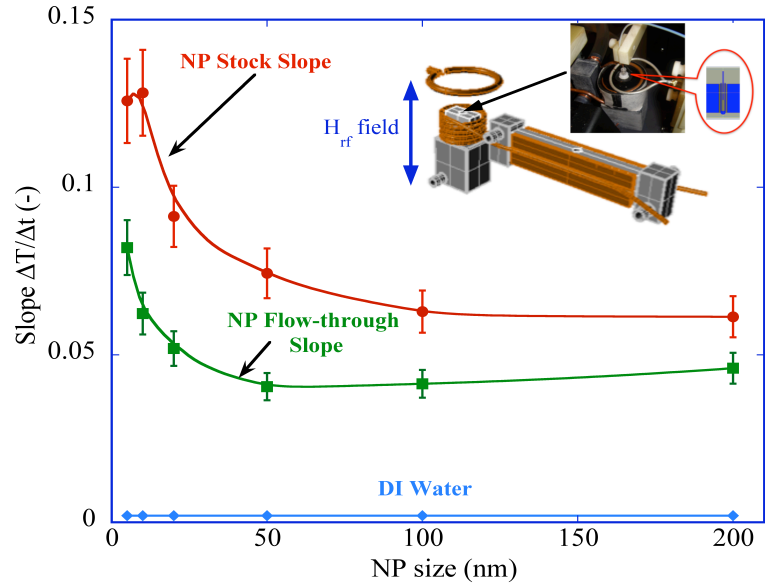
From these images, we can deduce that it's relatively easier to obtain filtrate for larger particles as filtrate for such particles is almost completely devoid of nanoparticles, however, smaller size particles, still show some very scarce population. Thus, we can finally assume that the filtrate has nothing but the dispersion medium.

8.4.1b Heating of gold nanoparticles and control solutions when placed in the solenoid and capacitor

The obtained stock solutions and filtrates as their respective test controls for 5, 10, 20, 50, 100 and 200 nm are exposed to *rf* fields in the capacitor and solenoid and the heating slopes are shown in Figure 8-14 (a) and (b) respectively. From Figure 8-14, the heating slopes of the gold nanoparticles following size dependence are observed. However we can ascertain that the dispersion medium (flow through filtrate) is also heating to a huge extent. Thus it is erroneous to consider DI water as a reference while analyzing gold nanoparticles' heating. There is certainly an enhancement due to nanoparticles, but the contribution is less than from the ohmic heating due to ionic conduction. Also, it is evident that in cases of 5, 10 and 20 nm sample, the filtrate demonstrates size dependence, which is attributed to the fact that not all of the gold population has been depleted from the suspensions. The smaller-sized particles are difficult to remove and are still there. But the slopes *versus* size for the dispersion medium of 50, 100 and 200 nm is almost a flat line. To calorimetrically analyze the heating slopes in the two fields, the calorimetric equations of nanoparticles' heating from Section 8.1.1 will be referenced here again.



(a)



(b)

Figure 8-14 Slope of heating of stock and filtrate of gold nanoparticle suspensions versus particle size (a) when placed in the capacitor (b) when placed in the solenoid

To determine the conductivity of the filtrate, the Equation 8.6 is used again. However, a depolarization factor $\gamma^m(\sigma)$ [111] due to free ion charges in the sample is used here to properly scale the local fields for the capacitor as the sample in the quartz

tube is oriented in a direction perpendicular to the local electric field $E_L = \beta E_y$. The depolarization factor in a form of a Debye factor is derived as

$$\gamma(\sigma) = \left| \frac{1}{1 + j \left(\frac{\omega_p(\sigma)}{\omega} \right)} \right|^2 = \frac{1}{1 + \left(\frac{\omega_p(\sigma)}{\omega} \right)^2}, \quad (8.10)$$

where, $\omega_p(s) = \sigma L / \pi a \epsilon_0 \epsilon_s$, with sample tube length $L = 15$ mm and inner radius $a = 1.4$ mm. $\epsilon_0 \epsilon_s$ is the permittivity of the nanoparticle solution and ω is the resonant frequency of the resonator. Thus, Equation 8.2 is rewritten as

$$P = C_{ps} \rho_s q^m = \frac{1}{2} \sigma_{sample} \left[\gamma^m(\sigma_{sample}) |E_L^m|^2 \right]. \quad (8.11)$$

This equation holds true for all non-magnetic samples even when placed in a solenoid, as there is no heat loss associated due to magnetic field for non-magnetic particles. As from the simulations in Section 8.3, the total E_s of conservative E_z and induced E_ϕ electric fields is revealed to be present in the solenoid. To calibrate the resonator's field, slopes of 2.5 mM NaCl salt solution ($\sigma_{salt} = 0.0314$ S/m, $\gamma^c = 0.57$), placed in the capacitor and the solenoid from section 8.2.2 are used as references to determine the local electric field components in the solenoid ($E_L^{s0} = E_s$) and in the capacitor ($E_L^c = \beta E_y$) from Equation 8.10. Table 8.4 shows such calibrated values of local electric fields.

Table 8.4 Calibrated local electric field values in the particular configuration from the slopes of NaCl solution heating

Configuration	Slope q_{salt}	Local electric field E_L (kV/m)
Capacitor 'c'	0.03672	4.145 (βE_y)
Solenoid 's0'	0.06262	4.083 (E_s)

From the local βE_y , where the field across the capacitor E_y is determined to be 37.68 kV/m is very close to the measured value of 45 kV/m using our experimental capacitive divider arrangement. Slope values from the heating curves are tabulated in Table 8.5.

Table 8.5 Slopes of filtrate and nanoparticle samples in the capacitor and solenoid

Size (nm)	Volume Fraction	Slope of filtrate		Slope of NP	
		Cap	Sol	Cap	Sol
5	3.27×10^{-6}	0.039	0.082	0.077	0.126
10	2.98×10^{-6}	0.046	0.062	0.053	0.128
50	2.94×10^{-6}	0.023	0.041	0.034	0.074
100	2.93×10^{-6}	0.023	0.041	0.035	0.063
200	2.93×10^{-6}	0.026	0.046	0.044	0.061

Replacing E with βE_y and E_s in Equations 8.6 and 8.8, conductivity of the filtrate (as the suspending solution) and conductivity of the nanoparticle solutions are calculated for different sizes. With these conductivity values, SAR for gold nanoparticle samples placed in the capacitor and solenoid, referenced to the dispersion medium are calculated from Equation 8.9 and the values are presented in Table 8.6

From the table, it is evident that the values of SAR of the gold particles are not as high as reported by other research groups (Table 3.1) and is two to three orders of magnitude less. Unlike the previous studies, there is certainly a very small contribution of nanoparticles to heat enhancement, but for SAR calculations, proper dispersion medium characterization is necessary as a huge contribution of heating comes from the Joule heating of the ionic conduction from the electrolytic suspension, which would result in an inaccurate SAR calculation. The contribution of nanoparticle heating is

attributed to the interaction of the enhanced dipole fields due to polarization and nanoparticle-electrolyte interface.

Table 8.6 Calculated effective conductivity and SAR calculation for Gold filtrate and nanoparticle suspensions

Size (nm)	Volume Fraction	Cond. of filtrate		Cond. of nanoparticle		SAR of nanoparticle	
		(S/m)		(S/m)		(W/kg)	
		Cap	Sol	Cap	Sol	Cap	Sol
5	3.27×10^{-6}	0.019	0.041	5.7×10^3	6.7×10^3	2.5×10^6	2.9×10^6
10	2.98×10^{-6}	0.022	0.031	1.1×10^3	1.1×10^4	4.7×10^5	4.8×10^6
50	2.94×10^{-6}	0.011	0.020	1.8×10^3	5.8×10^3	8.1×10^5	2.5×10^6
100	2.93×10^{-6}	0.011	0.021	1.9×10^3	3.7×10^3	8.5×10^5	1.6×10^6
200	2.93×10^{-6}	0.013	0.023	2.9×10^3	2.6×10^3	1.3×10^6	1.1×10^6

8.4.2 Heating of silica nanoparticles and control solutions in fields coupled in the capacitor and solenoid

8.4.2a Preparation of control solutions for silica nanoparticle

100 and 200 nm sized monodispersed silica beads with a density of 2 g/cm^3 in a concentration of 50 mg/mL were commercially obtained from Kisker-Biotech. Silica beads were centrifuged at 5000 rpm for 20 min. Like the process for the gold nanoparticles, the supernatants of the silica nanoparticles were collected and the aliquots for each of the samples were purified using ZebaTM spin desalting columns 7K MWCO (Thermoscientific #89882) after equilibrating the columns with DI water.

Figure 8-15 (b) shows the UV-Vis analysis of aliquots of the stock solution, supernatant and filtrates.

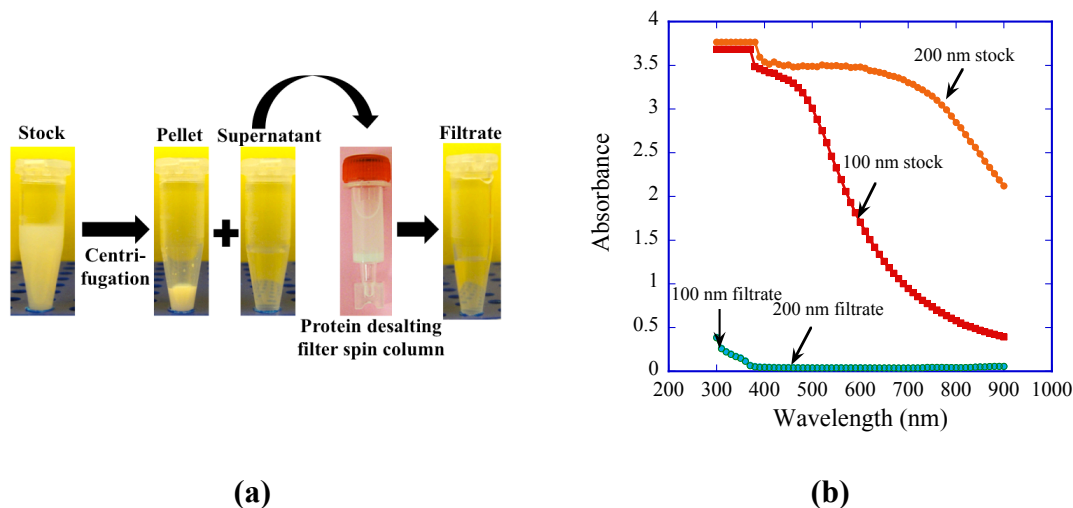


Figure 8-15 (a) Process for obtaining filtrate as a control solution from the silica nanoparticle stock solution (b) UV- Vis on filtrate and silica stock solutions

SEM micrographs for the silica stock and filtrate samples are shown in Figure 8-16. Silica particles are not supposed to show any characteristic absorbance peak in the UV-vis analysis. However the absorbance background from the UV-vis analysis shows a distinction between the stock and the filtrate as shown in Figure 8-15 (b). SEM images presented in Figure 8-16 complementally show how the population of silica nanoparticles is radically reduced in filtrate.

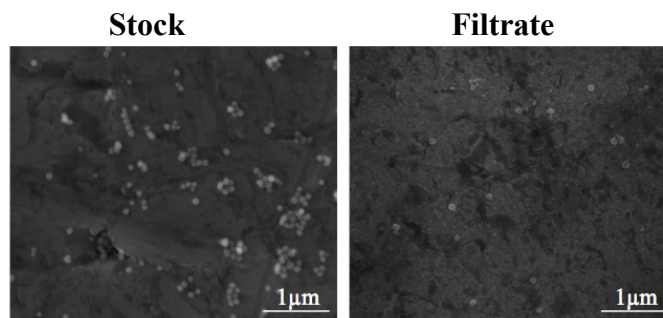


Figure 8-16 SEM micrographs for stock and filtrate of 100 nm silica nanoparticles

8.4.2b Heating of silica nanoparticles and control solutions when placed in the solenoid and capacitor

Thermo-graphic data for silica nanoparticle suspensions and the filtrates were analyzed by placing them in the capacitor and solenoid. From Figure 8-17, we can see that the dispersion medium for 100 and 200 nm silica is heated with a similar slope as for the bigger particle sizes it is relatively easier to remove the nanoparticles and obtain the same dispersion medium electrochemically. The differences in the slope for 200 nm, when placed in the solenoid and in the capacitor, are slight and are accounted to the experimental error. Such changes in the slope can certainly affect the SAR, however the order of SAR's magnitude is not drastically changed as found from the calorimetric analysis.

From similar equations as used for the gold particles' analysis, effective conductivity and SAR values for filtrates and stocks for silica nanoparticles are obtained and presented in Table 8.7. The volume fractions of the silica nanoparticles used in the study are the same and calculated as 0.025 based on the 50 mg/mL concentration of sample and 2 g/cm^3 as material density of silica as found from Kisker Biotech. The comparison between the results of the gold and silica nanoparticles from Table 8.6 and Table 8.7 determines that the SAR of gold nanoparticles is three orders of magnitude higher than that of the silica particles.

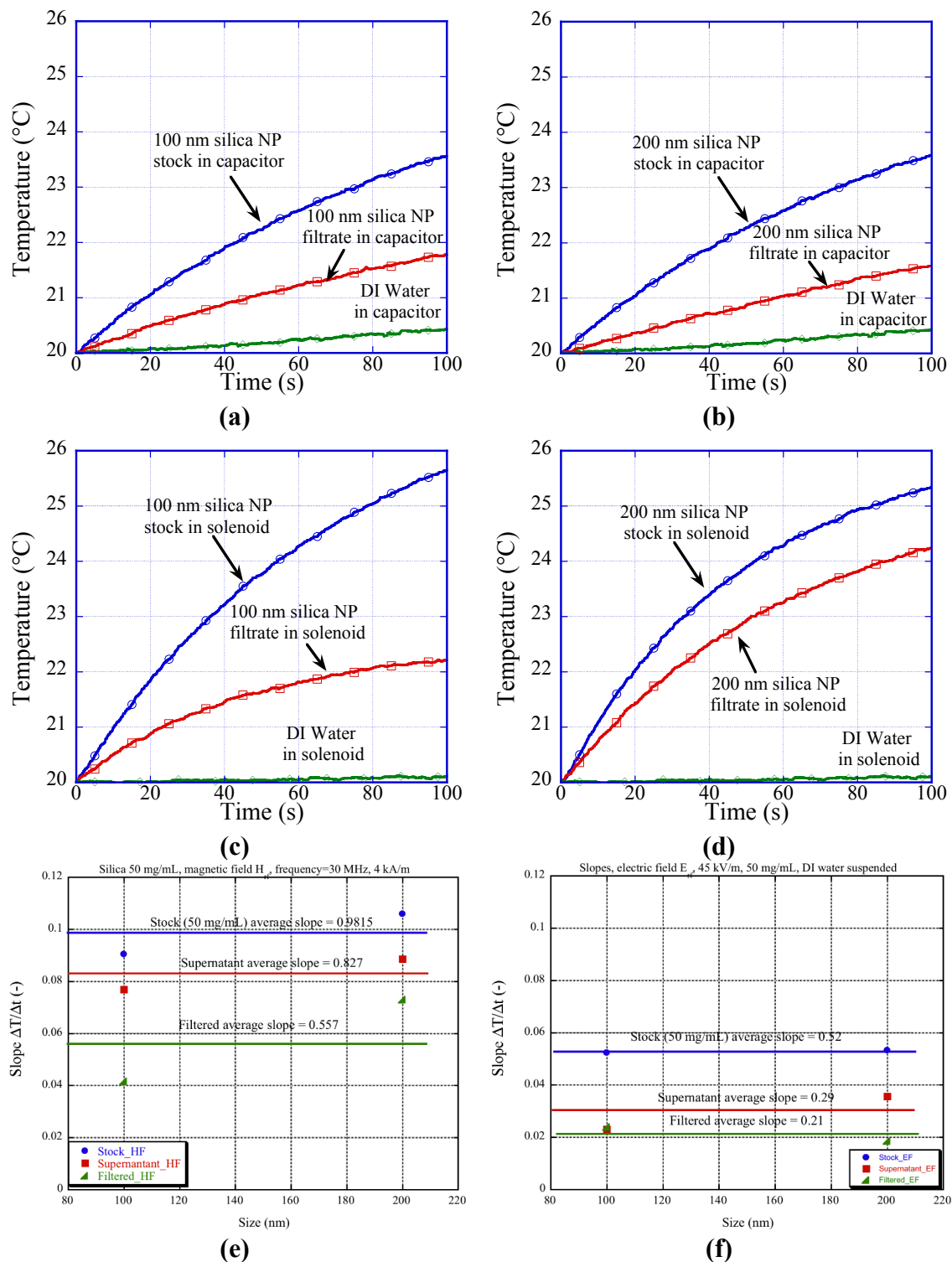


Figure 8-17 Slopes of filtrate and stock solutions for 100 nm and 200 nm silica NPs

Table 8.7 Calculated effective conductivity and SAR calculation for silica filtrate and nanoparticle suspensions

Size (nm)	Volume Fraction	Cond. of filtrate (S/m)		Cond. of NP (S/m)		SAR of NP (W/kg)	
		Cap	Sol	Cap	Sol	Cap	Sol
100	0.025	0.012	0.021	0.563	0.999	2418	4163.6
200	0.025	0.009	0.037	0.683	0.697	2933.7	2904.9

We have definitely ruled out the basis of dielectric/ohmic loss from the material's bulk to justify this loss. This loss behavior can be explained from the phenomena of polarization of nanoparticles due to the induction of electric fields as shown from COMSOL simulations in Section 3.4.2b. The dipole field enhancement for the gold nanoparticle was found to be three times higher than the silica nanoparticle. Such an analysis has been performed by Dr. Patrick Xie and Dr. Jarek Wosik, however it is not incorporated into this work. This analysis gives an insight to use physiologically relevant environments to modify the nanoparticle's surface, which would enhance the SAR from the nanoparticle.

8.4.3 Electric field heating of silica nanoparticles with different ambiances

Adsorbing proteins at the nanoparticle-water interface can change the surface chemistry of the bare nanoparticles and enhances their ability to be used as potential multifunctional nanoconstructs. The biocompatibility and biodegradability of silica makes it suitable for biomedical applications. A study to analyze the effect of physiologically relevant environments on heating efficiency of silica particles is done

as shown in Figure 8-18. 200 μL of silica beads (Kisker-Biotech) 30, 50 and 100 nm in diameter of density 2 g/cm^3 in a concentration of 50 mg/mL were added directly to bovine serum albumin (BSA)(Sigma-Aldrich) at 2% w/v and fetal bovine serum (FBS) at 10% v/v. The samples were then centrifuged at 5000xg for 20 min and supernatant saved. The albumin and FBS covered particles were then re-suspended in 200 μL DI water.

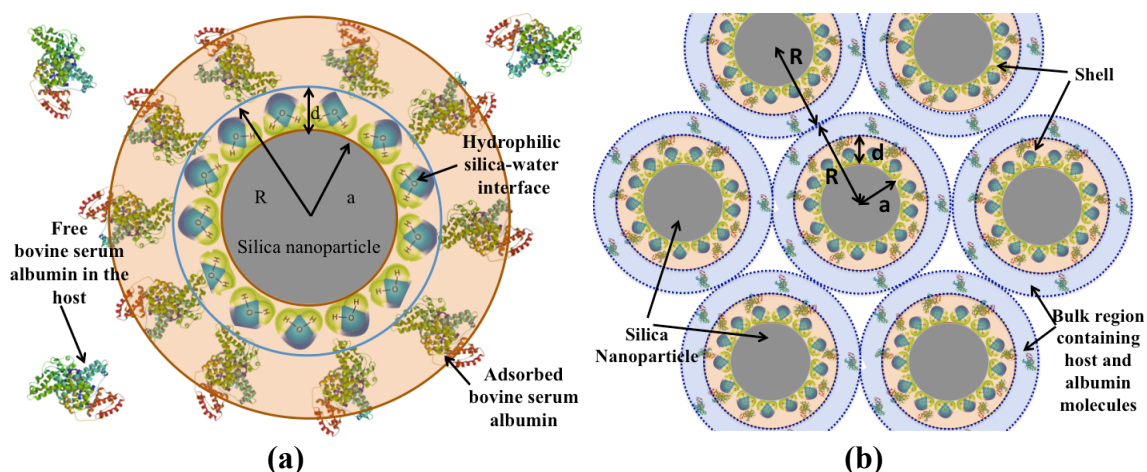


Figure 8-18 Composite silica particle used in the study entailing silica, silica-water charged interface, adsorbed albumin and water solution

Each of the samples of silica beads with albumin, supernatant and silica beads with albumin re-suspended in DI water were analyzed by using Malvern NanoZS for their zeta potential and hydrodynamic radius using the dynamic light scattering technique. The absorption of albumin on the surface of silica is evident from the change in hydrodynamic radius as recorded in Table 8.8. Temperature increase of 150 μL of samples of bare and surface modified silica nanoparticles, following 400 seconds of exposure in rf electric field at 50 MHz are summarized in Figure 8-19. The voltage across the capacitor's plate was measured to be 173 V, which corresponds to a βE_y of

9.7 kV/m. The volume fraction of the particles is the same throughout the study and is calculated using Equation 3.15 as 0.025.

Table 8.8 Hydrodynamic radius of bare and BSA adsorbed silica NPs

Albumin %	Hydrodynamic radius (nm) from DLS		
	30 nm	50 nm	100nm
0%	32.2	56.27	116.2
0.5%	32.68	59.74	117.2
1%	36.81	56.54	117.6
2%	35.5	58.58	120.4
4%	39.05	60.98	122.1

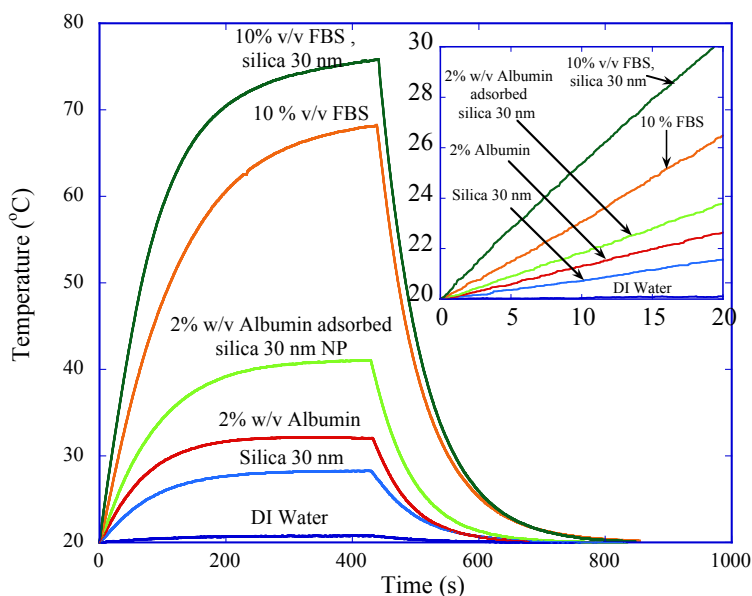


Figure 8-19 Thermographic results of heating of 30 nm silica particles in 2% w/v BSA and in 10 % v/v FBS and their respective controls including DI Water

Using Equations 8.6, 8.8 and 8.9, the conductivities and SARs for respective dispersion control mediums and silica nanoparticles suspensions presented in Table 8.9 and Table 8.10 respectively.

Table 8.9 Conductivities and SARs for dispersion mediums

Control sample	Slope (q)	Conductivity (S/m)	SAR (W/kg)
DI Water(Cond. Filtrate)	0.0049	0.000435(0.005)	20.46(235.22)
2% w/v Albumin	0.1351	0.012	564.54
10 %w/v FBS	0.3268	0.029	1364.3

Table 8.10 Conductivities and SARs for bare and modified silica nanoparticles

Silica NP sample	Slope (q)	Conductivity (S/m)	SAR (W/kg)
Bare 30 nm Silica	0.0795	0.2656(0.08756)	6247.1(2059.63)
30nm, 2% w/v Albumin	0.1908	0.2101	4942.1
30nm, 10 %w/v FBS	0.5140	0.6958	16367

From the tables above, we see that there is a SAR overestimation, if we take DI water as a dispersion medium for bare 30 nm silica particles. For correct analysis, proper dispersion medium must be obtained, but segregating conductive dispersion medium from 30 nm silica particles is a cumbersome process and was unsuccessful as the particle size is very small. However in Section 8.4.2, we have analyzed the conductivity value of the dispersion medium for 100 and 200 nm particles solution, which cannot be disregarded as it accounts for a major portion of the heating from silica nanoparticle suspension. Since, these measurements are done at 50 MHz, a plausible choice for conductivity of control should be a value more than DI water and less than the conductivity of filtrate at 30 MHz. Hence assuming a conductive control solution with 0.005 S/m as effective conductivity, we recalculate the conductivity of bare 30 nm silica as 0.08756 S/m, which gives a relatively precise SAR value of 2059.63. Thus,

even though conductive buffers and proteins will show hyperthermia when exposed to *rf* electric fields, the nanoparticles have a synergistic effect on the heating which is confirmed from the SAR numbers recorded in Table 8.10. There is an approximate 2.5 and 8 times enhancement in SAR for the silica particles with ionic environment varied due to respective BSA and FBS, in comparison to bare silica particles.

In the present study, the SAR of the silica nanoparticle is enhanced from 2060 to 4942 and 16367 for 2% Albumin and 10 % FBS respectively. This confirms that the main mechanism of heating of particles in the electric field is due to the nanoparticle-electrolyte ion interface. The double layer contributes to the loss enhancement resulted from polarization at the nanoparticle surface induced by the external electric fields. This also leads to the perception that the cellular and sub-cellular microenvironment around these particles (when injected directly or systemically in the lesions) would emphatically enhance the *rf* energy absorption. This study was continued with silica nanoparticles with 0.5, 1, 2 and 4% BSA solutions with slopes plotted in Figure 8-20.

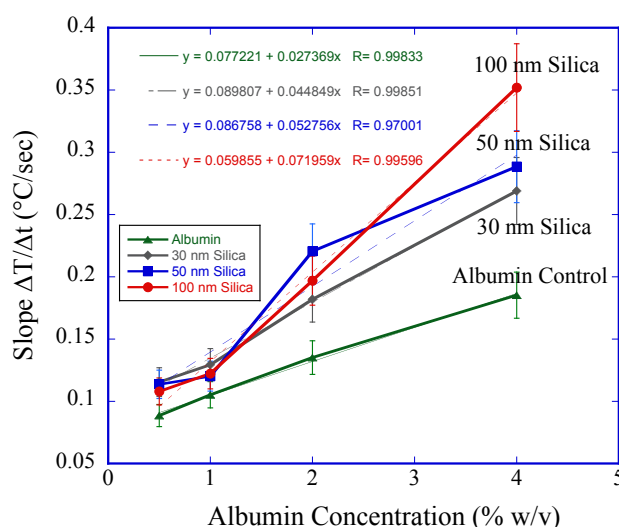


Figure 8-20 Slopes for temperature rises *versus* albumin concentrations for 30, 50 and 100 nm silica nanoparticles

From Figure 8-20, it is observed that albumin concentration affects the heating efficiency for the silica particle. The largest particle with the largest albumin concentration is found to be the most *rf* energy dissipative. We see that at 0.5% concentration of albumin, there is a small to large particle size heating order, which gets reversed at higher concentrations, distinctively at 4%. The proteins concentration in the physiological environments would vary depending on tissues and cells, however to better understand the particle heating dynamics, the critical point for the change in behavior could be analyzed.

8.4.4 Preliminary results of magnetic field and electric field heating of super paramagnetic iron oxide nanoparticles

The stock solutions of 5 nm and 10 nm SPIO (Sigma–Aldrich) were diluted 2, 4, 8, 16, 32 and 64-folds and were exposed to *rf* fields in the capacitor and solenoid. Figure 8-21 demonstrates the heating trends in the solenoid and capacitor showing the highest heating rate at about 8-fold dilution.

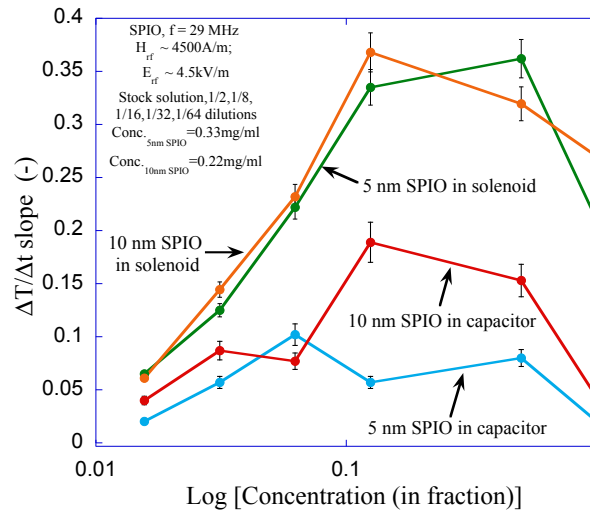


Figure 8-21 Heating slopes of SPIO in electric and magnetic fields *versus* the concentration fraction

From the magnetic field loss point of view, it could be considered that the SPIO clusters separated with increasing dilution, but at the same time the similar trend in the electric field in the capacitor proves that the conductivity of the medium is definitely playing a certain role in the behavior. As revealed before, different concentrations of NaCl also showed similar nonlinear heating when placed in the electric field, which determines that it is nothing but the electrolytic bulk's heating. Hence, the next step is to filter the electric field E_z out of the solenoid as E_z has a significant contribution to the total electric field E_s . This shielding of E_z would enable us to properly study the effect of H_z on iron oxide nanoparticles. To achieve this, perfect electrical boundary conditions should be established, for which primitively a copper shield with a vertical slit in-between is placed around the quartz tube and placed in the solenoid. This shield is also termed as a loop gap cylinder [108].

The three samples, 10 nm water-based iron-oxide particles (Sigma Aldrich), water-suspended 5 nm iron oxide nanoparticles embedded in a dextran matrix (Sienna+® from Endomagnetics Ltd) and 5nm gold particles as a magnetic control were tested in three configurations; capacitor, solenoid and solenoid with a shield. Figure 8-22, shows the TEM images of SPIO nanoparticles used in the study. Hence, three different slopes ($q=dT/dt$) q^c , q^{s0} , and q^{ss} were measured for the capacitor (E_y), solenoid (E_ϕ , E_z and H_z) and shielded solenoid (E_ϕ and H_z), respectively for the initial 20 seconds of temperature increase. Figure 8-23 depicts the heating curves for these samples.

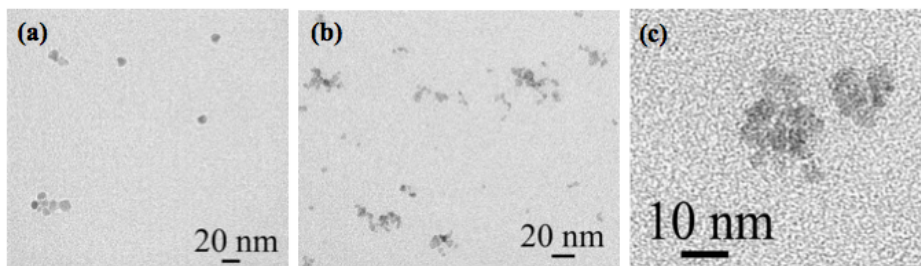


Figure 8-22 TEM Images of SPIO (a) 5nm Sigma (b) 5nm Endomag (c) Dextran matrix showing the SPIO nanoparticles embedded in it

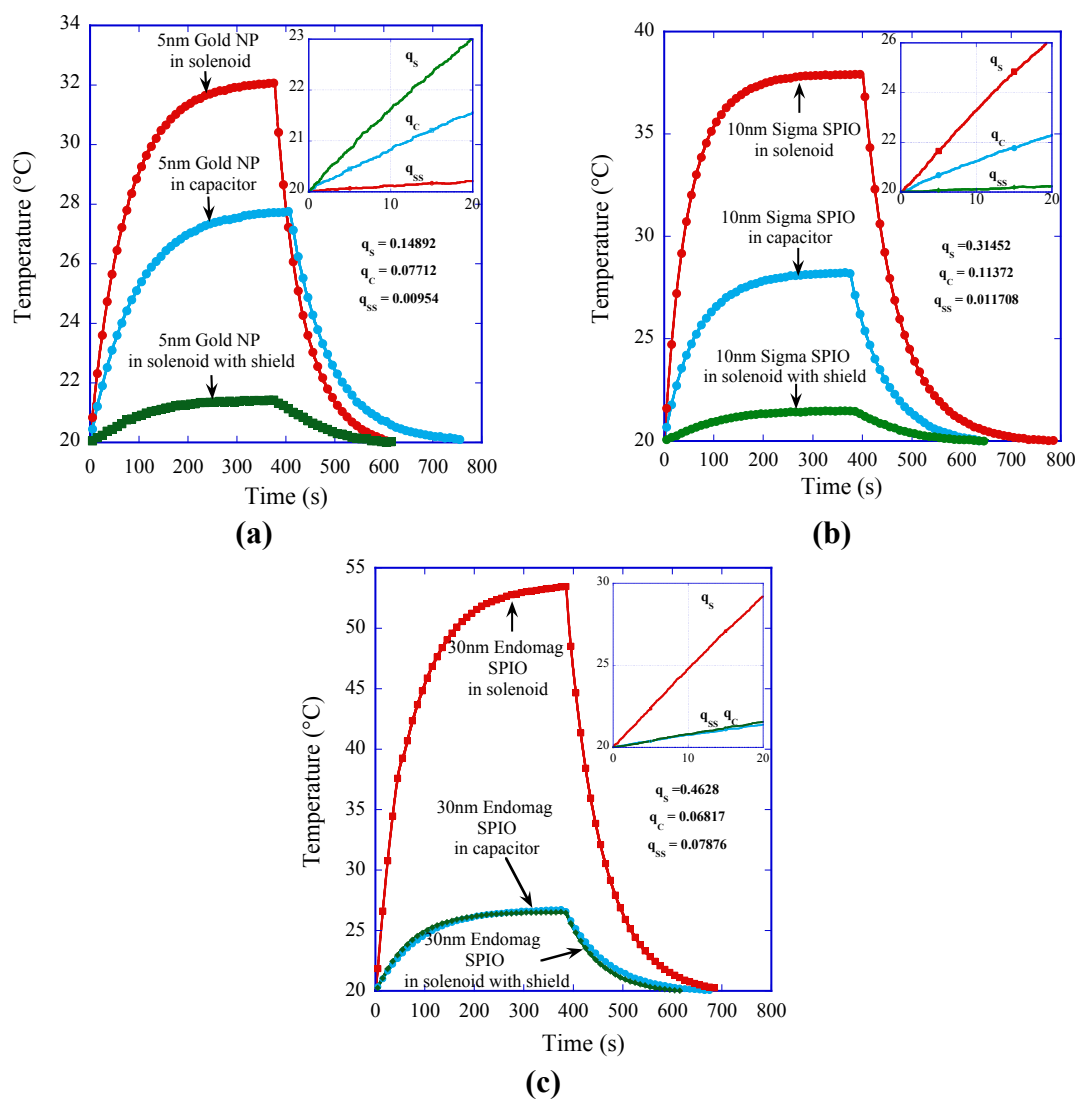


Figure 8-23 Nanoparticle samples placed in solenoid, capacitor and solenoid with shield for (a) 5 nm Au nanoparticle as magnetic control (b) 10 nm Sigma SPIO nanoparticle (c) 30 nm Endomag SPIO

It is observed that when 5 nm gold nanoparticles (which are theoretically devoid of any magnetization) placed in the solenoid with shield configuration, the slope of heating is the least. In such a configuration, the only interaction of the nanoparticles is with magnetic field H_z and its counterpart E_ϕ . From the slopes for the three cases it is evident that in the solenoid with shield configuration, Endomag SPIO is heated the most, followed by Sigma SPIO and then gold nanoparticles, which was heated the least. Gold particles have no magnetization. The fact that the Endomag heated higher than the sigma SPIO is referenced to the room temperature AC magnetization measurements, where it was found that Endomag particles have higher AC magnetization than the 5 nm Sigma particles.

8.5 RESULTS OF SHIELDING ON ENDOMAG IRON OXIDE PARTICLES

The heating of water-suspended 5 nm SPIO nanoparticles from Endomagnetics was studied using a proper shielding method using a new resonator with similar design principal but a properly placed shield next to the field coil, so that no heat is transferred due to conduction from the coil itself. The SPIO nanoparticles are embedded in the dextran matrix and were characterized for the average hydrodynamic diameter, size distribution and zeta potential using ZetaSizer Nano ZS (Malvern). The measurement of the average diameter of dextran surrounded 5 nm iron oxide clusters was found to be ~ 31.7 nm. The zeta potential measurements show a negative zeta potential of -24.6 mV, which renders them colloiddally mono-dispersed. The SEM and TEM analysis as shown in Figure 8.22 also confirmed the size of the dextran embedded SPIO nanoparticles.

Temperature *versus* time curves for SPIO samples with two different volume fractions placed in a quartz tube in three different rf field configurations (capacitor, solenoid and solenoid with shield) at 30 MHz are presented in Figure 8.24.

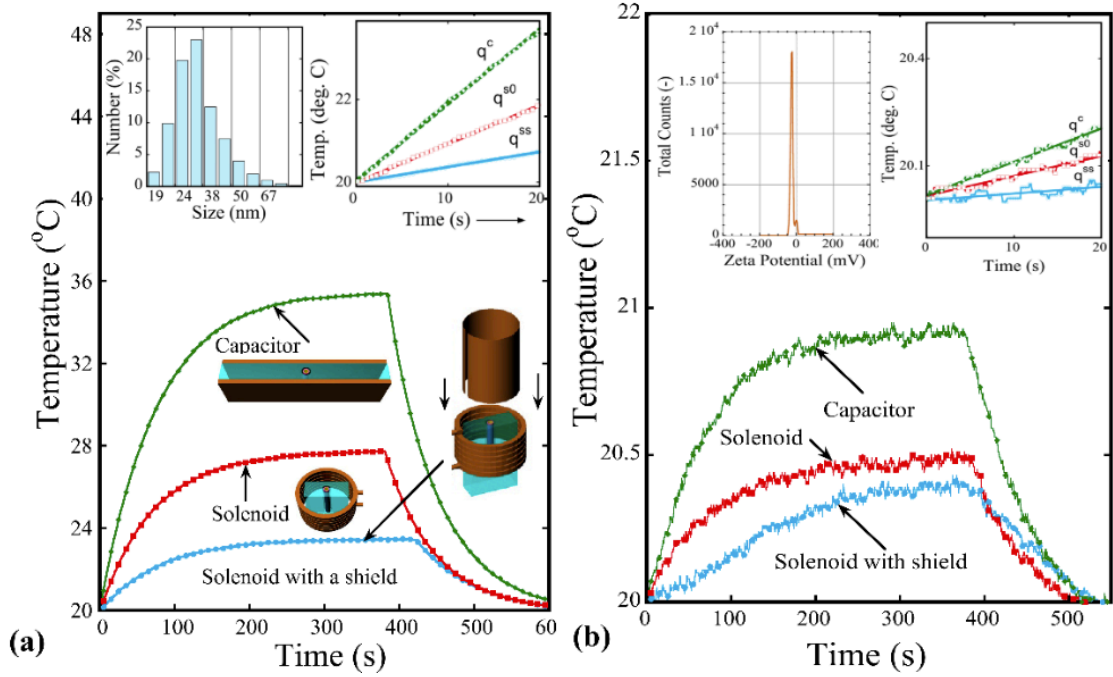


Figure 8-24 Temperature *versus* time plotted for SPIO (a) 28 mg/mL (b) 1 mg/mL SPIO measured in three rf fields configurations

To accommodate for magnetic losses, Equation 8.11 is modified such that

$$P = C_{ps} \rho_s q^m = \frac{1}{2} \sigma_{sample} \left[\gamma^m(\sigma_{sample}) |E_L^m|^2 \right] + \pi \mu_0 f \chi'' |H|^2 v_f. \quad (8.12)$$

Here v_f is the volume fraction of SPIO nanoparticles in the suspension, for the resonator's field calibration, 2.5 mM NaCl salt solution ($\sigma_{salt}=0.0314$ S/m, $\gamma^c=0.57$, $\chi''=0$, $v_f=0$) was used as a reference again. Respective slopes were used to calculate the local electric field components (in solenoid $E_L^{s0} = E_s$, in solenoid with the shield $E_L^{ss} = E_\phi$ and in the capacitor $E_L^c = \beta E_y$) from Equation 8.12 and their values are shown in Table 8.11.

Table 8.11 Slope values of NaCl and calculated local fields values for the three configurations

Configuration	Slope q_{salt}	Local electric field E_L (kV/m)	H_z (kA/m)
Capacitor ‘c’	0.02557	3.46 (βE_y)	0
Solenoid ‘s0’	0.01408	1.936 (E_s)	8.2
Solenoid with shield ‘ss’	0.00227	0.776 (E_ϕ)	7.1

The conservative electric field component $E_z = \sqrt{(E_s)^2 - (E_\phi)^2}$ is estimated as 1.7 kV/m.

The heating slopes for the different configurations are summarized in Table 8.12.

Table 8.12 Slope values of SPIO for the three configurations

Configuration	Slope q_{spio}^m (28 mg/mL)	Slope q_{spio}^m (1 mg/mL)
Capacitor “c”	0.1832	0.009255
Solenoid “s0”	0.093635	0.005501
Solenoid with shield “ss”	0.0364	0.001868

The two concentrations of SPIO nanoparticles studied here are 28 mg/mL and 1 mg/mL. Assuming mass density of the SPIO $\rho_{\text{NP}}=5.17 \times 10^3 \text{ kg/m}^3$, the volume fractions are calculated as $v_{f1}=5.4 \times 10^{-3}$ and $v_{f2}=1.96 \times 10^{-4}$ using Equation 3.14. Since there is no magnetic field present in capacitor and hence no magnetic loss, the conductivity of the suspensions can be calculated by substituting q^c for the two samples in Equation 8.12 as $\sigma_{\text{sample1}}=0.13 \text{ S/m}$ and $\sigma_{\text{sample2}}=0.0038 \text{ S/m}$. Further, for a colloidal suspension the effective conductivity of the nanoparticles suspension in the capacitor can be expressed as

$$\sigma_{\text{sample}} = \sigma_{\text{NP}} v_f + \sigma_{\text{sol}} (1 - v_f). \quad (8.13)$$

Substituting the volume fractions v_{f1} and v_{f2} and calculated effective conductivities σ_{sample1} and σ_{sample2} in Equation 8.13, the unknown variables σ_{NP} and σ_{sol} are solved and the conductivities of the SPIO-dextran nanoparticle complex and the dispersion medium are estimated as $\sigma_{\text{NP}}=23.16$ S/m and $\sigma_{\text{sol}}=0.002$ S/m.

In order to determine the magnetic loss of the SPIO nanoparticles, the calorimetric equations for the sample in the solenoid with the shield derived from Equation 8.12 is

$$2C_{ps}\rho_s q_{sus}^{ss} = \sigma_{sus} |E_\phi|^2 + 2\pi\mu_0 f \chi'' |H_z|^2 v_f, \quad (8.14)$$

from which susceptibility can be extracted as

$$\chi'' = \left(\frac{2C_{ps}\rho_s q_{sus}^{ss} - \sigma_{sus} |E_\phi|^2}{2\pi\mu_0 f |H_z|^2 v_f} \right). \quad (8.15)$$

Substituting the values of fields and slopes from Table 8.11 and 8.12 we get $\chi''_1=0.0038$ for 28 mg/mL SPIO, and $\chi''_2=0.0055$ for 1mg/mL SPIO nanoparticle suspensions. In order to better quantify the heating exclusively in E_{rf} and H_{rf} , SAR of the nanoparticles are expressed as

$$SAR_E = \frac{\sigma_{\text{sample}}}{\rho_{\text{sample}}} |E_L|^2, \quad (8.16)$$

and

$$SAR_M = \frac{\pi\mu_0 \chi''}{\rho_{NP}} f |H_z|^2. \quad (8.17)$$

From the mass density of the SPIO $\rho_{\text{NP}}=5.17 \times 10^3$ kg/m³ and of the solution $\rho_{\text{sol}}=\rho_{\text{water}}=10^3$ kg/m³, SAR of the nanoparticles and solution are calculated in the

electric field $\beta E_y = 3.46$ kV/m as 27 kW/kg and 2 W/kg, respectively. The imaginary part of magnetic susceptibility and magnetic SAR of the SPIO nanoparticles are presented in Table 8.13.

Table 8.13 Magnetic SAR of Endomag iron oxide nanoparticles

Concentration (mg/mL)	V_f	χ''	SAR_M (W/kg)	SAR_M/fH^2 (Wsm ² /kgA ²)
28	5.4×10^{-3}	0.0038	4.1×10^3	2.9×10^{-12}
1	1.96×10^{-4}	0.0054	5.86×10^3	4.16×10^{-12}

Therefore, these results show how the method using shielding and both fields to analyze iron oxide nanoparticle allows to singularize and to calculate specifically the contributions of electric and magnetic fields to the overall thermal efficiency. If SAR numbers would be calculated the way they are typically done in the literature assuming E_s field induced loss as a magnetic loss, the magnetic SAR_M would be calculated with a huge error percentage.

Chapter 9 Conclusions and future work

Limited penetration depth of ionizing radiations acknowledges the clinical acceptance of *rf* regimes of electromagnetic spectrum for cellular and sub-cellular studies and disease theranostics. While working with *rf* electromagnetic fields, this dissertation is a comprehensive study of *rf* induced thermal effects and the characterization of biomatter and nanoparticles, to evaluate their candidacy as *rf* energy absorption enhancers for thermo-therapeutic applications. The physics of mechanism of heating of these magnetic and non-magnetic particles is not clear and needs to be investigated. The exposé of the mechanisms of nanoparticle's heating in *rf* electric and magnetic fields is very imperative for designing and characterizing therapeutic systems for targeted hyperthermia. The summary of this dissertation can be outlined as follows:

- ❖ Heating of the magnetic and non-magnetic nanoparticles is studied using *rf* fields, inductively and capacitively coupled to colloidal suspensions of nanoparticles by placing them in the solenoid and capacitor of a unique LCR resonator designed.
- ❖ Sets of calorimetric and electromagnetic equations are derived to identify all *rf* components from the dispersion medium and the nanoparticles, thereby extracting the effective conductivity of nanoparticles. This allowed us to estimate heat loss exclusively from the nanoparticles. The clinically used cancer hyperthermia devices are based on the MHz regime of frequencies where the contribution of the dispersion medium to the overall heating is inevitable. Hence the characterization of the dispersion medium is well presented in this work. To experimentally determine and singularize nanoparticle's contribution to heat enhancement with respect to dispersion medium, control solutions for respective nanoparticles suspensions are prepared by ultra-

centrifuging the nanoparticle suspensions with subsequent purification of supernatants using desalting columns.

❖ Unlike very large SAR numbers reported previously for the gold NPs, it is found that a significant contribution of heat loss from these nanoparticle suspensions comes from the ionic conduction in electrolytic dispersion medium causing Joule Lenz heating. As a result we have concluded that previously reported SARs on gold nanoparticles were overestimated and their values are three orders in magnitude higher. Electric SARs for gold, silica and iron oxide nanoparticles were calculated as ~ 1000 , 2 and 27 kW/kg respectively.

❖ We have analyzed all the *rf* field components in the solenoid and it is found that the neglected-in-literature conservative *rf* electric field component (E_z component along the solenoid axis) has a very considerable effect on the heat response from the conductive suspensions. It indicates that most of the literature data overestimated the SAR of magnetic and non-magnetic particles in MHz range of frequencies.

❖ To study magnetic nanoparticles, the solenoid coil with/without an *rf* electric field shield is proposed to set perfect electric boundary conditions so that conservative field is shielded out, resulting only in H_z field left inside the solenoid. This method allows a more precise way of calculating SAR for iron oxide nanoparticles. Magnetic SAR for iron oxide was calculated as 4 kW/kg. A need to normalize the SAR with respect to frequency and field strength is identified, so that comparison between heating at different field strengths and frequencies could be done.

❖ It has been reiterated that the small amount of electric field heating observed for nanoparticles suspensions with a small volume fraction is not due to ohmic heating or

viscous losses. The rf loss is strongly ascribed to the interaction of dipole fields on the nanoparticle due to polarization with particle-electrolyte interface. From the analysis of particle polarization in the presence of an external field, it was established that the dipole fields on metallic gold nanoparticles are two (3x for gold, 1.5 x for silica) times higher than those on dielectric silica nanoparticle.

❖ To investigate the role of nanoparticle-electrolyte interface in the heat loss, proteins like bovine serum albumin were adsorbed onto silica nanoparticles' surface to modify the nanoparticle-electrolyte interface. Synergistic heat enhancement is observed in case of surface-modified particles. A 2.5 times and 8 times enhancement in SAR values is observed in case of particles modified with physiologically relevant proteins like BSA (Bovine Serum Albumin) and FBS (Fetal Bovine Serum) respectively. Use of such proteins not only proves the notion behind the interaction of fields with particle-electrolyte interface, but also gives us a prediction about the in vivo loss mechanism, as the microenvironment of the nanoparticle will change with the organs and tissues.

❖ To understand the electromagnetic behavior of the charged surface-electrolyte interface, the intrinsic non-linear impedance signatures of bio-electrolytes placed within planar gold electrodes were studied. An intrinsic non-linear effect due to the electrode-electrolyte interface interfered with the nonlinear signals coming from the biological samples. This contribution of the insulator-coated gold electrode-electrolyte interface to the observed nonlinearity from any aqueous electrolytic solution is calculated as a function of its ionic concentration using the electrical double-layer model approach. The third order coefficients of the power series of the nonlinear transfer function of a

bio-electrolytic system are derived and related to the capacitive and conductive components of impedance at electrode-electrolyte interface.

The future work includes the development of a model based on the physics of the nonlinear nanoparticle electrolyte interface to elucidate the mechanism of heating. The ohmic and/or dielectric loss of embedding polymer matrix (dextran, PEG, etc.) must be analyzed as a nanoparticle-polymer-solution interface, which could result in an additional source of E_{rf} induced loss. These hyperthermia studies on nanoparticles were performed at MHz regime of frequencies. Such studies should be repeated at kHz range of frequencies, where the effect from the nanoparticle-electrolyte interface will be more pronounced. Cell ablation using nanoparticles could be performed and the cell survival rate experiments could be studied to identify the effectiveness of the nanoparticle-assisted hyperthermia on different cell-lines, which would let us explore the cytotoxic heat response from different tumor types.

References

- [1] A. Han, L. Yang, and A. B. Frazier, "Quantification of the Heterogeneity in Breast Cancer Cell Lines Using Whole-Cell Impedance Spectroscopy," *Clinical Cancer Research*, vol. 13, pp. 139-143, January 1, 2007 2007.
- [2] M. Hywel, S. Tao, H. David, G. Shady, and G. G. Nicolas, "Single cell dielectric spectroscopy," *Journal of Physics D: Applied Physics*, vol. 40, p. 61, 2007.
- [3] H. P. Schwan, "Dielectric spectroscopy and electro-rotation of biological cells," *Ferroelectrics*, vol. 86, pp. 205-223, 1988/10/01 1988.
- [4] A. Koji, "Characterization of heterogeneous systems by dielectric spectroscopy," *Progress in Polymer Science*, vol. 27, pp. 1617-1659, 2002.
- [5] L. J. Challis, "Mechanisms for interaction between RF fields and biological tissue," *Bioelectromagnetics*, vol. 26, pp. S98-S106, 2005.
- [6] D. B. Kell, A. M. Woodward, E. A. Davies, R. W. Todd, M. F. Evans, and J. J. Rowland, "Nonlinear Dielectric Spectroscopy of Biological Systems: Principles and Applications," in *Nonlinear Dielectric Phenomena in Complex Liquids*. vol. 157, S. J. Rzoska and V. P. Zhelezny, Eds., ed: Springer Netherlands, 2005, pp. 335-344.
- [7] C. J. McLellan, A. D. C. Chan, and R. A. Goubran, "Aspects of Nonlinear Dielectric Spectroscopy of Biological Cell Suspensions," in *Engineering in Medicine and Biology Society, 2006. EMBS '06. 28th Annual International Conference of the IEEE*, 2006, pp. 455-458.
- [8] G. T. S. Mercier, A. Palanisami, and J. H. Miller Jr, "Nonlinear dielectric spectroscopy for label-free detection of respiratory activity in whole cells," *Biosensors and Bioelectronics*, vol. 25, pp. 2107-2114, 2010.
- [9] H. Yositate, M. Muraji, H. Tsujimoto, and W. Tatebe, "The estimation of the yeast growth phase by nonlinear dielectric properties of the measured electric current," *Journal of Electroanalytical Chemistry*, vol. 496, pp. 148 - 152, 2001.
- [10] S. N. Goldberg, M. Ahmed, G. S. Gazelle, J. B. Kruskal, J. C. Huertas, E. F. Halpern, B. S. Oliver, and R. E. Lenkinski, "Radio-Frequency Thermal Ablation with NaCl Solution Injection: Effect of Electrical Conductivity on Tissue Heating and Coagulation-Phantom and Porcine Liver Study," *Radiology*, vol. 219, pp. 157-165, April 1, 2001 2001.
- [11] J. Overgaard, "Effect of hyperthermia on malignant cells in vivo: A review and a hypothesis," *Cancer*, vol. 39, pp. 2637-2646, 1977.
- [12] P. Wust, B. Hildebrandt, G. Sreenivasa, B. Rau, J. Gellermann, H. Riess, R. Felix, and P. M. Schlag, "Hyperthermia in combined treatment of cancer," *The Lancet Oncology*, vol. 3, pp. 487-497, 2002.
- [13] B. Hildebrandt, P. Wust, O. Ahlers, A. Dieing, G. Sreenivasa, T. Kerner, R. Felix, and H. Riess, "The cellular and molecular basis of hyperthermia," *Critical Reviews in Oncology/Hematology*, vol. 43, pp. 33-56, 2002.
- [14] P. Carmeliet and R. K. Jain, "Angiogenesis in cancer and other diseases," *Nature*, vol. 407, pp. 249-257, 2000.

- [15] P. Vaupel, F. Kallinowski, and P. Okunieff, "Blood Flow, Oxygen and Nutrient Supply, and Metabolic Microenvironment of Human Tumors: A Review," *Cancer Research*, vol. 49, pp. 6449-6465, December 1, 1989 1989.
- [16] C. Jolly and R. I. Morimoto, "Role of the Heat Shock Response and Molecular Chaperones in Oncogenesis and Cell Death," *Journal of the National Cancer Institute*, vol. 92, pp. 1564-1572, October 4, 2000 2000.
- [17] D. M. Katschinski, "On Heat and Cells and Proteins," *Physiology*, vol. 19, pp. 11-15, February 1, 2004 2004.
- [18] R. A. McTaggart and D. E. Dupuy, "Thermal Ablation of Lung Tumors," *Techniques in Vascular and Interventional Radiology*, vol. 10, pp. 102-113, 2007.
- [19] A. Gevarghez and D. H. W. Groenemeyer, "Image-guided radiofrequency ablation (RFA) of spinal tumors," *European Journal of Radiology*, vol. 65, pp. 246-252, 2008.
- [20] J. van der Zee, "Heating the patient: a promising approach?," *Annals of Oncology*, vol. 13, pp. 1173-1184, August 1, 2002 2002.
- [21] C. J. Trujillo-Romero, S. Garcia-Jimeno, A. Vera, L. Leija, and J. Estelrich, ""Using nanoparticles for enhancing the focusing heating effect of an external waveguide applicator for oncology hyperthermia: evaluation in muscle and tumor phantoms,," *Progress In Electromagnetics Research*, vol. Vol. 121, pp. 343-363, 2011.
- [22] L. Brannon-Peppas and J. O. Blanchette, "Nanoparticle and targeted systems for cancer therapy," *Advanced Drug Delivery Reviews*, vol. 56, pp. 1649-1659, 2004.
- [23] A. Jordan, R. Scholz, P. Wust, H. Schirra, S. Thomas, H. Schmidt, and R. Felix, "Endocytosis of dextran and silan-coated magnetite nanoparticles and the effect of intracellular hyperthermia on human mammary carcinoma cells in vitro," *Journal of Magnetism and Magnetic Materials*, vol. 194, pp. 185-196, 1999.
- [24] B. Y. S. Kim, J. T. Rutka, and W. C. W. Chan, "Nanomedicine," *New England Journal of Medicine*, vol. 363, pp. 2434-2443, 2010.
- [25] A. Schroeder, D. A. Heller, M. M. Winslow, J. E. Dahlman, G. W. Pratt, R. Langer, T. Jacks, and D. G. Anderson, "Treating metastatic cancer with nanotechnology," *Nat Rev Cancer*, vol. 12, pp. 39-50, 2012.
- [26] B. Godin, W. H. Driessen, B. Proneth, S. Y. Lee, S. Srinivasan, R. Rumbaut, W. Arap, R. Pasqualini, M. Ferrari, and P. Decuzzi, "An integrated approach for the rational design of nanovectors for biomedical imaging and therapy," *Adv Genet*, vol. 69, pp. 31-64, 2010.
- [27] B. Godin, E. Tasciotti, X. Liu, R. E. Serda, and M. Ferrari, "Multistage Nanovectors: From Concept to Novel Imaging Contrast Agents and Therapeutics," *Acc Chem Res*, Sep 8 2011.
- [28] M. Johannsen, U. Gneveckow, B. Thiesen, K. Taymoorian, C. H. Cho, N. Waldöfner, R. Scholz, A. Jordan, S. A. Loening, and P. Wust, "Thermotherapy of Prostate Cancer Using Magnetic Nanoparticles: Feasibility, Imaging, and Three-Dimensional Temperature Distribution," *European Urology*, vol. 52, pp. 1653-1662, 2007.

- [29] S. Laurent, S. Dutz, U. O. Häfeli, and M. Mahmoudi, "Magnetic fluid hyperthermia: Focus on superparamagnetic iron oxide nanoparticles," *Advances in Colloid and Interface Science*, vol. 166, pp. 8-23, 2011.
- [30] W. Wu, Q. He, and C. Jiang, "Magnetic Iron Oxide Nanoparticles: Synthesis and Surface Functionalization Strategies," *Nanoscale Research Letters*, vol. 3, pp. 397 - 415, 2008.
- [31] R. Hergt and S. Dutz, "Magnetic particle hyperthermia--biophysical limitations of a visionary tumour therapy," *Journal of Magnetism and Magnetic Materials*, vol. 311, pp. 187-192, 2007.
- [32] S. D. Kong, W. Zhang, J. H. Lee, K. Brammer, R. Lal, M. Karin, and S. Jin, "Magnetically Vectored Nanocapsules for Tumor Penetration and Remotely Switchable On-Demand Drug Release," *Nano Letters*, vol. 10, pp. 5088-5092, 2010/12/08 2010.
- [33] S. Mornet, S. Vasseur, F. Grasset, and E. Duguet, "Magnetic nanoparticle design for medical diagnosis and therapy," *Journal of Materials Chemistry*, vol. 14, pp. 2161-2175, 2004.
- [34] A. Jordan, P. Wust, H. Föhlhling, W. John, A. Hinz, and R. Felix, "Inductive heating of ferrimagnetic particles and magnetic fluids: Physical evaluation of their potential for hyperthermia," *Int J Hypertherm*, vol. 25, pp. 499-511, 2009.
- [35] C. Gannon, C. Patra, R. Bhattacharya, P. Mukherjee, and S. Curley, "Intracellular gold nanoparticles enhance non-invasive radiofrequency thermal destruction of human gastrointestinal cancer cells," *Journal of Nanobiotechnology*, vol. 6, p. 2, 2008.
- [36] D. E. Kruse, D. N. Stephens, H. A. Lindfors, E. S. Ingham, E. E. Paoli, and K. W. Ferrara, "A Radio-Frequency Coupling Network for Heating of Citrate-Coated Gold Nanoparticles for Cancer Therapy: Design and Analysis," *Biomedical Engineering, IEEE Transactions on*, vol. 58, pp. 2002-2012, 2011.
- [37] C. Moran, S. Wainerdi, T. Cherukuri, C. Kittrell, B. Wiley, N. Nicholas, S. Curley, J. Kanzius, and P. Cherukuri, "Size-dependent joule heating of gold nanoparticles using capacitively coupled radiofrequency fields," *Nano Research*, vol. 2, pp. 400-405, 2009.
- [38] G. W. Hanson, R. C. Monreal, and S. P. Apell, "Electromagnetic absorption mechanisms in metal nanospheres: Bulk and surface effects in radiofrequency-terahertz heating of nanoparticles," *Journal of Applied Physics*, vol. 109, p. 124306, 2011.
- [39] D. Li, Y. S. Jung, S. Tan, H. K. Kim, E. Chory, and D. A. Geller, "Negligible absorption of radiofrequency radiation by colloidal gold nanoparticles," *Journal of Colloid and Interface Science*, vol. 358, pp. 47-53, 2011.
- [40] R. T. Hitchcock and R. M. Patterson, *Radio-Frequency and Elf Electromagnetic Energies: A Handbook for Health Professionals*: John Wiley & Sons, 1995.
- [41] B. J. Klauenberg and D. Miklavčič, *Radio Frequency Radiation Dosimetry and Its Relationship to the Biological Effects of Electromagnetic Fields*: Kluwer Academic Publishers, 2000.
- [42] R. W. Y. Habash, *Bioeffects and Therapeutic Applications of Electromagnetic Energy*: CRC Press, 2008.

- [43] K. R. Foster, F. A. Sauer, and H. P. Schwan, "Electrorotation and levitation of cells and colloidal particles," *Biophysical journal*, vol. 63, pp. 180-190, 1992.
- [44] E. Alphandéry, S. Faure, L. Raison, E. Duguet, P. A. Howse, and D. A. Bazylinski, "Heat Production by Bacterial Magnetosomes Exposed to an Oscillating Magnetic Field," *The Journal of Physical Chemistry C*, vol. 115, pp. 18-22, 2011/01/13 2010.
- [45] K. Ērglis, Q. Wen, V. Ose, A. Zeltins, A. Sharipo, P. A. Janmey, and A. C bers, "Dynamics of Magnetotactic Bacteria in a Rotating Magnetic Field," *Biophysical journal*, vol. 93, pp. 1402-1412, 2007.
- [46] Y. Kotsuka, E. Hankui, and Y. Shigematsu, "Development of ferrite core applicator system for deep-induction hyperthermia," *Microwave Theory and Techniques, IEEE Transactions on*, vol. 44, pp. 1803-1810, 1996.
- [47] D. Sullivan, "Three-dimensional computer simulation in deep regional hyperthermia using the finite-difference time-domain method," *Microwave Theory and Techniques, IEEE Transactions on*, vol. 38, pp. 204-211, 1990.
- [48] L. Dubois, J. P. Sozanski, V. Tessier, J. C. Camart, J. J. Fabre, J. Pribetich, and M. Chive, "Temperature control and thermal dosimetry by microwave radiometry in hyperthermia," *Microwave Theory and Techniques, IEEE Transactions on*, vol. 44, pp. 1755-1761, 1996.
- [49] S. Grimnes and Ø. G. Martinsen, *Bioimpedance and Bioelectricity Basics*: Academic, 2008.
- [50] K. Asami, "Characterization of heterogeneous systems by dielectric spectroscopy," *Progress in Polymer Science*, vol. 27, pp. 1617-1659, 2002.
- [51] K. Asami, "Characterization of biological cells by dielectric spectroscopy," *Journal of Non-Crystalline Solids*, vol. 305, pp. 268-277, 2002.
- [52] K. Asami, T. Hanai, and N. Koizumi, "Dielectric properties of yeast cells," *Journal of Membrane Biology*, vol. 28, pp. 169-180, 1976.
- [53] H. Morgan, T. Sun, D. Holmes, S. Gawad, and N. G. Green, "Single cell dielectric spectroscopy," *Journal of Physics D: Applied Physics*, vol. 40, p. 61, 2007.
- [54] P. Christophersen and P. Bennekou, "Evidence for a voltage-gated, non-selective cation channel in the human red cell membrane," *Biochimica et Biophysica Acta (BBA) - Biomembranes*, vol. 1065, pp. 103-106, 1991.
- [55] L. F. Cima and L. M. Mir, "Macroscopic characterization of cell electroporation in biological tissue based on electrical measurements," *Applied Physics Letters*, vol. 85, pp. 4520-4522, 2004.
- [56] S. De, R. Basu, and P. Nandy, "Confirmation of membrane electroporation from flicker noise," *Physical Review B*, vol. 61, p. 6689, 2000.
- [57] R. Astumian and B. Robertson, "Nonlinear effect of an oscillating electric field on membrane proteins," *The Journal of Chemical Physics*, vol. 91, pp. 4891 - 4901, 1989.
- [58] A. McShea, A. M. Woodward, and D. B. Kell, "Non-linear dielectric properties of *Rhodobacter capsulatus*," *Bioelectrochemistry and Bioenergetics*, vol. 29, pp. 205-214, 1992.

- [59] A. Woodward and D. Kell, "On the nonlinear dielectric properties of biological systems: *Saccharomyces cerevisiae*," *Bioelectrochemistry and Bioenergetics*, vol. 24, pp. 83 - 100, 1990.
- [60] V. I. Passechnik, "Estimates of the intramembrane field through the harmonics of capacitive current in inhomogeneous bilayer lipid membranes," *Bioelectrochemistry*, vol. 54, pp. 63-73, 2001.
- [61] M. Moussavi, H. Schwan, and H. Sun, "Harmonic distortion caused by electrode polarisation," *Medical and Biological Engineering and Computing*, vol. 32, pp. 121-125, 1994.
- [62] H. Schwan, "Linear and nonlinear electrode polarization and biological materials," *Annals of Biomedical Engineering*, vol. 20, pp. 269-288, 1992.
- [63] L. Geddes, "Historical evolution of circuit models for the electrode-electrolyte interface," *Annals of Biomedical Engineering*, vol. 25, pp. 1-14, 1997.
- [64] A. Richardot and E. T. McAdams, "Harmonic analysis of low-frequency bioelectrode behavior," *Medical Imaging, IEEE Transactions on*, vol. 21, pp. 604-612, 2002.
- [65] J. P. Diard, B. Le Gorrec, and C. Montella, "Deviation from the polarization resistance due to non-linearity I - theoretical formulation," *Journal of Electroanalytical Chemistry*, vol. 432, pp. 27-39, 1997.
- [66] L. Højgaard Olesen, M. Z. Bazant, and H. Bruus, "Strongly nonlinear dynamics of electrolytes in large ac voltages," *Physical Review E*, vol. 82, p. 011501, 2010.
- [67] G. F. Baronzio and E. D. Hager, *Hyperthermia in Cancer Treatment: A Primer*: Springer, 2006.
- [68] J. M. Brown and A. J. Giaccia, "The Unique Physiology of Solid Tumors: Opportunities (and Problems) for Cancer Therapy," *Cancer Research*, vol. 58, pp. 1408-1416, April 1, 1998 1998.
- [69] D. J. Chaplin, R. E. Durand, and P. L. Olive, "Acute hypoxia in tumors: Implications for modifiers of radiation effects," *International Journal of Radiation Oncology*Biology*Physics*, vol. 12, pp. 1279-1282, 1986.
- [70] S. B. Field and C. Franconi, *Physics and technology of hyperthermia*: M. Nijhoff, 1987.
- [71] A. Vander Vorst, A. Rosen, and Y. Kotsuka, *RF/Microwave Interaction With Biological Tissues*: John Wiley & Sons, 2006.
- [72] W. C. Dewey, L. E. Hopwood, S. A. Sapareto, and L. E. Gerweck, "Cellular responses to combinations of hyperthermia and radiation," *Radiology*, vol. 123, pp. 463-74, 1977.
- [73] C. D. Landon, M. W. Dewhirst, J. Y. Park, and D. Needham, "Nanoscale drug delivery and hyperthermia: The materials design and preclinical and clinical testing of low temperature-sensitive liposomes used in combination with mild hyperthermia in the treatment of local cancer," *Open Nanomed. J. Open Nanomedicine Journal*, vol. 3, pp. 38-64, 2011.
- [74] J. Kunisaki, T. Saito, T. Yamada, Y. Takemura, T. Niwa, and T. Inoue, "A Possibility of Hyperthermia Treatment using MRI Equipment," in *Engineering in Medicine and Biology Society, 2006. EMBS '06. 28th Annual International Conference of the IEEE*, 2006, pp. 6373-6375.

- [75] M. Morita, T. Inoue, T. Yamada, Y. Takemura, and T. Niwa, "Resonant circuits for hyperthermia excited by RF magnetic field of MRI," *Magnetics, IEEE Transactions on*, vol. 41, pp. 3673-3675, 2005.
- [76] W. J. Atkinson, I. A. Brezovich, and D. P. Chakraborty, "Usable Frequencies in Hyperthermia with Thermal Seeds," *Biomedical Engineering, IEEE Transactions on*, vol. BME-31, pp. 70-75, 1984.
- [77] J. R. Kanwar, X. Sun, V. Punj, B. Sriramoju, R. R. Mohan, S.-F. Zhou, A. Chauhan, and R. K. Kanwar, "Nanoparticles in the treatment and diagnosis of neurological disorders: untamed dragon with fire power to heal," *Nanomedicine: Nanotechnology, Biology and Medicine*, vol. 8, pp. 399-414, 2012.
- [78] S. Azarmi, W. H. Roa, and R. Löbenberg, "Targeted delivery of nanoparticles for the treatment of lung diseases," *Advanced Drug Delivery Reviews*, vol. 60, pp. 863-875, 2008.
- [79] P. Cherukuri, E. S. Glazer, and S. A. Curley, "Targeted hyperthermia using metal nanoparticles," *Advanced Drug Delivery Reviews*, vol. 62, pp. 339-345, 2010.
- [80] M. Liong, J. Lu, M. Kovichich, T. Xia, S. G. Ruehm, A. E. Nel, F. Tamanoi, and J. I. Zink, "Multifunctional Inorganic Nanoparticles for Imaging, Targeting, and Drug Delivery," *ACS Nano*, vol. 2, pp. 889-896, 2008/05/01 2008.
- [81] B. Thiesen and A. Jordan, "Clinical applications of magnetic nanoparticles for hyperthermia," *Int J Hypertherm*, vol. 24, pp. 467-474, 2008.
- [82] P. Wust, U. Gneveckow, M. Johannsen, D. Böhmer, T. Henkel, F. Kahmann, J. Sehouli, R. Felix, J. Rieke, and A. Jordan, "Magnetic nanoparticles for interstitial thermotherapy - feasibility, tolerance and achieved temperatures," *Int J Hypertherm*, vol. 22, pp. 673-685, 2006.
- [83] R. K. Gilchrist, R. Medal, W. D. Shorey, R. C. Hanselman, J. C. Parrott, and C. B. Taylor, "Selective inductive heating of lymph nodes," *Annals of surgery*, vol. 146, pp. 596-606, 1957.
- [84] R. E. Rosensweig, "Heating magnetic fluid with alternating magnetic field," *Journal of Magnetism and Magnetic Materials*, vol. 252, pp. 370-374, 2002.
- [85] X. Wang, H. Gu, and Z. Yang, "The heating effect of magnetic fluids in an alternating magnetic field," *Journal of Magnetism and Magnetic Materials*, vol. 293, pp. 334-340, 2005.
- [86] S. Purushotham and R. V. Ramanujan, "Modeling the performance of magnetic nanoparticles in multimodal cancer therapy," *Journal of Applied Physics*, vol. 107, pp. 114701-114701-9, 2010.
- [87] D. Pissuwan, S. M. Valenzuela, and M. B. Cortie, "Therapeutic possibilities of plasmonically heated gold nanoparticles," *Trends in Biotechnology*, vol. 24, pp. 62-67, 2006.
- [88] D. K. Roper, W. Ahn, and M. Hoepfner, "Microscale Heat Transfer Transduced by Surface Plasmon Resonant Gold Nanoparticles," *The Journal of Physical Chemistry C*, vol. 111, pp. 3636-3641, 2007/03/01 2007.
- [89] E. S. Glazer, C. Zhu, K. L. Massey, C. S. Thompson, W. D. Kaluarachchi, A. N. Hamir, and S. A. Curley, "Noninvasive Radiofrequency Field Destruction of Pancreatic Adenocarcinoma Xenografts Treated with Targeted Gold

- Nanoparticles," *Clinical Cancer Research*, vol. 16, pp. 5712-5721, December 1, 2010.
- [90] J. R. Klune, G. Jeyabalan, E. S. Chory, J. Kanzius, and D. A. Geller, "P64: Pilot investigation of a new instrument for non-invasive radiofrequency ablation of cancer," *The Journal of surgical research*, vol. 137, p. 263, 2007.
 - [91] J. A. Pearce and J. R. Cook, "Heating mechanisms in gold nanoparticles at radio frequencies," in *Engineering in Medicine and Biology Society, EMBC, 2011 Annual International Conference of the IEEE*, 2011, pp. 5577-5580.
 - [92] X. Liu, H.-j. Chen, X. Chen, C. Parini, and D. Wen, "Low frequency heating of gold nanoparticle dispersions for non-invasive thermal therapies," *Nanoscale*, vol. 4, pp. 3945-3953, 2012.
 - [93] Z. M. Markovic, L. M. Harhaji-Trajkovic, B. M. Todorovic-Markovic, D. P. Kepić, K. M. Arsikin, S. P. Jovanović, A. C. Pantovic, M. D. Dramićanin, and V. S. Trajkovic, "In vitro comparison of the photothermal anticancer activity of graphene nanoparticles and carbon nanotubes," *Biomaterials*, vol. 32, pp. 1121-1129, 2011.
 - [94] N. Huang, H. Wang, J. Zhao, H. Lui, M. Korbelik, and H. Zeng, "Single-wall carbon nanotubes assisted photothermal cancer therapy: Animal study with a murine model of squamous cell carcinoma," *Lasers in Surgery and Medicine*, vol. 42, pp. 638-648, 2010.
 - [95] S. Ghosh, S. Dutta, E. Gomes, D. Carroll, R. D'Agostino, J. Olson, M. Guthold, and W. H. Gmeiner, "Increased Heating Efficiency and Selective Thermal Ablation of Malignant Tissue with DNA-Encased Multiwalled Carbon Nanotubes," *ACS Nano*, vol. 3, pp. 2667-2673, 2009/09/22 2009.
 - [96] C. J. Gannon, P. Cherukuri, B. I. Yakobson, L. Cognet, J. S. Kanzius, C. Kittrell, R. B. Weisman, M. Pasquali, H. K. Schmidt, R. E. Smalley, and S. A. Curley, "Carbon nanotube-enhanced thermal destruction of cancer cells in a noninvasive radiofrequency field," *Cancer*, vol. 110, pp. 2654-2665, 2007.
 - [97] H. Xia, K. Karasawa, N. Hanyu, T.-C. Chang, M. Okamoto, Y. Kiguchi, M. Kawakami, and T. Itazawa, "Hyperthermia combined with intra-thoracic chemotherapy and radiotherapy for malignant pleural mesothelioma," *International Journal of Hyperthermia*, vol. 22, pp. 613-621, 2006.
 - [98] J. Overgaard, "The current and potential role of hyperthermia in radiotherapy," *International Journal of Radiation Oncology*Biology*Physics*, vol. 16, pp. 535-549, 1989.
 - [99] J. S. Ananta, B. Godin, R. Sethi, L. Moriggi, X. Liu, R. E. Serda, R. Krishnamurthy, R. Muthupillai, R. D. Bolskar, L. Helm, M. Ferrari, L. J. Wilson, and P. Decuzzi, "Geometrical confinement of gadolinium-based contrast agents in nanoporous particles enhances T1 contrast," *Nat Nano*, vol. 5, pp. 815-821, 2010.
 - [100] H. Gröll and S. Langereis, "Hyperthermia-triggered drug delivery from temperature-sensitive liposomes using MRI-guided high intensity focused ultrasound," *Journal of Controlled Release*.
 - [101] J. C. Pedro and N. B. Carvalho, *Intermodulation Distortion in Microwave and Wireless Circuits*: Artech House, 2003.

- [102] B. H. Moeckly, K. E. Kihlstrom, A. T. Findikoglu, and D. E. Oates, "Microwave properties of MgB₂ thin films grown by reactive evaporation," *Applied Superconductivity, IEEE Transactions on*, vol. 15, pp. 3308-3312, 2005.
- [103] R. Pande, L. Xie, W. Zagozdzon-Wosik, K. Nesteruk, and J. Wosik, "Use of the radiofrequency-intermodulation distortion technique to investigate intrinsic nonlinearity at the electrode-electrolyte interface," *Applied Physics Letters*, vol. 100, pp. 063701-4, 2012.
- [104] G. Ruiz and C. J. Felice, "Non-linear response of an electrode-electrolyte interface impedance with the frequency," *Chaos, Solitons & Fractals*, vol. 31, pp. 327-335, 2007.
- [105] J. H. Masliyah and S. Bhattacharjee, "Electric Double Layer," in *Electrokinetic and Colloid Transport Phenomena*, ed: John Wiley & Sons, Inc., 2005, pp. 105-178.
- [106] P. Somasundaran, *Encyclopedia of Surface and Colloid Science*: Taylor & Francis, 2006.
- [107] J. H. Masliyah and S. Bhattacharjee, "Fundamental Transport Equations," in *Electrokinetic and Colloid Transport Phenomena*, ed: John Wiley & Sons, Inc., 2005, pp. 179-220.
- [108] B. Park, A. G. Webb, and C. M. Collins, "A method to separate conservative and magnetically-induced electric fields in calculations for MRI and MRS in electrically-small samples," *Journal of Magnetic Resonance*, vol. 199, pp. 233-237, 2009.
- [109] F. S. Chute and F. E. Vermeulen, "A Visual Demonstration of the Electric Field of a Coil Carrying a Time-Varying Current," *Education, IEEE Transactions on*, vol. 24, pp. 278-283, 1981.
- [110] K. C. Grabar, R. G. Freeman, M. B. Hommer, and M. J. Natan, "Preparation and Characterization of Au Colloid Monolayers," *Analytical Chemistry*, vol. 67, pp. 735-743, 1995/02/01 1995.
- [111] D. Ketharnath, R. Pande, L. Xie, S. Srinivasan, B. Godin, and J. Wosik, "A method to measure magnetic specific absorption rate of nanoparticles in colloidal suspension by using different configurations of conservative and magnetically-induced electric fields," *Applied Physics Letters*, vol. Submitted, 2012.